Laser Spectroscopy of the Fourth Positive System of Carbon Monoxide Isotopomers

Anton du Plessis

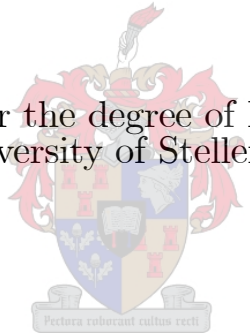

Dissertation presented for the degree of Doctor of Philosophy at the University of Stellenbosch

Promoter: Dr. E.G. Rohwer, University of Stellenbosch

Co-promoter: Dr. C.M. Steenkamp, University of Stellenbosch

April 2006

Declaration

I, the undersigned, hereby declare that the work contained in this dissertation is my own original work and that I have not previously in its entirety or in part submitted it at any university for a degree.

....

Signature Date

Abstract

Carbon monoxide (CO) is a diatomic molecule of particular interest in astrophysics, due to its high abundance in interstellar space. The Fourth Positive System $A^1\Pi - X^1\Sigma^+$ of CO is an important feature in the vacuum ultraviolet (VUV) region of the electromagnetic spectrum in astronomical observations, especially in high-resolution spectra recorded by satellite-based spectrographs. The interpretation of these astronomically detected spectra requires accurate laboratory wavelengths to serve as rest wavelengths and to resolve possible Doppler-shifts. Such rest wavelengths are known for the $^{12}C^{16}O$, $^{13}C^{16}O$ and $^{12}C^{18}O$ isotopomers for all astronomically observed spectral lines of the Fourth Positive System. The only laboratory wavelengths currently available for the Fourth Positive System of the $^{12}C^{17}O$ isotopomer have been determined in a previous work carried out in our laboratory for the vibronic band $A^1\Pi(v' = 3) - X^1\Sigma^+(v'' = 0)$. The present study continues this work for the other vibronic bands which have been detected astronomically, namely $A^1\Pi(v' = 2 - 5) - X^1\Sigma^+(v'' = 0)$. The $A^1\Pi(v' = 0 - 1) - X^1\Sigma^+(v'' = 0)$ vibronic bands have also been investigated due to their probability for future astronomical detection. Rotationally-resolved spectra of these six vibronic bands were obtained by selective rovibronic laser excitation, and subsequent detection of the undispersed fluorescence, observed as a function of the excitation wavelength in the VUV. A tunable narrow-bandwidth VUV laser source is used for excitation, and the CO gas sample is introduced by supersonic expansion. Flow-cooling in the supersonic expansion to rotational temperatures roughly corresponding to temperatures in the interstellar medium simplifies and aids the spectral analysis of the spectral lines of interest. The cold conditions in the supersonic expansion facilitates a high sensitivity for detection of the low-J lines, and allows the detection of rare isotopomers of CO in natural abundance. The experimental setup has been improved in the present study by the addition of a vacuum monochromator, facilitating an improved characterisation of the VUV source. Furthermore, a number of experimental conditions have been optimised for the detection of rare CO isotopomers, significantly increasing the signals of these lines in the spectra. The combination of this increase in sensitivity and the addition of the vacuum monochromator to the experimental setup, allowed the simultaneous detection of absorption spectra with the fluorescence spectra as an additional source of information in spectral analysis. The increased sensitivity also contributed to the detection of a large number of spectral lines of interest, with some additional lines identified in the previously studied vibronic band. Spectral lines of $^{12}C^{16}O$, $^{13}C^{16}O$, $^{12}C^{18}O$ and $^{12}C^{17}O$ were detected in each vibronic band, allowing accurate calibration of the spectra. A total of 29 new lines of $^{12}C^{17}O$ were recorded in the six vibronic bands investigated. Additionally, 10 new singlet-triplet lines of $^{12}C^{16}O$ were recorded in the wavelength regions investigated. The new wavelengths of $^{12}C^{17}O$ have been applied to calculate consistent heliocentric velocities of a gas cloud toward the star X Persei, obtained from spectra of the different CO isotopomers taken by the Hubble space telescope.

Opsomming

Koolstofmonoksied (CO) is 'n diatomiese molekuul wat veral van belang is in die ruimtefisika vanweë sy volopheid in die heelal. Die Vierde Positiewe Stelsel $A^1\Pi - X^1\Sigma^+$ van CO is 'n belangrike kenmerk in die vakuum ultraviolet (VUV) gedeelte van die elektromagnetiese spektrum in astronomiese waarnemings, veral in hoë resolusie spektra wat opgeneem word deur satelliet-gebaseerde spektrograwe. Daar word vir die interpretasie van bogenoemde spektra akkurate laboratorium golflengtes benodig, om as rus-golflengtes te dien en om moontlike Doppler-verskuiwings op te los. Sulke rus-golflengtes is bekend vir die $^{12}C^{16}O$, $^{13}C^{16}O$ and $^{12}C^{18}O$ isotopomere vir alle astronomies-waargenome spektraal-lyne van die Vierde Positiewe Stelsel. Die enigste laboratorium golflengtes tans beskikbaar vir die Vierde Positiewe Stelsel van die $^{12}C^{17}O$ isotopomeer is in die vorige werk in ons laboratorium bepaal vir die vibroniese band $A^1\Pi(v' = 3) - X^1\Sigma^+(v'' = 0)$. Die huidige studie brei hierop uit vir die ander vibroniese bande wat al astronomies waargeneem is, naamlik $A^1\Pi(v' = 2 - 5) - X^1\Sigma^+(v'' = 0)$. Die $A^1\Pi(v' = 0 - 1) - X^1\Sigma^+(v'' = 0)$ vibroniese bande is addisioneel ondersoek weens hul hoë waarskynlikheid vir toekomstige astronomiese waarnemings. Rotasioneel-opgeloste spektra van hierdie ses vibroniese bande is verkry deur selektiewe rovibroniese laser opwekking en waarneming van die totale resulterende fluoressensie as 'n funksie van opwekkings-golflengte in die VUV. 'n Verstelbare nou-bandwydte VUV laserbron word gebruik vir die opwekking, en die CO gas word ingevoer deur middel van supersoniese uitsetting. Vloei-verkoeling in die supersoniese uitsetting veroorsaak rotasionele temperature wat rofweg ooreenstem met dié in die buitenste ruimte en vereenvoudig die spektrale analise. Die koue toestande in die supersoniese uitsetting fasiliteer 'n hoë sensitiwiteit vir waarneming van die lae-J lyne, wat die waarneming van skaars isotopomere van CO in hul natuurlike volophede bewerkstellig. Die eksperimentele metode is in die huidige studie verbeter deur die toevoeging van 'n vakuum monokromator, wat 'n verbeterde karakterisering van die VUV bron bewerkstellig. Verder is 'n aantal eksperimentele kondisies geoptimeer vir die deteksie van skaars CO isotopomere, wat die seine van hierdie spektraal-lyne heelwat verhoog. Die kombinasie van die toename in sensitiwiteit en die toevoeging van die vakuum monokromator tot die eksperimentele opstelling het die meet van absorpsie spektra gelyktydig met die fluoresensie spektra moontlik gemaak. Hierdie word gebruik as 'n addisionele bron van inligting in spektrale analise. Die verhoogde sensitiwiteit het ook die meet van baie meer lyne as voorheen moontlik gemaak, met addisionele lyne ook in die voorheen gemete band. Spektraal-lyne van $^{12}C^{16}O$, $^{13}C^{16}O$, $^{12}C^{18}O$ en $^{12}C^{17}O$ is in elke vibroniese band gemeet, wat kalibrasie vereenvoudig. In totaal is 29 nuwe lyne van $^{12}C^{17}O$ gemeet in die ses vibroniese bande. Addisioneel is 10 nuwe singlet-triplet lyne van $^{12}C^{16}O$ gemeet in die golflengte gebiede wat ondersoek is. Die nuwe golflengtes van $^{12}C^{17}O$ is toegepas om akkurate snelhede van 'n gaswolk in die rigting van die ster X Persei te bereken, vanaf spektra van die CO isotopomere wat deur die Hubble ruimte-teleskoop gemeet is.

Acknowledgements

The financial assistance of the National Research Foundation (NRF) towards this research is hereby acknowledged. Opinions expressed and conclusions arrived at, are those of the author and are not necessarily attributed to the NRF.

There are three persons who deserve special acknowledgement for their contributions to my development as an experimental physicist. They are Dr Erich Rohwer, Dr Christine Steenkamp and Ulli Deutschländer. Without these three persons I would never have completed this work and would have been a much poorer person. Dr Rohwer has been the best supervisor and mentor any student can ask for and has succeeded in fostering scientific thinking skills in me, which is the most valuable lesson that I have learned during the ten years of my tertiary education. I thank him for his belief in me and his non-judgemental character, and for giving me so many opportunities which few students ever receive. Dr Christine Steenkamp has been involved in many discussions and decisions regarding this work and always has been more than willing to help in any way. Her precision and scientific skills have been something from which I could learn and gave me the highest goal to strive towards. Ulli Deutschländer has been responsible for my development as a practical experimentalist and his work methodology has been something from which I have learned a great deal and will continue to use in many different situations.

I would also like to acknowledge Prof Piet Walters, Henk van Wyk and Ping Huang. I have learned a great deal of spectroscopy and experimental techniques from Prof Walters, I learned to become an all-round laser mechanic from Henk and I learned some communication and scientific management skills from working with Ping.

I thank the Laser Research Institute for the support structures and my colleagues for their continued interest and co-operation. Thanks also go to the Department of Physics and all its staff for the comfortable working environment.

I thank my parents for their love and for the financial support over the years and for always supporting their crazy scientist son.

Finally I would like to thank Elize for her understanding during the hard times and for continued motivation and love. Behind every scientist.....

I thank God for guiding me in this work and for forming me in the way that he has in the last few years, even though I was at many stages not particularly malleable.

FÜR ELIZE

Contents

Chapter 1

Introduction

1.1 Relevance of carbon monoxide

Carbon monoxide, chemical formula CO, is a small heteronuclear diatomic molecule, consisting of a carbon atom and an oxygen atom. CO occurs naturally in the earth's atmosphere as a colourless, odourless, highly toxic gas. There are six stable isotopomers of CO. These are listed in Table 1.1 in the order of relative natural abundances. Unstable isotopomers, such as those containing the ^{14}C isotope, are not considered in this study [1] due to their low natural abundances.

Besides occuring naturally in the earth's atmosphere, CO is also formed artificially as a major product of the incomplete combustion of carbon and carbon-containing compounds. It is of great importance in environmental monitoring and atmospheric research.

In molecular physics, CO is widely considered a prototype molecule for basic research. It

Table 1.1: Natural abundances of the different stable CO isotopomers

Stable isotopomer	**Natural abundance (%)**
$^{12}C^{16}O$	98.668
$^{13}C^{16}O$	1.100
$^{12}C^{18}O$	1.979×10^{-1}
$^{12}C^{17}O$	3.790×10^{-2}
$^{13}C^{18}O$	2.207×10^{-3}
$^{13}C^{17}O$	4.224×10^{-4}

has a simple electronic structure and can therefore be modelled theoretically.

CO is of particular interest in astrophysics, since it is the second-most abundant molecule in interstellar space, after hydrogen [2]. Since its first astronomical detection in 1972 [3], interstellar CO has been widely detected in the radiofrequency, infrared, and vacuum ultraviolet (VUV) regions of the spectrum. Radiofrequency observations originate from rotational transitions within the lowest vibrational level of the electronic ground state. Infrared observations originate from transitions between rotational levels of different vibrational levels in the electronic ground state. The VUV observations of interest in this work originate from rotational-vibrational-electronic transitions between the singlet electronic ground state and the first singlet electronically excited state. This is termed the Fourth Positive System of CO and is designated $A^1\Pi(v')-X^1\Sigma^+(v'')$ or $A^1\Pi-X^1\Sigma^+(v',v'')$ [1]. In this dissertation, only the $v''=0$ band progression (the collection of bands involving the $v''=0$ level) is of interest and the term Fourth Positive System includes this restriction throughout this dissertation unless otherwise stated, in order to simplify explanations. Such transitions between specific rotational levels in different vibrational levels of different electronic states are termed rovibronic transitions. Rovibronic lines originating from transitions between two specific vibrational states are termed a vibronic band.

VUV observatories are all satellite-based due to atmospheric absorption of VUV light. A list of past, present and future satellite-based observatories can be found online [4]. Interstellar CO spectra in the VUV are obtained in absorption and detected using spectrographs aboard these satellites. The Fourth Positive System in the VUV provides important information useful in determining the distribution of matter in planetary atmospheres, interstellar gas clouds and comet tails. The detection of different isotopomers of CO, other than $^{12}C^{16}O$, is of particular importance for two reasons. Firstly, the relative abundance of the different isotopomers in the region of observation, which is different from that on earth, may be used to develop improved models of interstellar clouds and theories of stellar evolution [5]. Secondly, since the observed $^{12}C^{16}O$ transitions saturate in absorption spectra, spectra of other isotopomers provide more accurate column densities, which can be related to the CO density in the observed region.

[1] The short form (v',v'') is sometimes used to describe the vibronic band when reference to the Fourth Positive System is implied.

Since CO is of such great importance in astrophysics, and also in environmental and basic research, it is one of the most extensively studied molecules in the laboratory. All current astrophysically-relevant spectral data of the Fourth Positive System of the $^{12}C^{16}O$, $^{13}C^{16}O$ and $^{12}C^{18}O$ isotopomers are known. However, for $^{12}C^{17}O$, experimentally measured spectral data of the Fourth Positive System that are required for astrophysical calculations have largely been lacking.

1.2 Experimental method

Laser spectroscopy is a well known method of probing the structure of atoms and molecules, and has many advantages over conventional absorption or emission spectroscopy [6]. Wavelength-tunable, narrow-bandwidth lasers are used to selectively populate energy levels of atoms or molecules without excitation of other levels or other species. Other excitation mechanisms lack this narrow bandwidth and therefore do not have such a high degree of selectivity in excitation. By tuning the laser wavelength in small steps and indirectly observing the excitation by observing fluorescence or absorption (or lack thereof), the atomic or molecular spectrum can be measured. This selectivity is especially useful in molecular spectroscopy, because of the large number of levels and the close spacing of the rotational levels.

The VUV region of the spectrum ($105 - 200$ nm) is still largely unexplored by laser spectroscopy due to the lack of commercial tunable narrow-bandwidth laser sources in this wavelength range. The VUV is a scientifically interesting region since VUV photon energies correspond to the electronic excitation energies of many small molecules of scientific interest (such as CO), and these energies also correspond to the ionisation energies of larger molecules of scientific interest, such as aromatic compounds. In our laboratory, we have in the last few years developed and optimised an experimental setup for generating tunable narrow-bandwidth VUV light and for applying it to spectroscopy of gaseous samples [1,7].

The CO molecules are introduced by supersonic expansion into the vacuum chamber where the intersection with the laser beam takes place. A supersonic expansion has many advantages over the traditional low-pressure stagnant gas volume [6]. The supersonic expansion is generated by the flow of molecules from a high-pressure volume, through a small orifice, into a vacuum

chamber. This flow becomes supersonic when the velocity of the molecules becomes larger than the velocity of sound in the medium [8]. The flow-cooling of the sample gas facilitates effective rotational temperatures as low as 2 K in our experimental setup [1]. The rotational temperatures reached in the supersonic expansion are therefore similar to the temperature in the interstellar medium, approximately 4 K [9].

The low temperatures in the supersonic expansion and in the interstellar medium result in a large total thermal population of the $v'' = 0$ vibrational level and vanishingly small thermal populations of the $v'' = 1, 2, 3, ...$ levels. Since astronomical detection is in the form of absorption lines, the population of the lower level of a given transition directly affects its detection probability. Similarly the signal strength of a spectral line in a laser induced fluorescence (LIF) excitation spectrum is dependant on the population in the lower state, from which laser excitation occurs.

In both interstellar and laboratory spectra, the rotational levels within the $v'' = 0$ vibrational level of a CO molecule are thermally populated according to the Boltzmann distribution. The low temperature and resulting population distribution limits the rotational lines which may be detected to those having low rotational quantum numbers J. This has the additional advantage of simplifying the spectra. The lowest v' levels in the upper electronic state are generally of interest due to their relatively large transition probabilities with the $v'' = 0$ level, which are called Franck-Condon factors.

In the present study CO molecules are selectively excited by tunable narrow-bandwidth VUV light and the total subsequent fluorescence is detected. This fluorescence signal is monitored as a function of wavelength, resulting in a LIF excitation spectrum. The transmitted laser energy is simultaneously monitored, resulting in an absorption spectrum. Spectra are calibrated using the rovibronic lines of $^{12}C^{16}O$ and $^{13}C^{16}O$ having $J \leq 6$ and using their known wavelengths from literature [9]. In the calibrated spectra, spectral lines of $^{12}C^{17}O$ and $^{12}C^{18}O$ can be assigned and their wavelengths determined.

1.3 Scope of this study

The lack of accurate laboratory wavelengths for the rovibronic lines of the Fourth Positive System of $^{12}C^{17}O$ has only recently been partially overcome by the $A^1\Pi(v' = 3)-X^1\Sigma^+(v'' = 0)$ spectral data recorded in our laboratory in the pioneering work of C.M. Steinmann [1,10].

The work presented in this dissertation comprises a continuation of the spectroscopy on rare CO isotopomers in our laboratory, providing a substantial amount of new and scientifically relevant spectroscopic data. Preliminary experimental spectra have been published [11] and the complete results and analysis of all six vibronic bands investigated will be submitted for publication shortly. This study focuses on the lowest vibronic bands of the Fourth Positive System $A^1\Pi(v' = 0 - 5)-X^1\Sigma^+(v'' = 0)$ of $^{12}C^{17}O$ and the lower rotational levels in these bands, as these are observed astronomically and are therefore of astrophysical relevance.

In the process of recording the high-resolution spectra of various isotopomers of CO, a number of so-called singlet-triplet lines were detected in the wavelength ranges of the Fourth Positive System vibronic bands investigated. These singlet-triplet lines refer to rovibronic transitions between the electronic singlet ground state and electronically excited triplet states. Pure singlet-triplet transitions are quantum-mechanically forbidden and therefore have low transition probabilities. These singlet-triplet lines are observed astronomically and have relevance in astrophysics.

In this study, the selectivity and sensitivity of the technique has been improved by experimental characterisation and optimisation of the experimental conditions. These experimental conditions can be applied in future investigations in our laboratory. They can also be applied to similar spectroscopic investigations and other molecular species, in our laboratory or elsewhere.

1.4 Outline of the dissertation

Chapter 2 gives an overview of the state of the research of CO and its isotopomers, and the experimental methods employed to probe such small molecules. Chapter 3 is a theoretical description of a number of physical principles and methods employed in this work. This is followed in Chapter 4 by a description of the experimental setup, focusing on experimental improvements implemented in this study. Chapter 5 contains the collection of experimental

results, subdivided into the following: (i) the characterisation of the VUV laser source, (ii) an introduction to the spectra, (iii) the optimisation of experimental conditions, (iv) the CO Fourth Positive System isotopomer spectral results, and (v) the CO singlet-triplet spectral results. Chapter 6 includes the analysis and discussion of these experimental results, subdivided into the same sections as above. Chapter 7 contains conclusions and an outlook for future work in this project. Chapter 8 contains appendices referenced within the dissertation.

Chapter 2

State of the research

2.1 Carbon monoxide

2.1.1 Literature background of the Fourth Positive System

The Fourth Positive System $A^1\Pi(v')-X^1\Sigma^+(v'')$ of CO has been studied in great detail in the past, using mostly absorption and emission spectroscopy. There are a number of reliable literature reviews of the experimental investigation of the CO molecular spectrum [9,12 – 16]. Transition energies for the CO molecule are summarised in Morton and Noreau (1994) [9], which is currently widely considered a standard reference for such data. Franck-Condon factors for the $^{12}C^{16}O$ transitions of the Fourth Positive System can be found in Borges, Caridade and Varandas (2001) [17]. Because of the differences in molecular masses, the isotopomers other than $^{12}C^{16}O$ have different molecular spectra, but have not been as widely studied due to their lower natural abundances.

Rotationally-resolved spectra of the Fourth Positive System of $^{12}C^{17}O$ and $^{12}C^{18}O$ have recently been detected in interstellar clouds [18]. These spectra are Doppler-shifted due to the velocity of the observed CO cloud relative to the observer, which is the Hubble space telescope in this case. Accurate rest wavelengths are therefore required to accurately determine this velocity, termed the heliocentric velocity. Since accurate laboratory wavelengths were not available for the $^{12}C^{17}O$ molecule, calculated rest wavelengths for $^{12}C^{17}O$ were used in calculations by Sheffer, Lambert and Federman (2002) [18]. This resulted in different calculated

heliocentric velocities for the $^{12}C^{17}O$ and $^{12}C^{18}O$ isotopomers in the same cloud, which is physically improbable.

2.1.2 Electronic ground state $X^1\Sigma^+$

The electronic ground state of CO is labelled $X^1\Sigma^+$ and is a singlet state. The ground state of CO, and specifically its lowest vibrational level $v'' = 0$, has been studied in detail by high-resolution microwave and infrared measurements for all stable isotopomers [15,19,20]. The resulting mass-independent Dunham coefficients, using the latest values in George, Urban and Le Floch (1994) [20], predict the observed frequencies of all stable CO isotopomers to extremely high accuracy (10 kHz). The calculated term values for the lowest rotational levels are tabulated in Morton and Noreau (1994) [9]. The accuracies of the term values of the ground state are estimated to be of the order 10^{-7} cm^{-1}, while those of the transitions involving the $A^1\Pi$ excited state are about 10^{-1} cm^{-1}(experimental accuracy of present results). The uncertainties of the ground-state term values are therefore ignored in this study.

2.1.3 Electronic excited state $A^1\Pi$ of $^{12}C^{16}O$

The lowest singlet electronic excited state of CO is labelled $A^1\Pi$. Transitions between the ground state $X^1\Sigma^+$ and the $A^1\Pi$ state, the Fourth Positive System, constitutes the lowest frequency dipole-allowed rovibronic band of CO. The Fourth Positive System of $^{12}C^{16}O$ has been the focus of many studies in the past. Initial measurements were done in emission, as summarised in Krupenie (1966) [12]. This was followed by high-resolution absorption measurements using large spectrographs, and the resulting term values are tabulated in Simmons, Bass and Tilford (1969) [13] and Tilford and Simmons (1972) [14]. These term values were reinvestigated later and improved term values for the vibrational bands with $v' = 0 - 8$ and rotational levels up to $J = 33$ are tabulated in Le Floch (1992) [21]. Calculations of transition energies for the Fourth Positive System were done using these term values for the $A^1\Pi$ state and the term values of George *et al.* (1994) [20] for the $X^1\Sigma^+$ state, and are summarised for rotational levels $J \leq 6$ in Morton and Noreau (1994) [9]. This reference is widely used as the wavelength standard for CO in astrophysical calculations, molecular physics calculations as well as calibration of synchrotron experiments. All Fourth Positive System rovibronic transition energies have been

recalculated in this work from the term values of Le Floch (1992) [21] and George *et al.* (1994) [20], rather than using the values calculated by Morton and Noreau (1994) [9].

2.1.4 Electronic excited state $A^1\Pi$ of other isotopomers

The first observation of the Fourth Positive System of $^{13}C^{16}O$, and specifically the transitions with lower vibrational level $v'' = 0$, are reported in the form of band heads in Tilford and Simmons (1972) [14]. Rotationally-resolved spectral lines of the Fourth Positive System of $^{13}C^{16}O$ were observed in early laser excitation experiments [22], although investigation into the detection of rarer isotopomers was not attempted at this stage. A complete study of the $^{13}C^{16}O$ Fourth Positive System was done later in the form of high-resolution measurements in an emission experiment, reported in Haridass and Huber (1994) [23]. This reference includes term values for the vibrational bands $v' = 0 - 9$ and rotational levels up to $J'' = 29$. Transition energies were calculated and are summarised in the review paper by Morton and Noreau (1994) [9] for rotational levels $J \leq 6$.

The Fourth Positive System of the $^{12}C^{18}O$ molecule has been studied in a specialised emission experiment, using a chemical reaction to produce a high density of $^{12}C^{18}O$. The corresponding term values are given in Beaty, Braun, Huber and Le Floch (1997) [24]. For the $^{12}C^{17}O$ molecule, Morton and Noreau (1994) [9] reported a lack of experimentally measured spectroscopic data. This gap in the literature has only recently been partially filled by the $A^1\Pi(v' = 3)-X^1\Sigma^+(v'' = 0)$ spectral data recorded in our laboratory in the pioneering work of C.M. Steinmann [1,10,25]. This work has been continued in the present study for the $A^1\Pi(v' = 0 - 5)-X^1\Sigma^+(v'' = 0)$ bands.

2.1.5 Triplet states

There are a number of triplet states in the region of the $A^1\Pi$ state, causing spin-orbit perturbations to this state. These perturbations make the modelling of the CO spectrum extremely difficult, and justify the rigorous experimental investigations of the $A^1\Pi$ and the perturbing states. Specifically the $e^3\Sigma^-$, $d^3\Delta$ and $a'^3\Sigma^+$ states are responsible for many of the perturbations to the $A^1\Pi$ state. These triplet states have been experimentally investigated in various studies [26 – 29]. A recent review paper Eidelsberg and Rostas (2003) [30] tabulates all transitions of

these perturbing states to the ground state $X^1\Sigma^+$. This includes theoretical wavelengths for all these expected singlet-triplet transitions as well as experimental wavelengths for those which have been experimentally observed. This clearly indicates expected transitions of which the wavelengths have not yet been confirmed by experimental measurements. The data contained in this paper are also found online [31], and are being updated regularly.

2.2 Vacuum ultraviolet laser spectroscopy of CO

Vacuum ultraviolet laser spectroscopy is a well-established technique and has been applied by many groups to a number of small molecules having excitation energies in the VUV, such as CO. Two extensive reviews are given in Vidal (1988) [32] and Yamanouchi and Tsuchiya (1995) [33].

The first laser excitation studies of the Fourth Positive System of CO were done using two-photon and three-photon absorption techniques, using commercial dye lasers operating in the visible or UV spectral ranges. This was followed by the use of VUV laser sources for single photon excitation, having a considerably higher transition probability and therefore increased sensitivity. Detection techniques employed in all the above-mentioned experiments comprised the total subsequent fluorescence detection from the excited states [34,35] or further laser ionisation from the excited state using visible lasers and subsequent ion detection [36].

This work was extended to the study of the singlet-triplet bands perturbing the $A^1\Pi$ state [27] and to the measurement of radiative lifetimes of particular rovibronic levels in these triplet states [28, 37]. Rotationally-resolved singlet-triplet lines of $^{13}C^{16}O$ were also observed in Klopotek and Vidal (1984) [27] but their wavelengths were not determined accurately.

Higher-lying states such as Rydberg levels were investigated by two-step excitation using one VUV laser source for excitation to an intermediate level (fixed) and a second laser source (tunable) for further excitation to higher-lying states, and subsequently detecting the laser-induced fluorescence from the upper level, or the laser-reduced fluorescence from the intermediate level, also called fluorescence-dip spectroscopy [38]. Other techniques include more complex pumping schemes and ion-dip spectroscopy, which is the ion detection analogue to fluorescence-dip spectroscopy. Various investigations of the Rydberg levels of CO using these techniques are

documented [37, 39 – 42].

In recent VUV laser spectroscopy of the Fourth Positive System of CO [33], also using a supersonic expansion, many lines of the $^{13}C^{16}O$ isotopomer were detected amongst the $^{12}C^{16}O$ lines, but no further investigations were carried out into detecting lines of the rarer isotopomers of CO.

The rarer isotopomers of CO have been studied by laser excitation in the extreme ultraviolet (XUV: $\lambda < 105$ nm) by identical methods to those above, the only difference being the shorter wavelength used in excitation. This XUV laser source and supersonic gas expansion setup is described in Levelt, Ubachs and Hogervorst (1992) [43] and Eikema, Hogervorst and Ubachs (1994) [44]. There are a number of publications reporting on the work of this group, with a representative example given by Ubachs, Velchev and Cacciani (2000) [45], in which all six stable isotopomers of CO could be detected by using enriched gas samples. The same group has previously used a VUV laser source in the range $105 - 109$ nm and natural CO gas to detect the four most abundant isotopomers of CO in the $C^1\Sigma^+$ state [46].

The methods employed in the present study are therefore widely applied to the VUV laser spectroscopic study of CO.

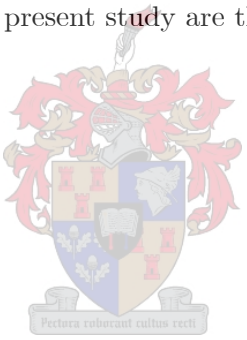

Chapter 3

Theory

3.1 Tunable vacuum ultraviolet laser radiation

There is a lack of commercial laser sources in the VUV, and none of the few available sources provide frequency tunable coherent radiation with a narrow spectral bandwidth. Nonlinear crystals are widely used for frequency conversion of commercial lasers such as dye lasers into the UV region, but become opaque below 200 nm, although recent advances suggest converted radiation can be obtained down to 170 nm in certain new crystals [47].

One of the most widely used processes for generating tunable VUV radiation is four-wave mixing, either by sum or difference frequency mixing, in gases and metal vapours. For gases, either a gas cell or a gas expansion into vacuum is employed as nonlinear medium. Both these methods are expensive on gas usage and extremely critical to impurities in the medium, requiring specialised vacuum equipment. For metal vapours, a heatpipe oven operating at high temperature is generally employed which generates a suitable homogenous medium of the metal vapour of interest. Metal vapours are attractive for frequency mixing due to their high nonlinear susceptibility. Complete reviews of VUV generation can be found in Eden (2000) [48] and Vidal (1987) [49] and the references therein.

The specific four-wave mixing process employed in our source comprises the interaction of visible laser pulses at frequencies ν_1 and ν_2 with a magnesium vapour medium to generate VUV light at the sum frequency (ν_{SF}):

$$\nu_{SF} = 2\nu_1 + \nu_2 \tag{3.1}$$

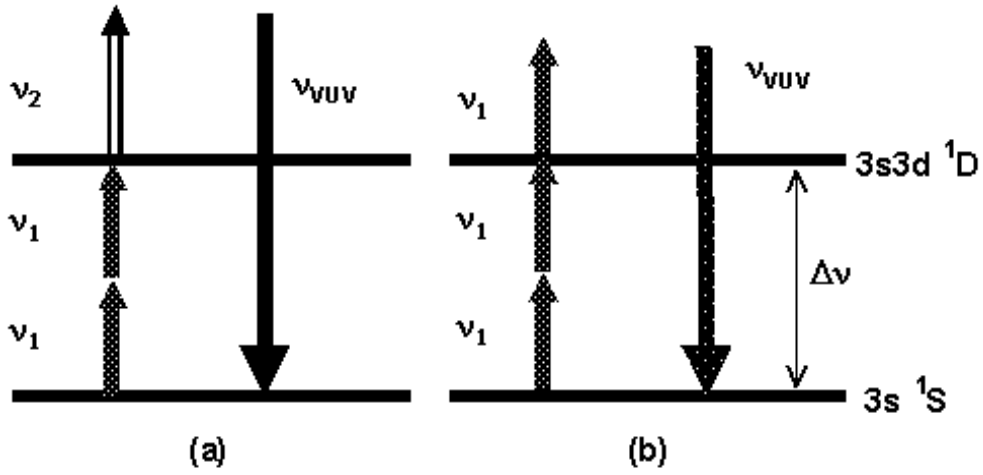

Figure 3-1: Energy level diagrams of the competing two-photon resonant four-wave mixing processes: (a) sum frequency mixing (SFM) and (b) third harmonic generation (THG). The atomic energy levels of magnesium giving the two-photon resonance are indicated.

The susceptibility for the conversion process is greatly enhanced by a resonance of one of the laser frequencies with a transition of the nonlinear medium. The choice of metal vapour medium is therefore often dictated by a suitable resonance. For the generation of VUV in the region $138 - 160$ nm the two-photon resonance of one of the dye laser frequencies ν_1 with the $3s^2$ $^1S - 3s3d$ ^1D transition of magnesium, as illustrated in Figure 3-1 (a), is favourable. The non-resonant dye laser frequency ν_2 can be tuned freely, generating a tunable VUV frequency at the sum frequency as indicated in Relation 3.1. This process is called two-photon resonant sum frequency mixing, and is referred to as SFM in this dissertation. The sum frequency component generated in the laser beam is referred to as the SF component.

The competing process in the present experimental setup is two-photon resonant third harmonic generation, referred to as THG in this dissertation. The third harmonic component is referred to as the TH component. This process is the degenerate case of the SFM described above when the third photon is not ν_2 but another ν_1 photon, therefore generating fixed-frequency VUV radiation (since the frequency ν_1 is fixed on the resonance). This process is illustrated in Figure 3-1 (b).

The process of THG is discriminated against by suitable polarisation of the laser beams.

By polarising the two laser beams of frequencies ν_1 and ν_2 circularly in opposite directions, angular momentum conservation allows the process of SFM and forbids the process of THG. This is discussed in detail in Steinmann (1999) [7]. However, a significant TH component is generated in the experimental setup due to the large susceptibility for the process and the imperfect circular polarisation of the incident laser beams.

The generated VUV is coherent and its bandwidth is determined by the bandwidth of the incident laser beams. If the bandwidth is described as a standard deviation, we find the following rule of thumb for the frequency bandwidth of the SF component ($\Delta\nu_{SF}$) as a function of the frequency bandwidths of the visible wavelengths ($\Delta\nu_1$ and $\Delta\nu_2$):

$$\Delta\nu_{SF} \simeq \sqrt{2(\Delta\nu_1)^2 + (\Delta\nu_2)^2} \tag{3.2}$$

Phase matching of the generated VUV and the incident visible laser radiation is required to optimise the conversion efficiency. This may be explained for SFM by linear momentum conservation, which can be expressed as follows for colinear beams:

$$\begin{aligned} p_{SF} &= 2p_1 + p_2 \\ n_{SF}\nu_{SF} &= 2n_1\nu_1 + n_2\nu_2 \end{aligned}$$

The phase matching condition differs for THG and is given by:

$$n_{TH}\nu_{TH} = 3n_1\nu_1$$

In these equations p_q is the linear momentum and n_q is the index of refraction of the medium for the component with the frequency ν_q.

Phase matching is achieved in the magnesium medium by addition of krypton gas and by fine-tuning the pressure ratio of magnesium vapour and krypton gas. The optimum phase-matching conditions are found at different pressure ratios for THG and SFM respectively.

3.2 Molecular states of carbon monoxide

3.2.1 Molecular energy states and selection rules

The transitions of interest in this study are individual rovibronic transitions of CO corresponding to transitions between vibrational levels v' of an upper electronic state ($A^1\Pi$) and the vibrational level $v'' = 0$ of the electronic ground state ($X^1\Sigma^+$). The previous pioneering study into the VUV laser spectroscopy of CO in our laboratory was done on the $A^1\Pi(v' = 3)-X^1\Sigma^+(v'' = 0)$ vibronic band and this transition is indicated by a vertical arrow in Figure 3-2. The $A^1\Pi$ vibrational levels investigated in the present study ($v' = 0 - 5$) are clearly indicated by solid horizontal lines in Figure 3-2.

The Fourth Positive System consists of $^1\Pi - ^1\Sigma$ transitions. The selection rules applicable to these specific rovibronic transitions are summarised below and can be found in more detail in Herzberg (1950) [51].

Transitions between different electronic states are only allowed between electronic states having the same spin quantum number S, as indicated by the Selection Rule 3.3:

$$\Delta S = S' - S'' = 0 \tag{3.3}$$

This implies that only singlet-singlet or triplet-triplet transitions are allowed.

The Selection Rule 3.4 for the total angular momentum quantum number J holds rigorously for electric dipole radiation:

$$\Delta J = J' - J'' = 0, \pm 1 \quad \text{with the restriction } J' = 0 \nrightarrow J'' = 0 \tag{3.4}$$

This results in allowed P, Q and R branches of rotational lines in a given vibronic band, according to the total angular momentum quantum number difference of +1, 0 or −1, as is indicated in Figure 3-3. These branches overlap, forming a band head on the short-wavelength side in the case of the Fourth Positive System of CO. In the figure, the Q(0), P(0) and P(1) transitions are indicated as dashed lines because they do not exist. The P(0) transition cannot exist due to the definition of the transitions, as is clearly indicated in the figure. The Q(0) line, or band origin, is forbidden due to the selection rule restriction of the total angular momentum,

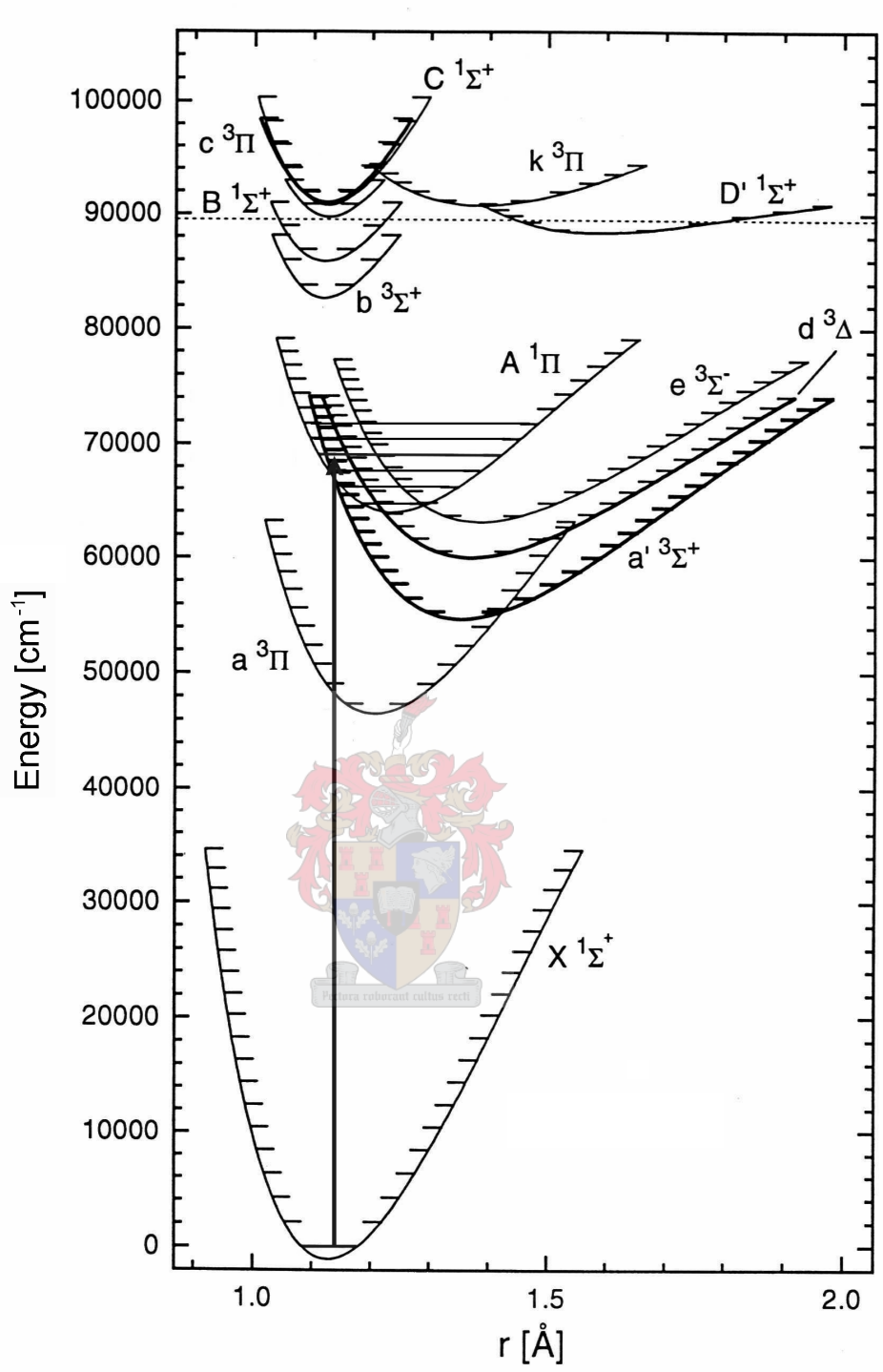

Figure 3-2: Potential energy curves of carbon monoxide, indicating electronic and vibrational states, and specifically the vibrational states of interest in the $A^1\Pi$ electronic state. This figure is taken from Mellinger (1995) [50] with permission from the author.

as indicated in Selection Rule 3.4. The P(1) line is additionally forbidden in the Fourth Positive System of CO due to an additional restriction placed on the upper electronic state. The upper state $A^1\Pi$ has angular momentum vector $\Lambda = 1$ (as indicated by the greek letter Π). For this reason, the upper state has only levels with $J = 1, 2, 3, ...(J \geq \Lambda)$. Transitions involving the level $J' = 0$ are therefore forbidden, such as Q(0) and P(1).[1]

In addition to the above-mentioned selection rules, only states with opposite symmetry may combine. This is indicated by the Selection Rule 3.5:

$$+ \longleftrightarrow -, + \nleftrightarrow +, - \nleftrightarrow - \tag{3.5}$$

Since the $A^1\Pi$ state has angular momentum $\Lambda = 1$, it undergoes Λ-type doubling of its rotational levels, each into close-lying positive and negative symmetry levels. Because the ground electronic state has $\Lambda = 0$, no splitting occurs in this state. The Selection Rule 3.5 therefore allows only transitions between levels of unlike symmetries, thereby preventing the observation of double lines in the P, Q and R branches. An improved and widely used description when refering to this symmetry is the concept of parity and the use of the labels e and f [52] to describe this characteristic. The levels with parities e and f are defined as follows for molecules having an even number of electrons (integral J values) as in the case of CO:

Levels with symmetry $+(-1)^J$ are called e levels

Levels with symmetry $-(-1)^J$ are called f levels

For molecules having an uneven number of electrons (half-integral J values) the following holds:

Levels with symmetry $+(-1)^{J-\frac{1}{2}}$ are called e levels

Levels with symmetry $-(-1)^{J-\frac{1}{2}}$ are called f levels

The Selection Rules 3.4 and 3.5 in the new notation become:

[1] Q(0) is therefore forbidden by two different selection rules in this case.

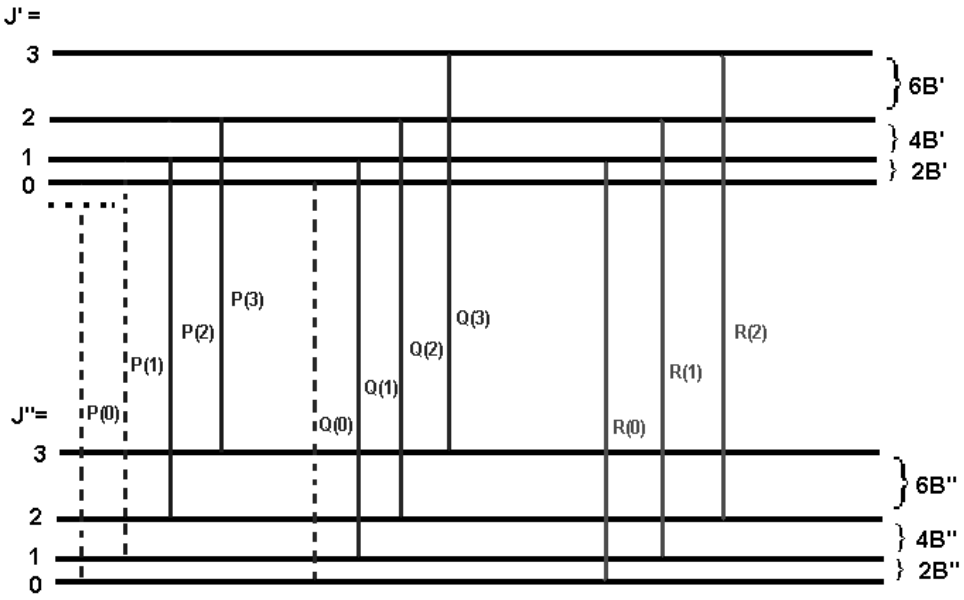

Figure 3-3: Rovibronic transitions between different vibronic states. The allowed P, Q and R branch transitions are indicated by solid vertical lines and the forbidden transitions by dotted lines. As indicated P(0) cannot exist. P(1) and Q(0) are forbidden, specifically in CO. B′ and B″ are the rotational constants of the upper and lower vibrational states respectively.

$$\Delta J = 0, e \leftrightarrow f \tag{3.6}$$

$$\Delta J = \pm 1, e \leftrightarrow e \text{ and } f \leftrightarrow f \tag{3.7}$$

There is no stringent selection rule governing vibronic transitions, therefore transitions between the $v'' = 0$ vibrational level of the ground state $X^1\Sigma^+$ and all of the upper state $A^1\Pi$ vibrational levels v' are possible. However, the Franck-Condon principle, namely that the transition probability is proportional to the spacial overlap of the wavefunctions of the lower and upper vibronic states, applies.

3.2.2 Calculation of rovibronic transition energies

Calculating transition energies from term values

The term values of molecular spectra tabulated in many publications correspond to the total energy of the level in relation to the lowest level, which is taken to have energy $E = 0$. These term values should be converted to transition energies, to be useful for identification of spectral lines or as wavelength standards, as in this work.

For the Fourth Positive System of $^{12}C^{16}O$, accurate term values for the ground state $X^1\Sigma^+$ and the excited state $A^1\Pi$ are found in Morton and Noreau (1994) [9] and Le Floch (1992) [21] respectively. The term values of the ground state $X^1\Sigma^+$ may be calculated from mass-independent Dunham parameters for all isotopomers of CO [20]. Excited state term values (for the $A^1\Pi$ state) for $^{13}C^{16}O$ are tabulated in Haridass and Huber (1994) [23], while those for $^{12}C^{18}O$ are tabulated in Beaty *et al.* (1997) [24]. No such values are known yet for $^{12}C^{17}O$.

The Parity Selection Rules 3.6 and 3.7 must be obeyed in transitions. Since the electronic ground state $X^1\Sigma^+$ does not undergo Λ-type doubling, its levels are by definition all of parity e. The $A^1\Pi$ state does undergo Λ-type doubling, its levels are doublets of parity e and f.

As a result the transition energies of the P, Q and R branches are calculated by:

$$\begin{aligned} E_{P(J'')} &= E'_e(v', J' = J'' - 1) - E''_e(v'' = 0, J'') \text{ for } J \geq 2 \\ E_{Q(J'')} &= E'_f(v', J' = J'') - E''_e(v'' = 0, J'') \text{ for } J \geq 1 \\ E_{R(J'')} &= E'_e(v', J' = J'' + 1) - E''_e(v'' = 0, J'') \text{ for } J \geq 0 \end{aligned}$$

Although calculated transition energies for $^{12}C^{16}O$ and $^{13}C^{16}O$ are published in Morton and Noreau (1994) [9] for levels having $J \leq 6$, the transition energies for the Fourth Positive System with $v' = 0 - 5$ were re-calculated in the above-mentioned manner in this study for all available J values for these isotopomers and also for the $^{12}C^{18}O$ isotopomer, from original term values.

Calculating transition energies using molecular constants only

The process of calculating transition energies from molecular constants is useful for finding the expected wavelength positions of rovibronic lines. Since the isotopomer lines of interest in this work have not been detected before, calculations of expected line positions have to be made for accurate identification of these lines. Although these calculations are imperfect, it provides a starting point for identification of unknown lines and provides a first-order representation of molecular parameters and also results in an improved conceptual understanding.

The energy of a specific rovibronic transition is given by:

$$\begin{aligned} E_{transition} &= E' - E'' \\ &= (T'_e - T''_e) + (G' - G'') + (F' - F'') \end{aligned}$$

where $(T'_e - T''_e)$ is the electronic contribution, $(G' - G'')$ is the vibrational contribution, and $(F' - F'')$ is the rotational contribution. These terms can be calculated from molecular constants as follows.

The electronic contribution $(T'_e - T''_e)$ is known and for the CO Fourth Positive System this value is given in Huber and Herzberg (1979) [53], as are the constants in the relations below. The vibrational contribution is given by:

$$G(v) = \omega_e(v + \frac{1}{2}) - \omega_e x_e(v + \frac{1}{2})^2 + \omega_e y_e(v + \frac{1}{2})^3 + ...$$

where ω_e, $\omega_e x_e$ and $\omega_e y_e$ are molecular constants of each electronic state.

The rotational contribution is given by:

$$F(v, J) = [B_e - \alpha_e(v + \frac{1}{2})]J(J + 1) - [D_e + \beta_e(v + \frac{1}{2})]J^2(J + 1)^2 + ...$$

where B_e, α_e, D_e and β_e are molecular constants of each electronic state.

The relations above were used to calculate expected line positions of $^{12}C^{16}O$ and $^{13}C^{16}O$, for initial line identification before calibration and for identification of $^{12}C^{18}O$ and $^{12}C^{17}O$ lines.

The above relations are a simplified representation of the more accurate Dunham expression, which allows the calculation of the term energies for a given state from a single mass-independant

expression, for all isotopomers of CO. The applicable Dunham parameters for the ground state of CO may be found in George *et al.* (1994) [20]. Dunham parameters are not yet accurately known for the $A^1\Pi$ state, but may be derived in the future, using literature values for the term values of the different isotopomers of CO.

3.3 Supersonic expansion

Supersonic expansions or jets offer extremely favourable conditions for molecular spectroscopy [54]. These conditions are: (i) the low translational temperature resulting in simplified spectra and increased signal strengths of the low-J lines, and (ii) the relatively high sample density in the interaction region, also increasing the signal strengths. The theoretical description and experimental setup of the supersonic expansions used in this work have been described in detail in Steinmann (2003) [1].

A schematic illustration of a supersonic expansion is given in Figure 3-4. A pulsed gas jet (not necessarily supersonic) consists of molecules passing from a high-pressure reservoir through a small orifice into a vacuum chamber during the short period of time that the pulsed valve opens the orifice. Such a gas jet is termed supersonic when the mean velocity of the molecular flow becomes larger than the speed of sound in the expanding gas. This occurs physically when the mean free path length of the molecules in the reservoir is smaller than the size of the orifice [8].

The temperature of the gas sample influences the relative intensities of lines in experimentally recorded spectra. Figure 3-5 shows the expected relative populations of the different rotational levels of the lowest vibrational level of the electronic ground state as calculated from the Boltzmann distribution for different rotational temperatures, normalised to represent the same number of molecules. The lowest temperatures result in the lowest levels having the highest populations.

The supersonic expansion is advantageous in these spectroscopic investigations since the population of the rotational levels in the $v'' = 0$ lower state will affect the signals obtained for low-J lines in a LIF spectrum. The lines of interest in this study are generally the lowest-J lines. In a cold sample compared to a warmer sample of equal density, the $J'' = 0$ level will have

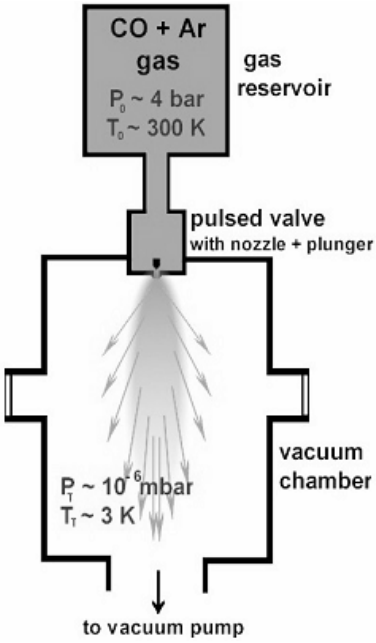

Figure 3-4: Illustration of the generation of a supersonic expansion. Typical pressures and temperatures are indicated. This figure is taken, with permission, from a presentation of C.M. Steenkamp.

a higher relative population. Therefore the allowed transitions from the $J'' = 0$ level especially, which is only R(0) in this case, will have the highest intensity of the lines in the R-branch. The significant cooling obtained in the supersonic expansion greatly simplifies the recorded spectra by decreasing the intensity of higher-J lines in this manner and increasing intensities of lower-J lines.

In summary, the low temperature obtained with the supersonic expansion allows the detection of the low-J lines of the rare isotopomers in a natural CO sample, which would otherwise have remained below the noise level. The low-J lines detected in the supersonic expansion are also the lines of interest in astrophysics, due to similarly low temperature conditions in the interstellar medium. The low temperature has the additional advantage of simplifying the spectra, as compared to room-temperature measurements.

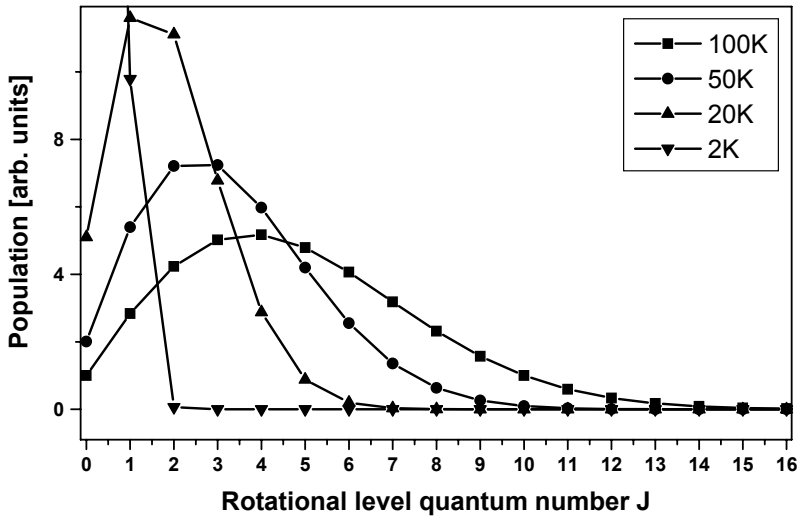

Figure 3-5: The calculated relative populations of the CO ground state rotational levels for different temperatures. The usual working range in the present study was in the range $2 - 20$ K.

3.4 Laser induced fluorescence and absorption spectroscopy

Laser induced fluorescence spectroscopy is a description for the process of fluorescence detection after excitation of a sample with narrow-bandwidth laser light. There are two types of laser induced fluorescence spectra: (i) laser induced fluorescence excitation spectra, and (ii) dispersed fluorescence spectra.

In laser induced fluorescence excitation spectroscopy a tunable laser is used to excite the sample and this excitation is recorded as a function of the laser wavelength, by the detection of the total subsequent fluorescence at a specific wavelength. The spectral resolution is limited by the laser bandwidth or atomic or molecular linewidth, whichever is larger.

In dispersed fluorescence spectroscopy the sample is excited by laser radiation and the subsequent fluorescence is analysed by a spectrometer, yielding information on the de-excitation pathways. The spectral resolution is limited to the resolution achievable by the spectrometer; which is generally much larger than laser bandwidths or atomic or molecular linewidths.

In this study the laser induced fluorescence excitation spectroscopy technique was used. The

acronym LIF refers specifically to this spectroscopic technique throughout this dissertation.

In this experimental investigation an absorption spectrum could be measured simultaneously with the LIF spectrum by recording the energy of the laser pulse after interaction with the sample. Absorption spectra using pulsed lasers are not generally accepted as useful sources of information, because of their relatively low signal-to-noise ratios. However, in this work the measured absorption spectra have useful signal-to-noise ratios, as will be discussed.

Chapter 4

Experimental setup

4.1 Basic experimental setup

The experimental setup used in the present study is illustrated schematically in Figure 4-1. This setup is essentially the same as that used previously in our laboratory [1,10] and the modifications since the earlier work are discussed in Section 4.3, as well as in Steinmann, Du Plessis and Rohwer (2005) [25] and Du Plessis, Steinmann and Rohwer (2005) [55]. In Figure 4-1 the experimental setup is divided into three sections for simplicity: the vacuum ultraviolet laser source, the setup for LIF measurement, and the setup for absorption measurement. These sections are briefly discussed below.

The vacuum ultraviolet laser source can be described as follows. A XeCl excimer laser (Lambda Physik EMG203 MSC; 308 nm; pulse energies typically between 80 and 150 mJ; pulse duration 25 ns) is used to pump two dye lasers simultaneously (both Lambda Physik FL3001X; pulse energies typically between 0.1 and 2 mJ; pulse durations 20 ns). In this work the following dyes were used: *PBBO* (tuning range 378-413 nm), *stilbene 3* (412-435 nm), *coumarin 440* (415-472 nm), *coumarin 480* (457-517 nm), *coumarin 540A* (516-608 nm). The estimated bandwidth of the dye laser output is in the range $0.19 - 0.37$ cm^{-1} [56]. The estimated bandwidth of the VUV, using Equation 3.2, is then in the range $0.39 - 0.50$ cm^{-1}. This corresponds to an estimated wavelength bandwidth in the range $0.8 - 1.1$ pm, although this may be an exaggerated estimate.

The dye lasers beams, mostly in the visible wavelength range, are polarised circularly

in opposite directions by polarising elements not shown in Figure 4-1 and combined colinearly in a Glan Taylor prism (P1 in Figure 4-1). The combined beams are focused into the magnesium-krypton medium inside the heatpipe oven, where conversion to the vacuum ultraviolet takes place. This conversion takes place by resonantly-enhanced sum frequency mixing in the magnesium medium, to which krypton was added to ensure phase matching at a ratio $P_{Kr}.P_{Mg} \approx 13:1$. The generated coherent vacuum ultraviolet light propagates colinearly with the remaining visible beams, through a magnesium fluoride window into the vacuum system.

The LIF measurement occurs inside the vacuum system, which is maintained at 5×10^{-6} mbar by a turbomolecular pump (Pfeiffer TPH200) backed by a rotation pump (VacuuBrand RS15). A supersonic expansion is generated by allowing the sample gas to expand from a stagnation pressure of typically 4 bar through a nozzle (0.8 mm diameter) of a solenoid pulsed valve (General Valves series 9) into the vacuum chamber. The sample gas consisted of CO, to which Argon was sometimes added to act as the carrier gas for more efficient cooling.

The beam of coherent VUV light crosses the molecular beam perpendicularly, at a distance of 25 nozzle diameter lengths below the nozzle (20 mm). The gas and laser pulses are synchronised by a delay generator (Stanford Research Systems DG535). The pulsed valve is driven by a pulsed valve driver (Iota One Pulse Driver, General Valve Corporation), allowing the generation of stable pulses of durations down to 170 μs (physical limit). The VUV fluorescence from the irradiated volume of the jet is detected by a solarblind photomultiplier tube (EMR 542G-08-18-03900) positioned perpendicular to the laser beam and the direction of gas expansion (PMT1 in the figure).

The setup for absorption measurement consists of a VUV monochromator (McPherson Model 218) attached to the above-mentioned vacuum system, and separated by a magnesium fluoride window. This system is separately evacuated by a diffusion pump (Edwards Difstak 63) and liquid-nitrogen-cooled cold trap, backed by a rotation pump (Alcatel 2008A). The transmitted laser beam (consisting of the visible dye laser components as well as two vacuum ultraviolet components) is sent through the monochromator for separation of the different wavelength components and selective transmission of the tunable VUV component is made possible. The detector connected to the exit slit of the monochromator is also a solarblind photomultiplier (Hamamatsu R973 - PMT2 in Figure 4-1).

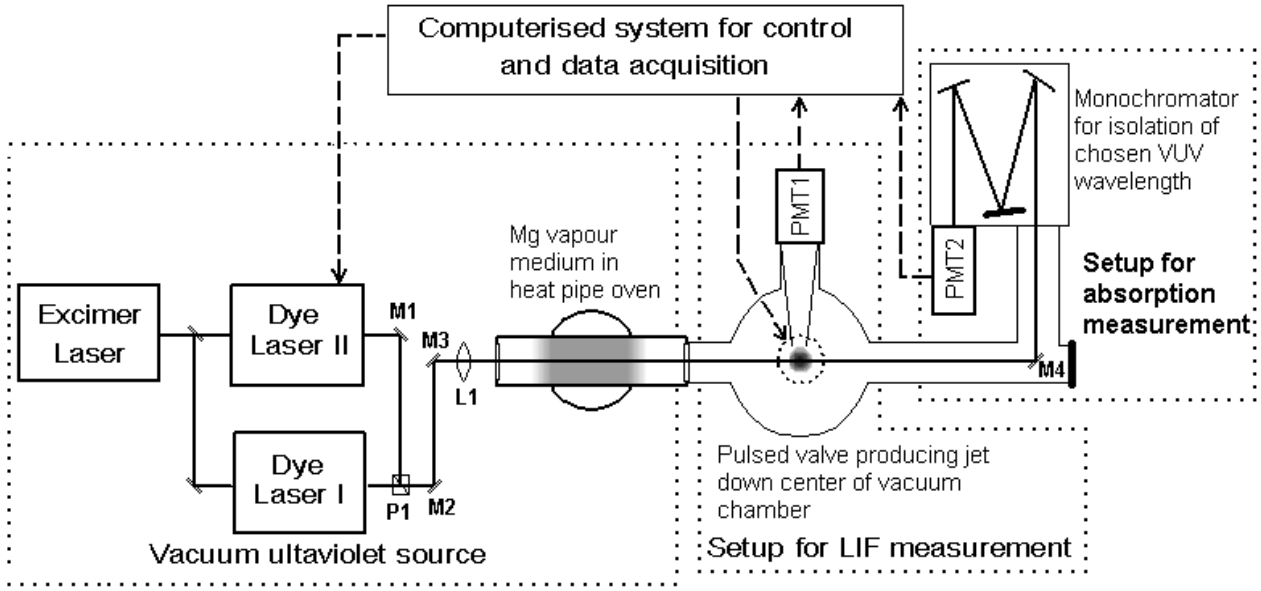

Figure 4-1: Schematic illustration of the experimental setup used in this work, divided by the dotted lines into the VUV laser source, the setup for LIF measurement, and the setup for absorption measurement.

4.2 Experimental method

4.2.1 Startup procedure

Beam alignment

Initial beam alignment is done by visual alignment of the visible dye laser beams through the vacuum system that is opened at the position of mirror M4 (see Figure 4-1). The resonant dye laser beam (dye laser I) is used as reference, as the alignment of the other dye laser beam (dye laser II) can be adjusted independently to follow this path. The resonant dye laser beam is aligned for optimal transmission through the heatpipe oven and vacuum system, as well as the monochromator when it is used.

This alignment through the centre of the heatpipe and vacuum chamber is done by two mirrors in the beam path M2 and M3, after the beam combination prism P1 and before the focusing lens L1. Mirror M4 is removed in order to do this alignment and, when necessary, a

helium-neon laser is aligned from the position of M4 backwards through the optical setup to find the optimal alignment.

The alignment is critical in order to have minimal obstruction of the laser beams by crystals formed in the heatpipe (which are more abundant closer to the walls of the heatpipe), and to intersect the centre of the gas expansion (for maximal gas density and other considerations which will be discussed later). After this alignment, mirror M4 is replaced. This mirror is used to reflect the laser beam either directly onto the photomultiplier tube or through the monochromator and then onto the photomultiplier tube, when this is added to the setup. Alignment of the beam through the monochromator is done using fine adjustment of this mirror M4 and inspecting the visible transmission with the grating angle set to the applicable visible wavelength. This setting is changed to the applicable VUV region after alignment.

Reaching operating conditions

The process of bringing the experimental apparatus to operating conditions for experimental investigations can be briefly described as follows. The heatpipe oven is brought to a stable operating condition at a temperature in the range $700-850\,^{\circ}\mathrm{C}$, determined by the exact pressure of the external argon volume. The dye laser energies are measured and the non-resonant dye laser is aligned colinear to the resonant laser beam by inspecting the visual overlap of the laser spots in the near field and far field. This is done by adjusting the beam combination prism P1 and the mirror reflecting the non-resonant laser into the prism M1.

Once the operating temperature of the heatpipe has been reached and the vacuum system has reached a suitable vacuum, the photomultiplier tube is used for detection of the VUV signal on the oscilloscope. This signal strength is optimised by fine adjustment of the beam overlap and optimisation of the resonant laser wavelength. Phase matching curves are also measured at this stage, in order to optimise the VUV yield under the given working conditions. This should be done systematically due to the large number of variables in the system.

4.2.2 Measurement techniques

Recording of spectra

The experimental LIF and absorption spectra are recorded using a computer interface and a custom HPVEE program as used in the previous study [1]. Prior to any measurements, the appropriate mixture of sample gas is prepared in the gas reservoir and the pulsed valve driver is set to the required pulse duration. An appropriate temporal delay between the gas pulse and the laser pulse is chosen for optimal intersection. A signal proportional to the LIF or transmitted VUV respectively is obtained by integrating the photomultiplier tube signal over the laser pulse period using a boxcar integrator. These boxcar integrators are set such that the fluorescence signal is integrated over the temporal peak of the fluorescence, typically $\frac{1}{3}$ of the fluorescence signal width (FWHM). An average over 10 signals is taken for a single recorded data point.

Delay scans

A delay scan is a measurement of the LIF and absorption signals as a function of delay time between gas and laser pulses. A delay scan is therefore a temporal measure of the LIF and absorption signals, while the wavelength is fixed on one of the rotational lines such as R(0). The signals are measured as a function of delay between gas and laser pulses, by measurement of the signals from different pulses at different delay time settings. Delay scans are used to find the optimal delay setting for spectral measurements.

Typical conditions

Specific operating conditions for all recorded spectra presented in this dissertation are included in the descriptions in Appendix 8.1. Typical operating conditions are summarised below.

Most spectra were recorded at a repetition rate of 5 Hz, as is described in the next section. This repetition rate refers to the physical laser and gas pulses. A burst of 10 laser shots was used to determine an average for each data point. Most experiments used a 100% CO sample gas mixture, at typically 4 bar stagnation pressure of the sample gas volume. Most experimental spectra were recorded using 1.5 pm wavelength step sizes of the visible dye laser wavelength.

The translated VUV step sizes are wavelength dependent and range between the extremes of 0.1 pm around 139 nm and 0.2 pm around 154 nm. Other parameters will not be dealt with here and may be found in Appendix 8.1.

The monochromator was used for wavelength separation of the SF and TH components. In a typical experiment with the monochromator, a central wavelength position is chosen and optimised for VUV transmission, and the exit slit opened to a relatively wide position, enough to transmit a broad range of SF wavelengths but none of the TH component at 143.6 nm.

4.3 Modifications to the setup

During this study, the experimental setup and measurement process was optimised in a number of ways. These are discussed briefly in the next paragraphs. Experimental results pertaining to these experimental improvements are not included in this dissertation, but have been published [55]. More details regarding the addition of the monochromator are included in Huang (2004) [57].

4.3.1 Repetition rate

The experimental procedure in the past included measuring spectra at a repetition rate of 1 Hz. The recording of spectra at this rate is very slow and increases the possibility of changes in the experimental parameters. The recording of spectra at higher repetition rates was investigated in this study. Only above 10 Hz do changes to the spectra and delay scans become observable due to the limited pumping capacity, for removing background gas between pulses. This increased background gas pressure disrupts the gas expansion and increases the temperature, although it does not have any effect on the absolute accuracy of spectral results obtained. The limiting factor however is the possibility of damaging the photomultiplier tubes at higher pressures, as they may become damaged when the background gas pressure between pulses is increased. It was decided to do most experimental investigations in this study at 5 Hz. This is a good compromise between time taken for recording of spectra and maintaining the background pressure below 10^{-4} mbar.

4.3.2 Pulsed valve driver

A home-built driver used in previous work was replaced by the Iota One Pulse Driver Series 9 from General Valve Corporation, manufactured for the General Valve Corporation Series 9 solenoid pulsed valves.

The previous driver was not able to supply the specified peak voltage, although it did manage to open the valve. The new driver's peak voltage meets the specifications of the valve. The previous driver also had serious problems of pulse instability (probably due to the lower peak voltages or peak voltage instability), especially at higher repetition rates and at short pulse durations below 1.5 ms [1]. The new driver was used in this work at a wide range of pulse durations and repetition rates and found to be extremely stable under all these conditions. This finding is based partially on visual observation of the pulse pressures on the pressure gauge of the vacuum system, and also substantiated by experimental results. The pulse duration limitation (shortest possible pulses) of the old driver was approximately 1 ms. The new driver is able to generate pulses down to 300 μs in this study, as experimentally observed in the regime of pressures used. This is a vast improvement, especially when taking into account the improved stability and repeatability of these pulses. Short pulses are generally preferable for supersonic expansions, as they result in the coldest temperatures obtainable.

4.3.3 Monochromator

The transmitted VUV, after the intersection with CO in the supersonic expansion, has previously been detected by a solarblind photomultiplier tube directly after the intersection region (in transmission). This gives a simultaneous measurement of the non-interacting TH and the transmitted SF radiation. The absorption spectra were used as an online monitor of the VUV energy. Decreases in VUV energy occur occasionally due to crystal growth in the heatpipe or other factors. Such effects should be corrected immediately for usefulness of the recorded results. The spectra were also used in data analysis, as will be explained, but the signal-to-noise ratio of such pulsed absorption spectra have in the past not been found useful as sources of spectral data.

In the present study a vacuum monochromator was used to separate the different wavelength components. A solarblind photomultiplier tube was connected to the exit slit of the

monochromator. This allowed the selective detection of the vacuum ultraviolet component of interest, ignoring the other VUV component and visible components.

The aim of this addition to the experimental setup was twofold. Firstly, the separation of the VUV components, which are generated in the heatpipe, allows an improved characterisation of the VUV source. Secondly, the measurement of useful absorption spectra was demonstrated with this addition to the setup.

Chapter 5

Experimental results

All experimental results of interest are presented and described in detail in this chapter. The results in each section of this chapter are discussed in the corresponding sections of Chapter 6.

5.1 Characterisation of the VUV source

The VUV source used in this work has been characterised and optimised for use in the range $143 - 145$ nm in the work of C.M. Steinmann [1,7]. In the present study the addition of a vacuum monochromator to the experimental setup has allowed the improved characterisation of this laser source. The monochromator is used to separate the spectral components of the transmitted laser beam. The transmitted beam contains two visible dye laser frequencies and two VUV components: the SF and TH as discussed in Section 3.1. The characteristics of the SF and TH components are of particular importance, since the SF component is the useful component for laser excitation in the experiment. The TH component is an unwanted but inevitable component, as it is a competing nonlinear process in the VUV source. In previous work the TH and SF components could not be measured independently [1].

In the present study the possibility of measuring the TH and SF components independently, by using the monochromator, made it possible to characterise the nonlinear processes better and to optimise the useful SF component. Optimisation of the SF component is often done by adjusting the phase-matching factor, by adjustment of the krypton gas pressure in the heatpipe oven. This adjustment changes the relative amount of krypton gas in the magnesium-krypton

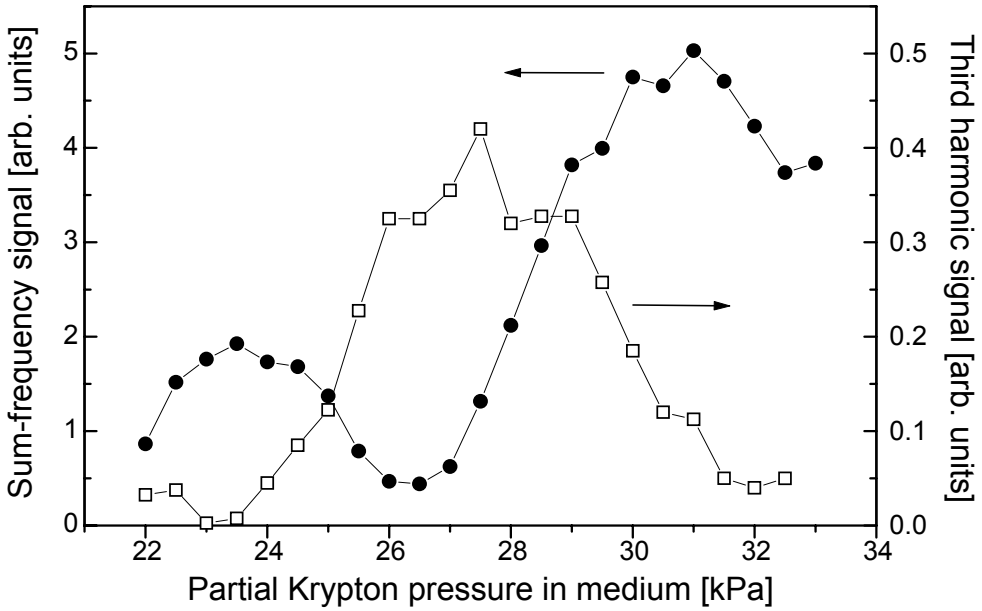

Figure 5-1: Example of phase-matching curves of the TH and SF components separated using the monochromator. Peaks are found for these different components at different pressures of the krypton gas. The partial Mg vapour pressure was ~ 2 kPa.

medium, thereby changing its index of refraction. Separate phase-matching curves for the SF and TH components were measured under different conditions in the present study.

The phase-matching curves of the SF and TH components at 148.7 nm and 143.6 nm respectively for a heatpipe temperature of $\sim 750\ ^{\circ}C$ are shown in Figure 5-1. The optimal peak of the SF component is at a partial Kr pressure of approximately 31 kPa, whereas the peak of the TH component is at approximately 27 kPa.

It was found that the phase-matching curve for SFM changes with wavelength, having peak values at different Kr pressures for different incident wavelengths. This is especially important to the wavelength regions of the different vibronic bands of CO. The shift in the peak position of the phase-matching curve is typically of the order of 1 kPa towards higher pressure per 1 nm wavelength increase. Therefore small wavelength increments (of 1.5 pm) have little or no effect on phase matching, which is a positive result in view of the continuous tuning of the VUV wavelength employed in the spectroscopic technique.

It was found that the phase-matching curve for THG is entirely independent of changes in

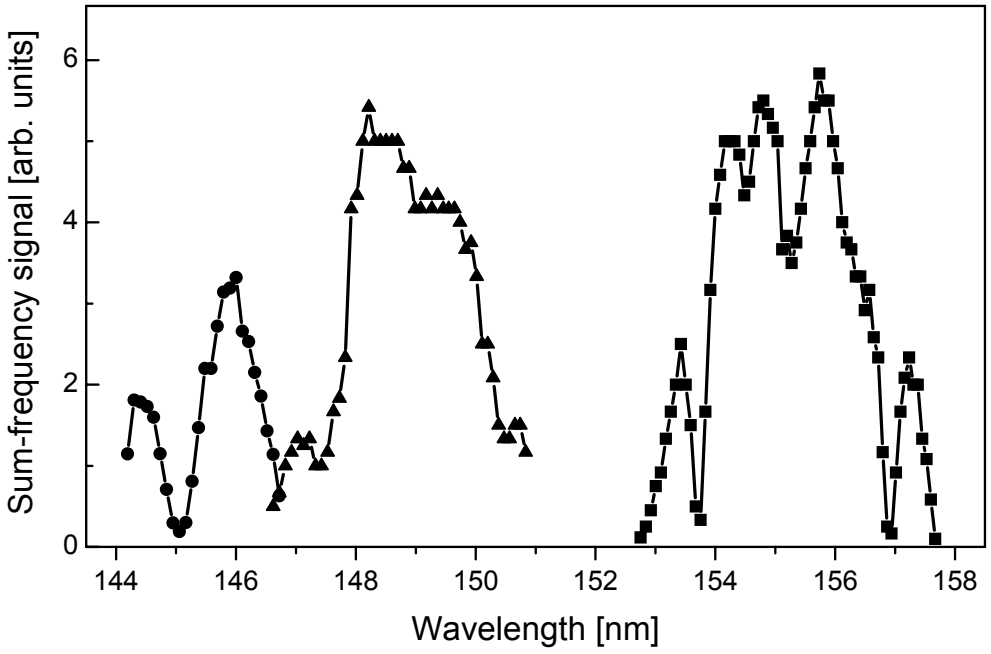

Figure 5-2: Wavelength tuning curves in the VUV using *coumarin 440* (•), *coumarin 480* (▲) and *coumarin 540A* (■), indicating the wide tunability available. The absorptions are most likely due to atomic auto-ionisation levels of Mg and are slowly varying over short wavelength regions. Gaps in this graph may be filled by using different dyes of the non-resonant dye laser.

the wavelength of the SF component, and therefore constant within a given experiment.

For both SFM and THG it was found that the effect of incident laser energy and heatpipe conditions affects the phase-matching conditions. Unfortunately no definite rule-of-thumb could be derived from these results, due to the large number of variables in the system.

As an indication of the wavelength tunability in the VUV, tuning curves measured using three different dyes of the non-resonant dye laser are shown in Figure 5-2. The dyes *coumarin 440*, *coumarin 480* and *coumarin 540A* cover the regions of interest for measurement of the CO Fourth Positive System bands with $v' = 0 - 3$. The other two vibronic bands measured in this study were the bands with $v' = 4 - 5$, corresponding roughly to the regions around 139 nm and 141 nm. This required the use of the dyes *stilbene 3* and *PBBO*.

Figure 5-2 clearly shows a number of dips corresponding to VUV wavelength ranges that are absorbed more strongly by the magnesium or krypton in the heatpipe. These are likely

caused by auto-ionisation levels of the Mg vapour.

5.2 Introduction to experimental measurements

5.2.1 LIF and absorption spectra

A typical measurement over a small section of a vibronic band is presented in Figure 5-3. This figure depicts, from left to right, the R(3), R(2), R(1) and R(0) lines of the $A^1\Pi(v' = 3)-X^1\Sigma^+(v'' = 0)$ band. The position of the R(3) line is also the band head of this band. The solid circles in the lower half of the figure represent the data points from the LIF measurements and the hollow squares in the upper half of the figure represent the data points from the absorption measurements.

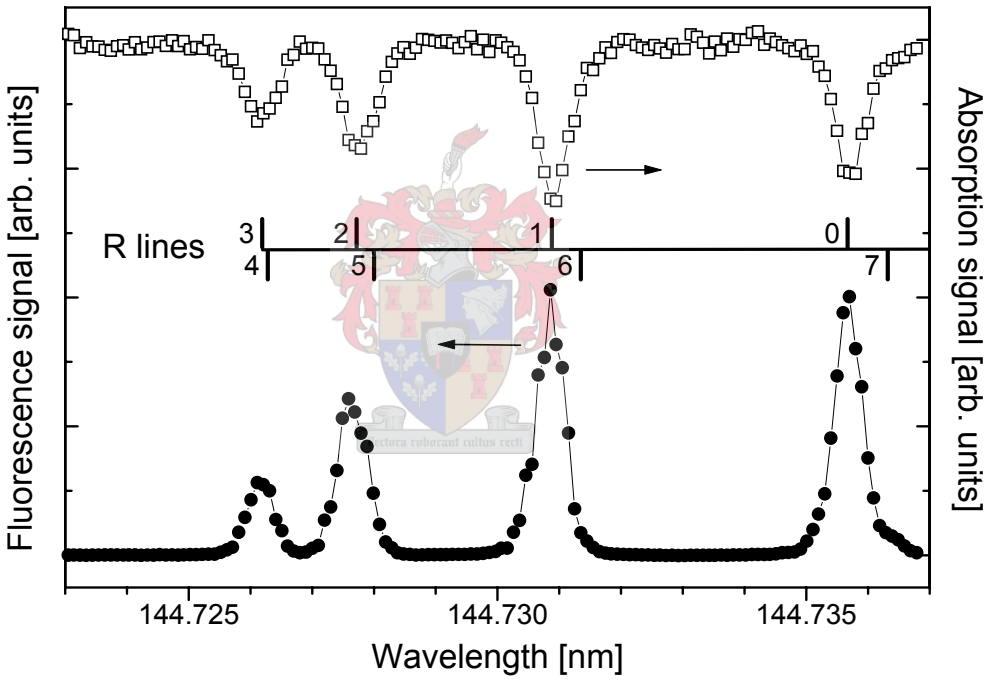

Figure 5-3: Example of LIF (•) and absorption (□) spectral lines near the $A^1\Pi(v' = 3)-X^1\Sigma^+(v'' = 0)$ band head region, indicating typical signal-to-noise ratios and linewidths.

The LIF spectrum is recorded on a zero background, the only noise originating from the photomultiplier tube detector and the boxcar integrator. The signal-to-noise ratios of these

lines are typically up to 500 : 1.

The absorption spectrum is recorded on the background of the VUV energy, which has a significant pulse-to-pulse fluctuation due to the nonlinear character of the VUV generation process. Nevertheless, the lines of the absorption spectrum have typical signal-to-noise ratios of up to 50 : 1. The background baseline of the absorption spectrum was observed to drift slowly as the total VUV generated in the heatpipe changes with time. Such changes may be caused by temporal changes in the heatpipe operating characteristics or the dye laser pulse energies.

The linewidths of the spectral lines of both the LIF and absorption spectra were typically $0.4 - 0.8$ pm (FWHM). Some line broadening effects were observed under certain experimental conditions and are mentioned in Section 5.3.4. The theoretical natural linewidths of these lines are much narrower than this but the combination of possible power broadening of the lines and the limitation of the laser bandwidth results in the measured spectral linewidths.[1]

5.2.2 Calibration of spectra

The experimental spectra were calibrated using the known $^{12}C^{16}O$ and $^{13}C^{16}O$ lines as wavelength standards in the VUV. In the present study all spectra were calibrated using the wavelength data of Morton and Noreau (1994) [9] and therefore only lines with $J' \leq 6$ were used in calibration. This choice not to use data from older literature was made in an effort to minimise calibration uncertainty and was based on the wide use of this set of data in contrast to older data. Further discussion of this calibration choice can be found in the next chapter.

After calibration of the spectra by the method outlined above, the subsequent $^{12}C^{16}O$ and $^{13}C^{16}O$ line wavelengths of the calibrated spectra could be compared to their corresponding literature wavelengths. The difference between the calibrated wavelength, termed the observed wavelength, and the literature wavelength used in the calibration is ideally very close to zero. This difference serves as an indication of the error margin of the calibration, the experimental measurement or the literature values, whichever has the largest error margin. The collection of above-mentioned differences is shown in Figure 5-4 for all six bands of interest, where each data point represents one spectral line of $^{12}C^{16}O$ or $^{13}C^{16}O$. The differences between the calibrated observed wavelengths and literature wavelengths are scattered around zero in each band and

[1] The measured spectral linewidth is therefore an indication of the laser bandwidth.

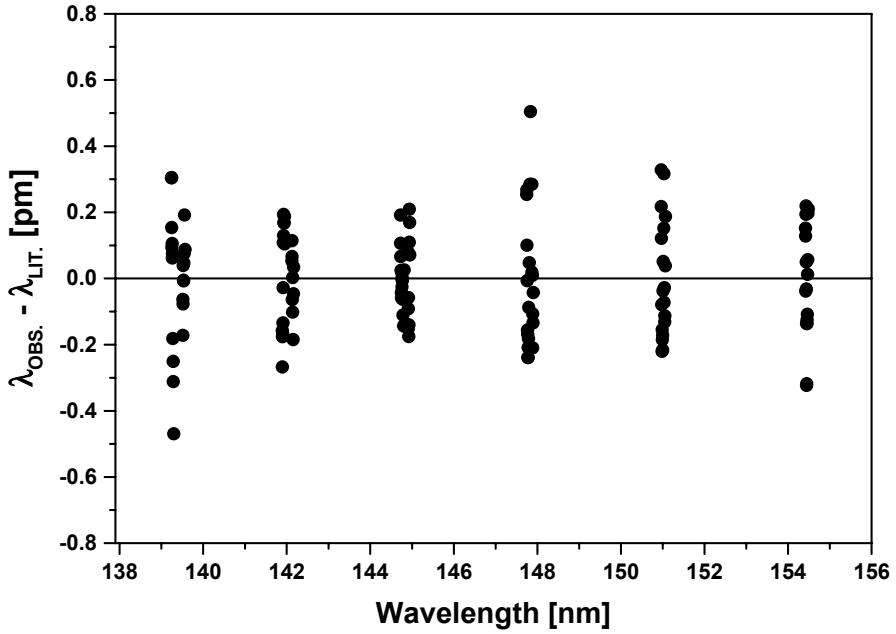

Figure 5-4: Difference between calibrated observed wavelengths ($\lambda_{OBS.}$) and the corresponding literature wavelengths that were used in the calibrations ($\lambda_{LIT.}$). The data of all observed $^{12}C^{16}O$ and $^{13}C^{16}O$ lines in spectra of all six vibronic bands are combined here.

have standard deviations of between 0.11 and 0.21 pm (calculated in each band separately). The average is 0.17 pm. Details are presented in Table 5.1.

Table 5.1: Standard deviations of calibration data in each vibronic band

Band label	**Standard deviation [pm]**	**Mean [$\times 10^{-18}$ m]**
$A^1\Pi(v'=0)$–$X^1\Sigma^+(v''=0)$	0.174	-6.52
$A^1\Pi(v'=1)$–$X^1\Sigma^+(v''=0)$	0.176	-2.87
$A^1\Pi(v'=2)$–$X^1\Sigma^+(v''=0)$	0.206	-9.49
$A^1\Pi(v'=3)$–$X^1\Sigma^+(v''=0)$	0.108	12.6
$A^1\Pi(v'=4)$–$X^1\Sigma^+(v''=0)$	0.141	12.0
$A^1\Pi(v'=5)$–$X^1\Sigma^+(v''=0)$	0.193	10.0

5.2.3 Delay scans

Typical LIF and absorption delay scans of the R(2) line of the $A^1\Pi(v' = 3)-X^1\Sigma^+(v'' = 0)$ band of $^{12}C^{16}O$ are depicted in Figure 5-5.[2] This measurement was taken with the previous pulsed valve driver as discussed in Section 4.3.2, generating a pulse duration of approximately 1.3 ms. The typical features of the LIF delay scan are the fast rise in fluorescence signal, followed under some conditions by a plateau or dip region, and the eventual decrease in signal. The delay scan of the absorption measurement shows a slower increase in absorption and a much higher background absorption after the gas pulse has passed.

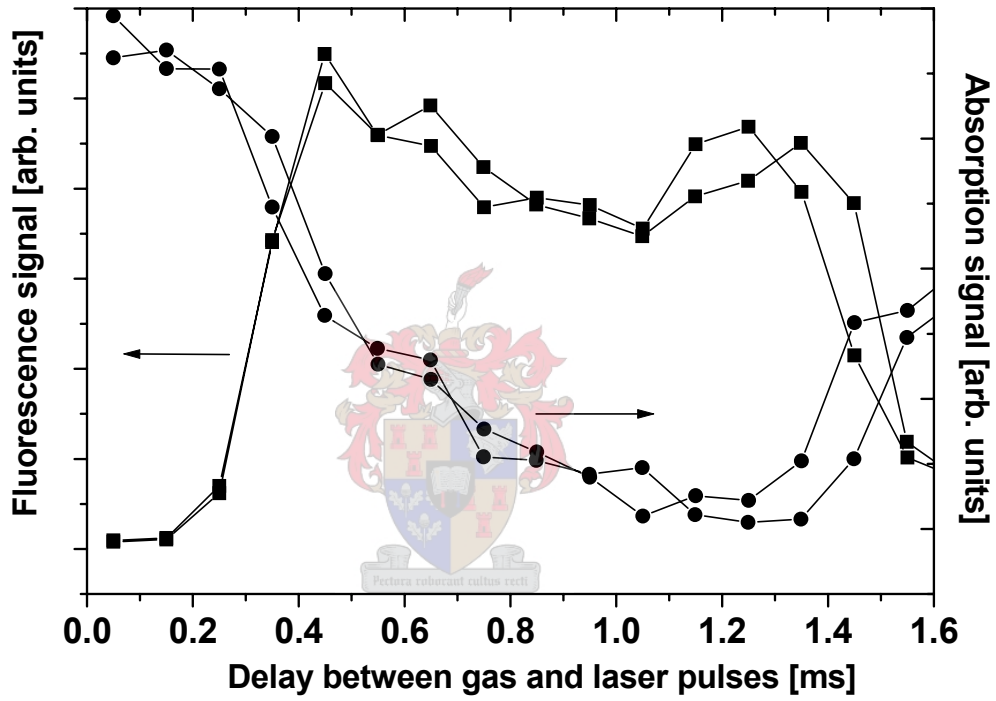

Figure 5-5: Example of a LIF (■) and absorption (•) delay scans of the R(2) line of $A^1\Pi(v' = 2)-X^1\Sigma^+(v'' = 0)$, indicating a typical $^{12}C^{16}O$ delay scan structure.

[2] These delay scans were recorded twice consecutively, and both results are included in the figure by superposition.

5.2.4 Spectral line caused by perturbation

A spectral line was observed repeatably in LIF and absorption spectra in the $A^1\Pi(v' = 2)-X^1\Sigma^+(v'' = 0)$ band at 147.8044 nm, a wavelength where no rovibronic line of CO is expected from the theoretically calculated band structure. This region contains only lines of $^{12}C^{16}O$, and the lines of this isotopomer in the vicinity are all accounted for. This additional line has been identified as an additional Q(8) line of $^{12}C^{16}O$ caused by a perturbation between the $A^1\Pi(v' = 2)$ state and the $I^1\Sigma^-(v = 3)$ state [14]. Figure 5-6 shows the (a) absorption and (b) LIF spectra of this spectral region. The labels of the $^{12}C^{16}O$ lines are indicated with solid lines and the $^{13}C^{16}O$ lines with dotted lines. The additional line is indicated with a dashed line and labelled Q(8)*. This line has the same linewidth as other lines in the vicinity. The delay scan structure is shown in Figure 5-7, in comparison to the delay scans of the nearby P(4) and Q(7) lines of $^{12}C^{16}O$. The delay scan exhibits the same *dip* structure, and not the triangular structure typical of rare isotopomer lines.

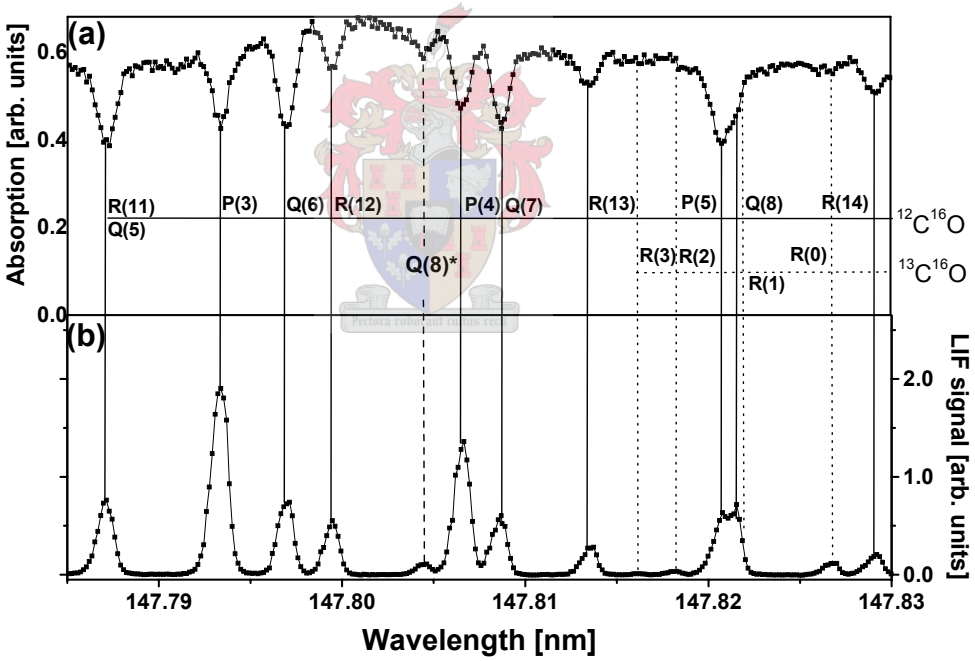

Figure 5-6: A section of the $A^1\Pi(v' = 2)-X^1\Sigma^+(v'' = 0)$ band, indicating an additional Q(8) line (Q(8)*) caused by perturbation, visible in the (a) absorption and (b) LIF spectra.

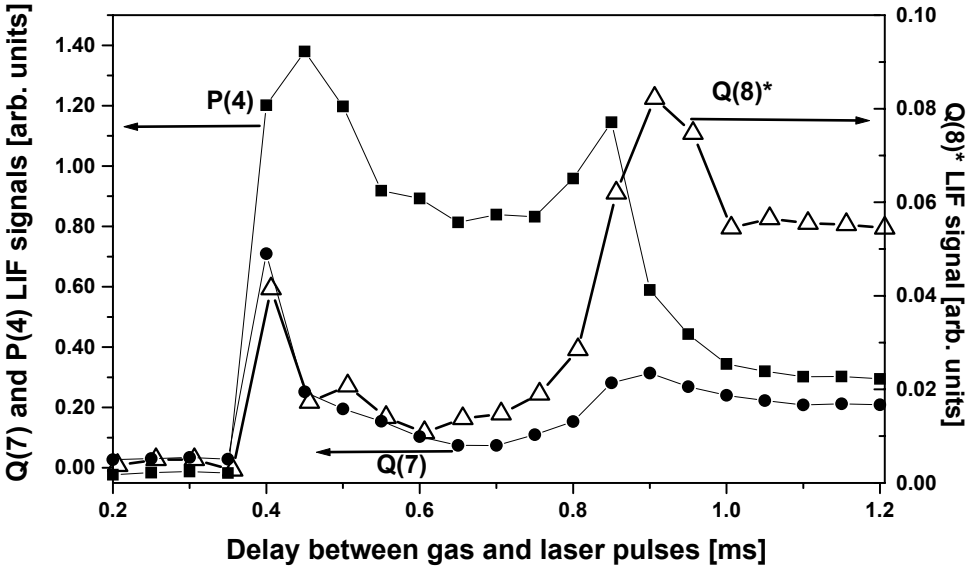

Figure 5-7: Delay scans (LIF) of the P(4) (■) and Q(7) (•) lines of the $A^1\Pi(v' = 2)$–$X^1\Sigma^+(v'' = 0)$ band and the additional Q(8) line (△) caused by perturbation.

5.3 Optimisation of experimental conditions

5.3.1 Sample density

An increase in the amount of CO in the sample gas mixture (i.e. an increase in sample density) was found to significantly increase the signal-to-noise ratio of the measured spectra. This effect is illustrated in Figure 5-8 for two experimental spectra of the $A^1\Pi(v' = 2)$–$X^1\Sigma^+(v'' = 0)$ band, recorded using 25% and 100% CO in 4 bar total stagnation pressure. Clearly visible in this figure is the increased signal-to-noise ratio of the $^{13}C^{16}O$ lines in the spectrum recorded with higher sample density, even though the $^{12}C^{16}O$ lines show relatively small increases in their peak intensities. These spectra were recorded on different days but all other conditions were identical as far as possible.[3] Figure 5-9 shows the signal increase for selected lines of $^{12}C^{16}O$ in the above-mentioned spectra. The signal increase with density increase is generally smaller (and even negative in some cases) for the lowest-J lines of the Q and R branches, relative to the

[3] This indicates possible changes in the heatpipe operating conditions and laser pulse energies, but the spectra can safely be compared on a relative scale.

higher-J lines of all branches, which have large increases in signals. A general trend of a larger signal increase with higher J-value in a given branch cannot unambiguously be distinguished from this data, since some of the lines show smaller increases, for example the R(8) line signal increase is smaller than that of R(7).

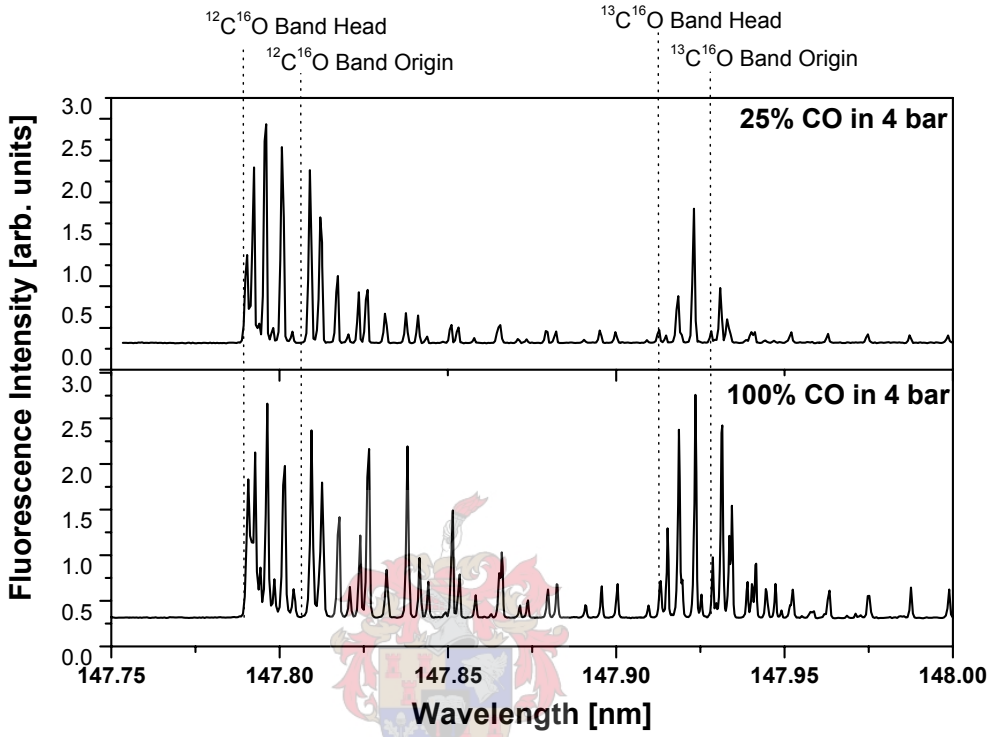

Figure 5-8: Experimental spectra of the $A^1\Pi(v' = 2)$–$X^1\Sigma^+(v'' = 0)$ band recorded using different CO gas mixtures: (a) 25% CO in argon and (b) 100% CO, both at 4 bar stagnation pressure. This gives a qualitative indication of the increase in sensitivity of the spectra with an increased CO density.

This effect was investigated in more detail by recording spectra at different sample gas mixtures. In this experiment the sample gas mixture was changed systematically from 0.6% to 12% to 24% in a total of 4 bar stagnation pressure, using argon as carrier gas. Figure 5-10 (a) shows the lowest-J lines of $^{12}C^{16}O$, and Figure 5-10 (b) shows the lowest-J lines of $^{12}C^{17}O$, which are being overlapped by the higher-J lines of $^{12}C^{16}O$. Only one of the $^{12}C^{17}O$ lines is clearly visible without any overlap by other lines - this is the R(0) line, and is indicated in the figure by an asterisk. From this figure it can be seen that all lines exhibit an increase in

signal strength with increasing CO density, irrespective of isotopic species or quantum number J. The relative signal increase as a function of initial signal strength for these lines is shown in Figure 5-11 (a). This shows a clear trend, namely that the lines having lowest initial intensity exhibit a larger relative increase with density increase, while the lines having an initial large signal show a relatively small signal increase. Figure 5-11 (b) shows the same signal increases, plotted as a function of J-value. This indicates a rough dependance of the signal increase on increasing J-value in a branch, although there is much variation.

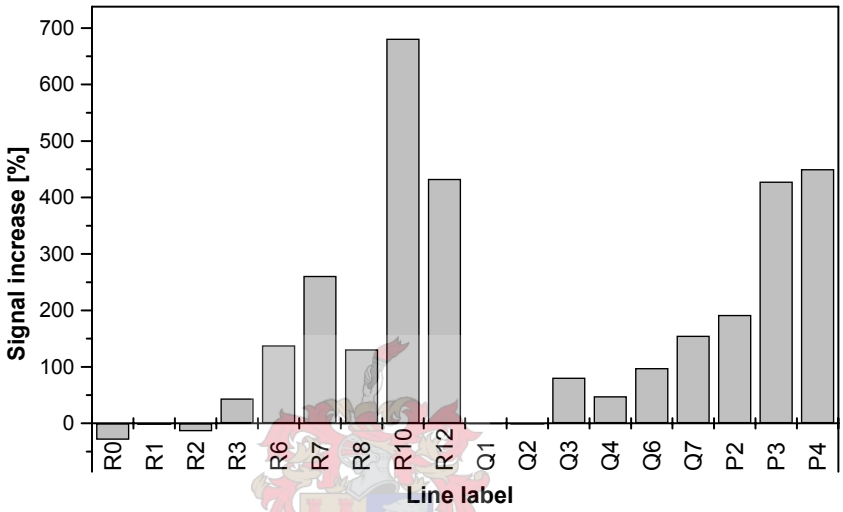

Figure 5-9: Signal increase (expressed as a percentage) of selected lines of $^{12}C^{16}O$ when CO density is increased from 25% to 100%. Lines are arranged according to the J-value in each branch, and only lines which are clearly identified in the spectra have been included.

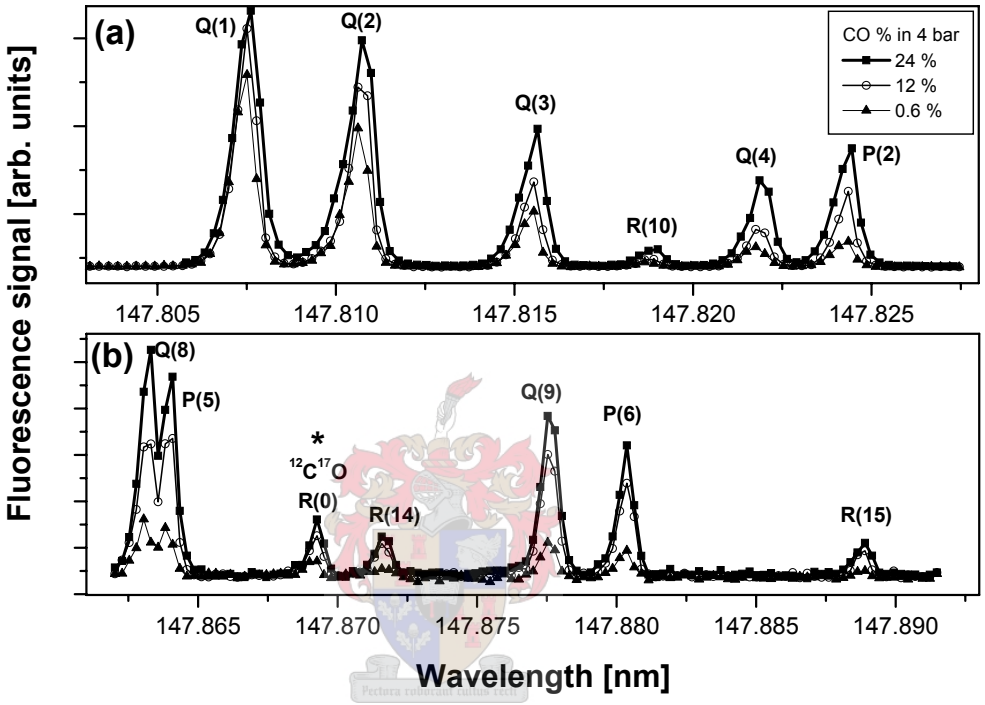

Figure 5-10: Experimental spectra of the $A^1\Pi(v' = 2)-X^1\Sigma^+(v'' = 0)$ band showing (a) lower-J lines of $^{12}C^{16}O$, and (b) one $^{12}C^{17}O$ line - R(0)* among higher-J lines of $^{12}C^{16}O$. Spectra recorded using different CO densities: 0.6%, 12%, 24%.

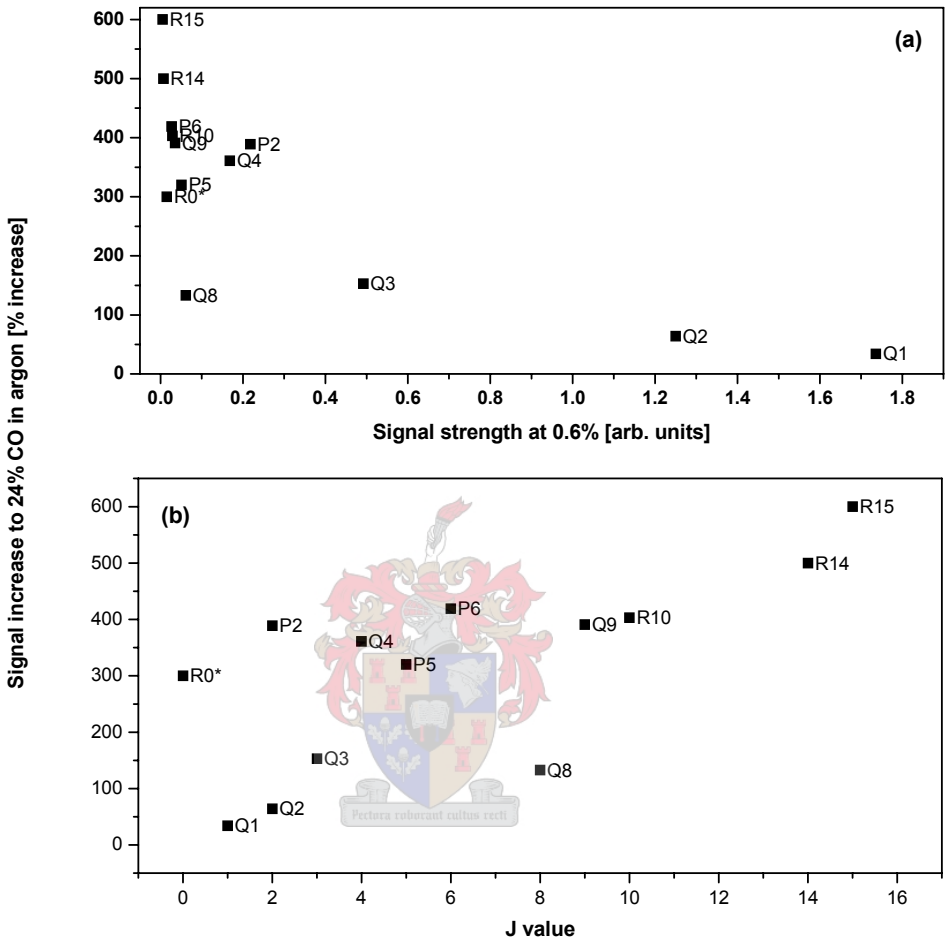

Figure 5-11: Signal increase of selected lines when CO density is increased from 0.6% to 24%, expressed as a percentage of the signal strength at 0.6% CO graphed relative to (a) initial signal strength and (b) J-value of each line.

5.3.2 Delay setting

In the present study, the delay scans of the rarer CO isotopomer lines were recorded for the first time. Figure 5-12 (a) shows the delay scans of the R(0) lines of the four isotopomers $^{12}C^{16}O$, $^{13}C^{16}O$, $^{12}C^{18}O$ and $^{12}C^{17}O$ in the $A^1\Pi(v'=2)-X^1\Sigma^+(v''=0)$ band, using a pulse duration[4] of 0.5 ms. The signal of the $^{12}C^{17}O$ fluorescence is too small to observe on this scale and the same results are therefore presented on an adjusted scale in Figure 5-12 (b). Delay scans of the rarer isotopomers exhibit a triangular delay scan profile, differing from the plateau profile of $^{12}C^{16}O$. It is clear from this example that the peak fluorescence signal is found at a different delay time for the rarer isotopomers than for $^{12}C^{16}O$. This is of particular importance in the present study, since the delay setting has previously been set to the initial peak of the $^{12}C^{16}O$ delay scan, always around 0.4 ms. In the present study the delay scan setting has been changed to around $0.55 - 0.65$ ms to optimise the detection of the rarer isotopomers.

5.3.3 Gas pulse duration

Previously, pulse durations were restricted to the shortest pulses obtainable with the previous pulse driver: roughly 1.3 ms. With the introduction of the new pulsed valve driver to the experimental setup (see Section 4.3.2), pulse durations down to 0.3 ms have been obtained. Measurements of the delay scans for different pulse duration settings are shown in Figure 5-13 (a) for the R(0) line of the $A^1\Pi(v'=3)-X^1\Sigma^+(v''=0)$ band of $^{12}C^{16}O$ and in Figure 5-13 (b) for the R(0) line of the $A^1\Pi(v'=2)-X^1\Sigma^+(v''=0)$ band of $^{12}C^{17}O$. This pulse duration setting of the pulsed valve driver is not an absolute indication of the physical pulse duration and a 200 μs setting corresponds to a physical duration of 300 μs, for example. The pulse duration does not necessarily scale linearly with this setting due to the properties of the solenoid valve. In the case of $^{12}C^{16}O$ the peak intensity is not strongly influenced by the pulse duration due to the plateau profile. In the case of $^{12}C^{17}O$ the peak intensity is strongly dependent on pulse duration for pulses up to a pulse duration setting of 0.65 ms, in contrast to the case of $^{12}C^{16}O$. Similar to the results of the previous section, the delay scan structure is triangular in shape and has a peak value later than the peak of the $^{12}C^{16}O$ delay scans, specifically 0.13 ms later. In

[4] This is estimated roughly from the delay scan itself. The pulse duration setting on the pulsed valve driver was 250 μs.

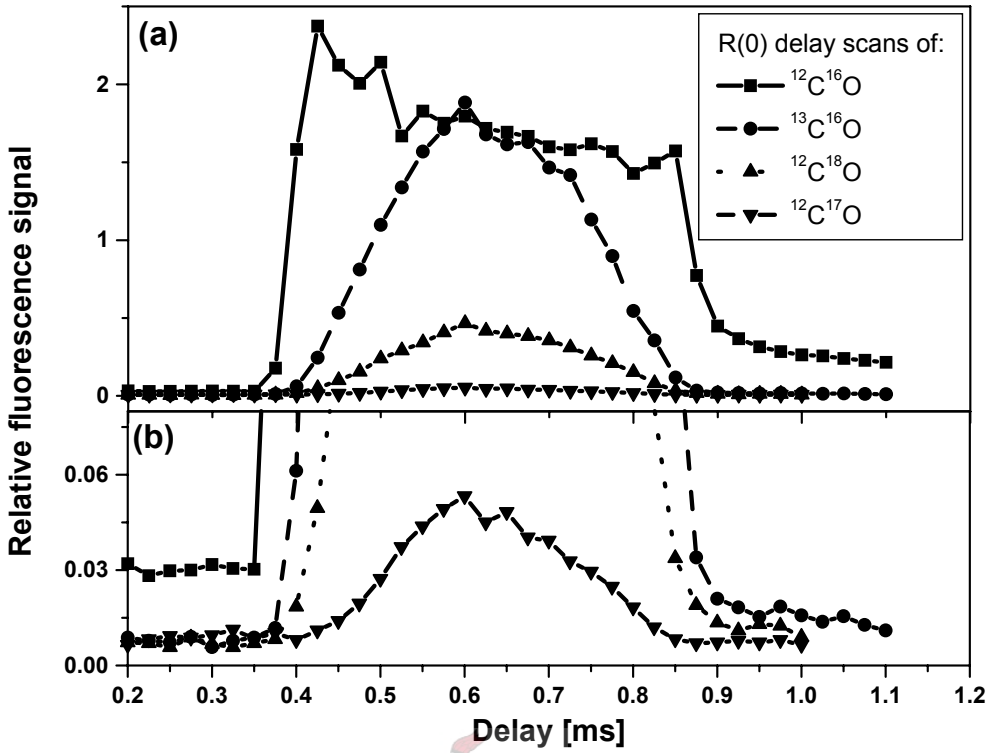

Figure 5-12: Experimental delay scans of the R(0) lines of the $A^1\Pi(v' = 2)$–$X^1\Sigma^+(v'' = 0)$ bands of the $^{12}C^{16}O$, $^{13}C^{16}O$, $^{12}C^{18}O$ and $^{12}C^{17}O$ isotopomers of CO on (a) the same relative intensity scale, and (b) a more sensitive scale, to indicate the shape of the $^{12}C^{17}O$ delay scan. Pulse duration setting in this experiment was 0.25 ms.

the present study the pulse duration setting has been set to 0.65 ms to optimise the detection of the rarer isotopomers.

The delay scan profiles of $^{12}C^{17}O$ with longer pulses tend toward a plateau profile (or dip profile), but the relative initial peak difference remains. This may be explained by an increase in the $^{12}C^{17}O$ density with larger pulse durations, as more gas expands into the vacuum and the interaction volume.

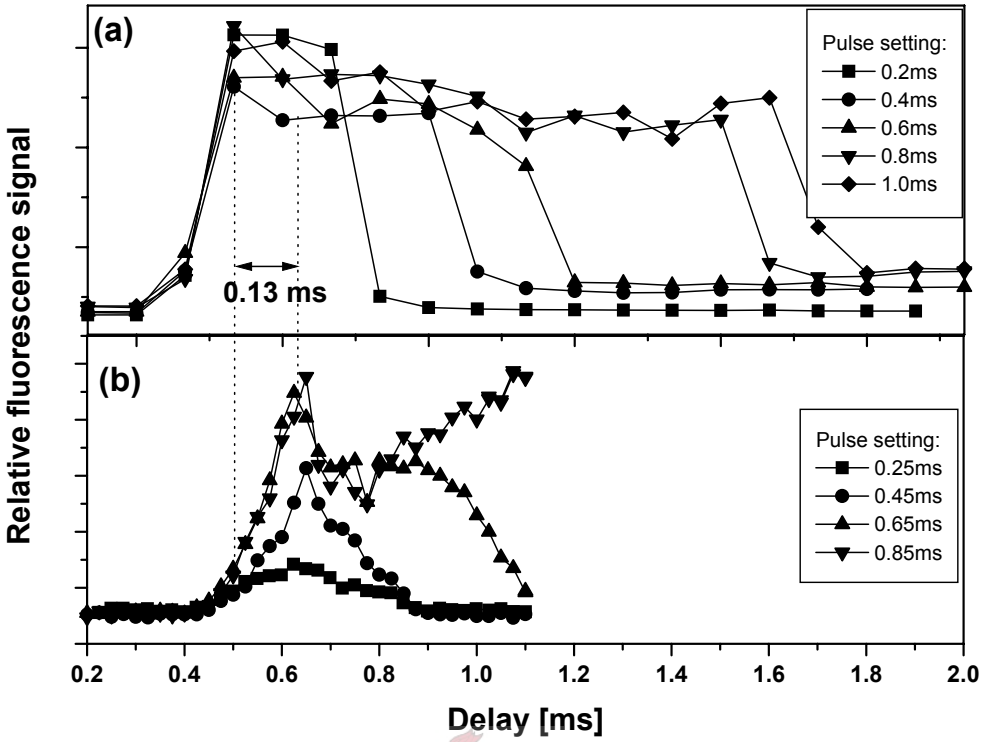

Figure 5-13: Delay scans of $^{12}C^{16}O$ and $^{12}C^{17}O$ in comparison, using different pulse duration settings. Shown here are delay scans of (a) the R(0) line of the $^{12}C^{16}O$ $A^1\Pi(v' = 3)$–$X^1\Sigma^+(v'' = 0)$ band and (b) the R(0) line of the $^{12}C^{17}O$ $A^1\Pi(v' = 2)$–$X^1\Sigma^+(v'' = 0)$ band.

5.3.4 Laser energy and alignment

The total useful VUV laser energy (the SF component) and its alignment through the gas pulse may both have an effect on the LIF spectral characteristics. Although a detailed investigation of the influence of these factors was not attempted in this study, two spectra are presented which indicate strong influences of either or both of these factors.

The two spectra of the vibronic bands having $v' = 3, 2, 1$ and 0 were recorded on different occasions. The difference between the two spectra is illustrated in Figure 5-14 for the band head region of the $A^1\Pi(v' = 2)$–$X^1\Sigma^+(v'' = 0)$ band, indicating a *cold* spectrum in the upper half and a *hot* spectrum in the lower half. The *cold* spectrum has fewer lines in comparison to the *hot* spectrum which has many lines of higher-J values. The reason for the labels *hot* and *cold* is the prominence of the higher-J lines in the *hot* spectrum, following from the explanation

in Section 3.3. The spectral lines in the *hot* spectrum are also slightly broadened in comparison to the *cold* spectrum, but this does not affect the identification or assignment of spectral lines.

A direct comparison of the experimental conditions of the two situations for recording the $A^1\Pi(v' = 2)-X^1\Sigma^+(v'' = 0)$ band showed that the resonant laser had more pulse energy in the *hot* spectrum (1.5 mJ compared to 1 mJ) and the non-resonant laser had roughly the same pulse energy in both cases. There are indications that the intensity of the SF radiation in the *hot* situation was higher than in the *cold* situation. These indications are from the relative signal strengths in the LIF spectra, for example the R(0) line which has a roughly 3 times higher intensity in the *hot* situation. The signals from the absorption spectra cannot be used to derive relative VUV energies since the settings of the boxcar integrators were different. The only other significant difference in the experimental conditions was the pulse duration setting of 250 μs in the *hot* spectrum and 650 μs in the *cold* spectrum. However, there are indications that the *hot* spectrum was recorded with the laser beams intersecting the gas jet *off-centre*. These conditions are used to propose an explanation for the observed differences in the next chapter.

5.4 Spectra of rare isotopomers

5.4.1 Overview of measured spectra

Each of the recorded high-resolution simultaneous LIF and absorption spectra of the CO $A^1\Pi(v' = 0-5)-X^1\Sigma^+(v'' = 0)$ bands includes lines of four isotopomers of CO, namely $^{12}C^{16}O$, $^{13}C^{16}O$, $^{12}C^{18}O$ and $^{12}C^{17}O$. Experimental LIF spectra of all six vibronic bands investigated are shown together in Figure 5-15. The labels A, B, C and D roughly indicate the positions of the band origins of each of the above-mentioned isotopomers in each vibronic band, in the same order of natural abundance: $^{12}C^{16}O$, $^{13}C^{16}O$, $^{12}C^{18}O$ and $^{12}C^{17}O$ respectively.

As a demonstration of the signal-to-noise ratios achieved for the isotopomer lines of interest, the region of $^{12}C^{17}O$ lines in the $A^1\Pi(v' = 2)-X^1\Sigma^+(v'' = 0)$ band is presented in Figure 5-16. This is a small section (approximately $\frac{2}{5}$) of the entire wavelength scan of this band. The lines of $^{12}C^{17}O$ are clearly identified in between higher-J lines of $^{12}C^{16}O$, which have a smaller relative intensity than their corresponding lower-J lines of $^{12}C^{16}O$ (toward shorter wavelengths). The

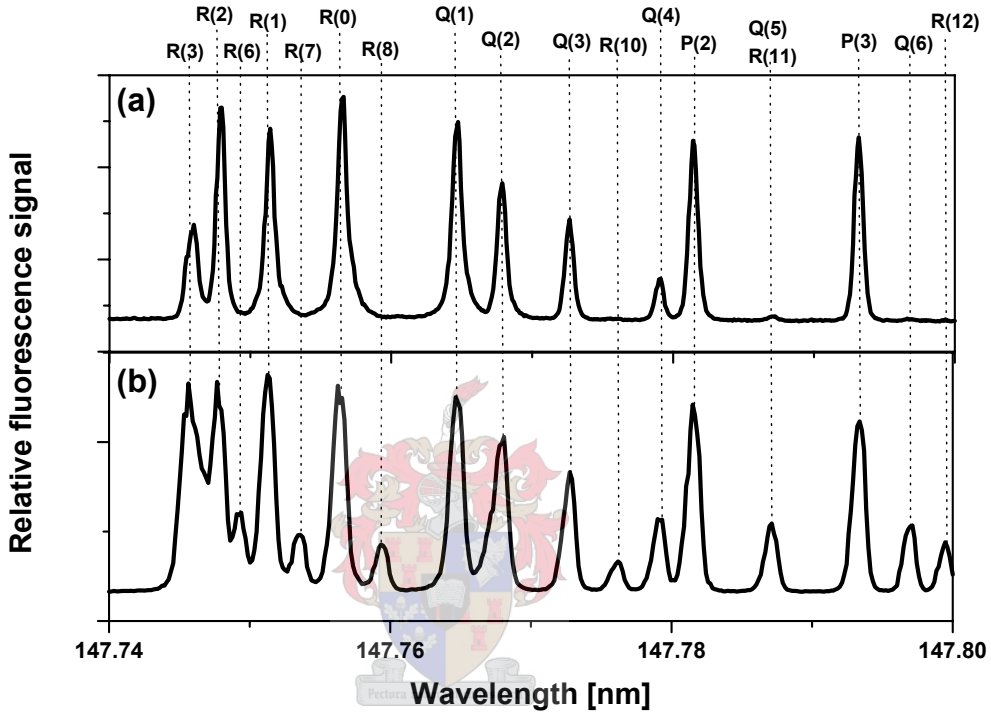

Figure 5-14: Experimental spectra of the $A^1\Pi(v' = 2)-X^1\Sigma^+(v'' = 0)$ band. The upper spectrum (a) corresponds to the *cold* conditions, while the lower (b) corresponds to the *hot* conditions.

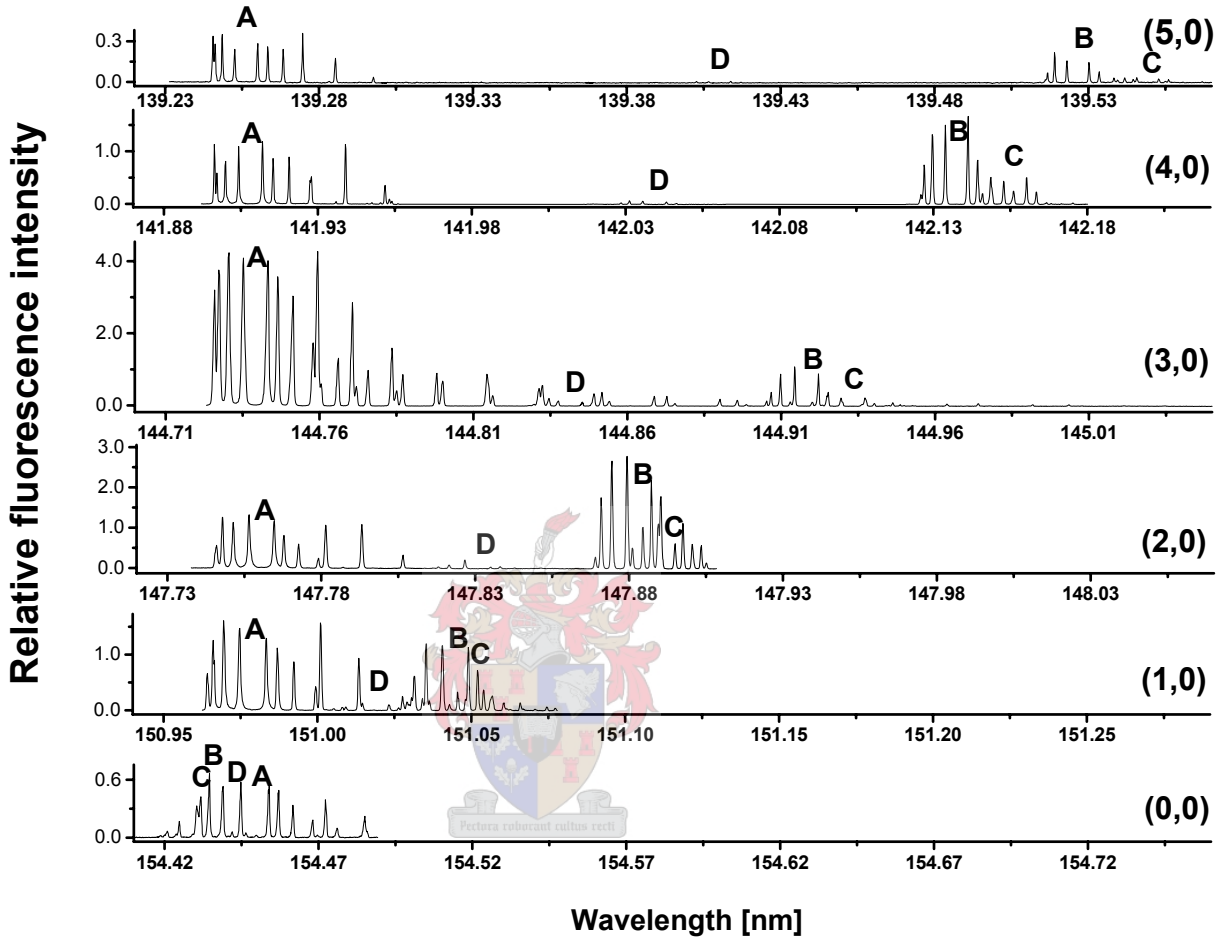

Figure 5-15: Experimental LIF rovibronic spectra of all six bands of interest: $A^1\Pi(v' = 0 - 5) - X^1\Sigma^+(v'' = 0)$. The wavelength axes have been scaled to show the wider spacing of lines in higher vibrational states. The fluorescence intensity (y-axis) has been scaled roughly to allow comparison of intensities between different bands.

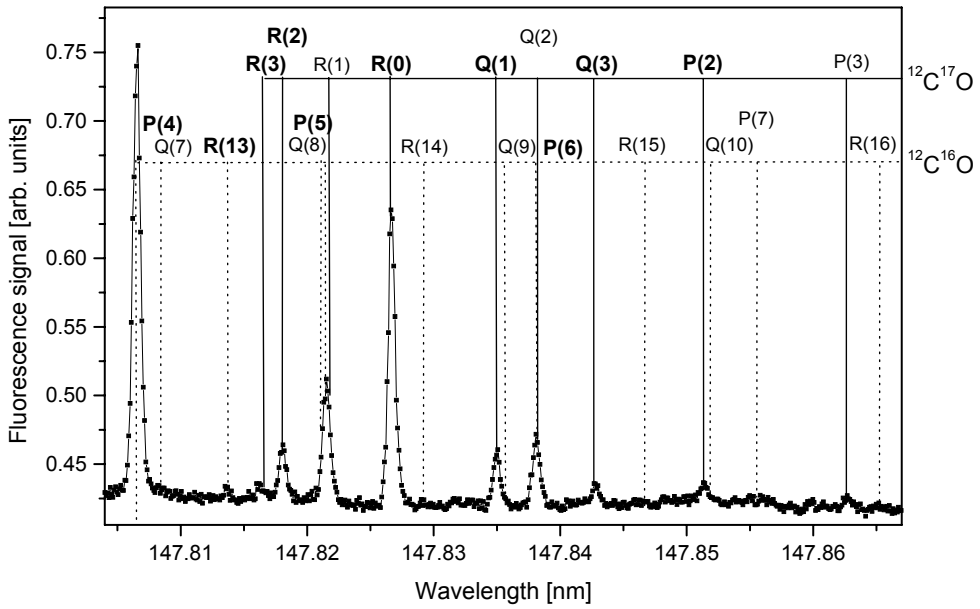

Figure 5-16: Experimental LIF spectrum of a small section of the $A^1\Pi(v' = 2)-X^1\Sigma^+(v'' = 0)$ band, demonstrating the signals achieved for $^{12}C^{17}O$ lines (solid lines) amongst higher-J lines of $^{12}C^{16}O$ (dotted lines).

intensity axis has been adjusted to a more sensitive scale than Figure 5-15.

A short description of the spectral structure is warranted here, as this is applicable to line identification, for the measured spectra in the bands with $v' = 1 - 5$. The structure of the band with $v' = 0$ is slightly different due to the near-zero vibrational isotopic shift, but the same principles apply. From the short wavelength side (refer to Figure 5-15), the first lines encountered are in the form of the band head of $^{12}C^{16}O$ (A), followed by the band head of $^{12}C^{17}O$ (D), followed by the closely spaced band heads of $^{13}C^{16}O$ (B) and $^{12}C^{18}O$ (C). These spacings between band heads of the different isotopomers decrease with decreasing vibrational number. Due to the above-mentioned structure, the possibility of overlapping of lines increases with wavelength within a given band, and increases with decreasing vibrational number in different bands.

Vibrational shifts of the band origins of the less abundant isotopomers relative to the band origin of $^{12}C^{16}O$ were determined from calculations using experimental results. The summary

of the calculated vibrational shifts is presented in Table 5.2. The calculation of the band origins are discussed in more detail in Appendix 8.2.

Table 5.2: Calculated theoretical and observed experimental vibrational isotopic shifts of the band origins. The theoretical band origin values were calculated using constants given in Herzberg (1950) [51].

	Vibrational isotopic shift relative to $^{12}C^{16}O$ [cm^{-1}]					
Band label	**$^{13}C^{16}O$**		**$^{12}C^{18}O$**		**$^{12}C^{17}O$**	
	Theory	Experiment	Theory	Experiment	Theory	Experiment
$(5,0)$	138.5	139.1	150.2	150.7	79.0	79.3
$(4,0)$	112.3	113.7	121.8	123.0	64.1	65.0
$(3,0)$	84.7	85.3	91.9	92.6	48.3	48.7
$(2,0)$	55.5	56.2	60.2	60.8	31.7	32.1
$(1,0)$	24.9	28.9	27.0	31.0	14.2	17.5
$(0,0)$	-7.3	-6.2	-7.9	-6.7	-4.2	-3.6

Individual LIF and absorption spectra of all six vibronic bands are included separately in Appendix 8.1, in more detail. The exact positions of the $^{12}C^{16}O$ and $^{13}C^{16}O$ lines, which are used for calibration of the spectra, are indicated in these individual spectra, as well as detailed descriptions of the corresponding experimental conditions.

5.4.2 Line identification

It is essential that the lines of $^{12}C^{16}O$ and $^{13}C^{16}O$ which are used as wavelength references are identified correctly, in order to obtain an accurately calibrated spectrum. Furthermore, the accurate identification of $^{12}C^{17}O$ and $^{12}C^{18}O$ lines (and finding their exact positions) from a calibrated spectrum is also of the utmost importance.

The expected wavelengths of the rovibronic lines of the four isotopomers observed are required for accurate identification. These wavelengths are obtained either directly from literature or by calculation (see Section 3.2.2). After the expected wavelengths have been determined by either of these methods, the following line identification procedure is applied.

The line identification procedure entails the use of the expected wavelengths (or spectral *fingerprint*) to determine the isotopomer, the branch (P, Q or R) and the J quantum number associated with each detected line. This process is made challenging by overlap of the lines, either with other lines of the same isotopomer, or with those of the other isotopomers. Overlap

of lines of the same isotopomer is caused by the nature of the branches in the rovibronic structure. Overlap of lines of different isotopomers is caused by the relatively small vibrational shifts of the band origins of the different isotopomers in a given band.

A number of principles were applied to resolve and identify some of the overlapping lines. As described in Section 3.3, the supersonic expansion causes cooling of the sample gas. At the prevailing temperature in the supersonic expansion, the line intensity decreases monotonically with increasing J-value in all branches. When two lines overlap, the preceding lines in the same branches are inspected (for example if the lines P(4) and Q(7) are overlapping, P(3) and Q(6) are inspected). If one of the preceding lines has a relatively low intensity and the other a relatively high intensity, it may be assumed that the branch belonging to the line with the higher intensity will also prevail in the overlapping line and this line may be accurately identified. However, if the lines are similar in intensity (either low or high), they may not be resolved.

Additionally, a series of lines of a particular branch may be inspected. The relative intensity of the series is expected to decrease without sudden increases or discontinuities (in a roughly exponential decrease). Any deviation from this behaviour indicates the presence of another line contributing to the additional intensity.

The process of finding the peak of a spectral line, and therefore the most accurate wavelength determination, is by visual inspection using Origin 5.0 software. The results in a graphical format are inspected, *zoomed in* on a particular line and the peak position found by interpolation of the data points. This was done manually, since the peak-finding algorithm of Origin was found to be less accurate in determining the exact peak position.

Most spectra were recorded using wavelength step sizes of approximately $0.1 - 0.2$ pm in the VUV[5], and most spectral lines were observed to have a linewidth of $0.4 - 0.8$ pm (FWHM). Typical spectral lines therefore consist of a minimum of about $5 - 10$ data points, sufficient to determine line peaks to an accuracy of 0.2 pm, as shown in Section 5.2.2.

[5] Most experimental spectra were recorded using 1.5 pm step sizes in visible dye laser wavelength. The translated VUV step sizes are wavelength dependent and range between the extremes of 0.1 pm in the (0,0) band and 0.2 pm in the (5,0) band.

5.4.3 Summary of results on $^{12}C^{17}O$ and $^{12}C^{18}O$

A total of 29 new lines of $^{12}C^{17}O$ were experimentally detected in the $A^1\Pi(v')-X^1\Sigma^+(v''=0)$ bands having $v' = 0-5$, and accurate wavelengths were determined for these lines. In the identification of these lines, the possibility of overlap by $^{12}C^{16}O$ lines must be taken into consideration. The detailed spectra and discussion of line identification of all $^{12}C^{17}O$ lines are included in Appendix 8.1. A total of 35 lines of $^{12}C^{17}O$ are included here, since this includes the 6 lines previously published.

In total, 44 new lines of $^{12}C^{18}O$ were experimentally detected in the $A^1\Pi(v')-X^1\Sigma^+(v''=0)$ bands having $v' = 0-5$, and accurate wavelengths were similarly determined for these lines, although their wavelengths are known in the literature. In the identification of these lines, the possibility of overlap by $^{12}C^{16}O$,$^{13}C^{16}O$ and $^{12}C^{17}O$ lines must be taken into consideration. The detailed analyses of the $^{12}C^{18}O$ spectra are omitted from this dissertation and only results are presented. A total of 48 lines of $^{12}C^{17}O$ are included here, since this includes the 4 lines previously published.

Summarised results, after appropriate averaging, are presented here in Tables 5.3–5.8. All these results have an estimated error margin of ± 0.2 pm, as derived from the calibration accuracy test described in Section 5.2.2. Detailed tables of all experimentally determined lines of $^{12}C^{18}O$ and $^{12}C^{17}O$ (in each systematic measurement) are included in Appendix 8.3.

Table 5.3:
Experimentally measured wavelengths for the $A^1\Pi(v'=5)-X^1\Sigma^+(v''=0)$ bands of $^{12}C^{18}O$ and $^{12}C^{17}O$.

	Wavelengths [nm]	
Line label	**$^{12}C^{18}O$**	**$^{12}C^{17}O$**
R(2)	139.5395	
R(1)	139.5418	139.4027
R(0)	139.5457	139.4066
Q(1)	139.5528	139.4138
Q(2)	139.5560	139.4171
Q(3)	139.5608	
P(2)	139.5670	
P(3)	139.5770	

Table 5.4:
Experimentally measured wavelengths for the $A^1\Pi(v' = 4)-X^1\Sigma^+(v'' = 0)$ bands of $^{12}C^{18}O$ and $^{12}C^{17}O$.

	Wavelengths [nm]	
Line label	**$^{12}C^{18}O$**	**$^{12}C^{17}O$**
R(3)		142.0274
R(2)	142.1460	142.0285
R(1)	142.1486	142.0312
R(0)	142.1529	142.0356
Q(1)	142.1603	142.0433
Q(2)	142.1635	142.0465
Q(3)	142.1683	142.0514
P(2)	142.1753	

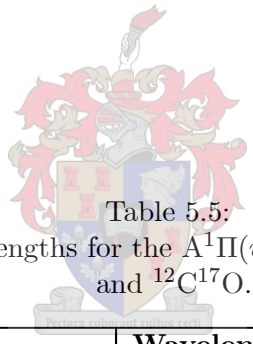

Table 5.5:
Experimentally measured wavelengths for the $A^1\Pi(v' = 3)-X^1\Sigma^+(v'' = 0)$ bands of $^{12}C^{18}O$ and $^{12}C^{17}O$.

	Wavelengths [nm]	
Line label	**$^{12}C^{18}O$**	**$^{12}C^{17}O$**
R(3)	144.9204	144.8282
R(2)		144.8298
R(1)	144.9250	144.8328
R(0)	144.9296	144.8376
Q(1)	144.9375	144.8454
Q(2)	144.9405	144.8486
Q(3)	144.9450	144.8532
Q(4)	144.9514	144.8597
P(2)	144.9527	144.8610

Table 5.6:
Experimentally measured wavelengths for the $A^1\Pi(v' = 2)-X^1\Sigma^+(v'' = 0)$ bands of $^{12}C^{18}O$ and $^{12}C^{17}O$.

	Wavelengths [nm]	
Line label	**$^{12}C^{18}O$**	**$^{12}C^{17}O$**
R(3)		147.8162
R(2)	147.8811	147.8181
R(1)	147.8845	
R(0)	147.8895	147.8268
Q(1)	147.8975	147.8350
Q(2)	147.9005	
Q(3)	147.9051	147.8429
Q(4)	147.9111	147.8490
P(2)	147.9136	147.8514
P(3)	147.9248	147.8628
P(4)	147.9375	
P(5)	147.9515	

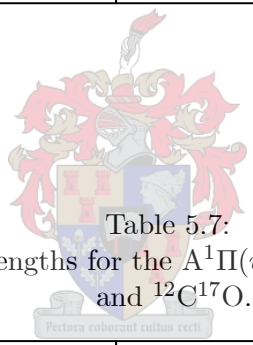

Table 5.7:
Experimentally measured wavelengths for the $A^1\Pi(v' = 1)-X^1\Sigma^+(v'' = 0)$ bands of $^{12}C^{18}O$ and $^{12}C^{17}O$.

	Wavelengths [nm]	
Line label	**$^{12}C^{18}O$**	**$^{12}C^{17}O$**
R(3)	151.0341	151.0030
R(2)	151.0365	151.0052
R(1)		151.0092
R(0)	151.0457	151.0146
Q(1)	151.0540	151.0232
Q(2)	151.0570	151.0263
Q(3)	151.0616	
Q(4)	151.0670	
Q(5)	151.0745	
P(2)	151.0708	

Table 5.8:
Experimentally measured wavelengths for the $A^1\Pi(v'=0)-X^1\Sigma^+(v''=0)$ bands of $^{12}C^{18}O$ and $^{12}C^{17}O$.

	Wavelengths [nm]	
Line label	**$^{12}C^{18}O$**	**$^{12}C^{17}O$**
R(2)	154.4200	
R(1)	154.4237	
R(0)	154.4292	154.4363
Q(2)	154.4407	
Q(4)	154.4517	

5.5 Spectra of singlet-triplet transitions

5.5.1 Overview of measured singlet-triplet lines

Singlet-triplet lines here refer to rovibronic excitations from the singlet electronic ground state to electronically excited triplet states. In this work, 32 singlet-triplet lines belonging to three different singlet-triplet bands of $^{12}C^{16}O$ were detected. Figure 5-17 is a modified reproduction of the previous Figure 5-15, shifted to indicate the relative positions of the singlet-triplet bands detected. Lines of the $a'^3\Sigma^+(v'=14)-X^1\Sigma^+(v''=0)$ band were detected in the region of the $A^1\Pi(v'=4)-X^1\Sigma^+(v''=0)$ lines, between the $^{12}C^{16}O$ and $^{12}C^{17}O$ lines. Lines of the $d^3\Delta(v'=5)-X^1\Sigma^+(v''=0)$ band were detected in the region of the $A^1\Pi(v'=1)-X^1\Sigma^+(v''=0)$ lines, between the $^{13}C^{16}O$ lines (and also overlapping with other isotopomer lines). Lines of the $e^3\Sigma^-(v'=1)-X^1\Sigma^+(v''=0)$ band were found on the short-wavelength side of the band head of $A^1\Pi(v'=0)-X^1\Sigma^+(v''=0)$ and were not overlapping with any isotopomer lines.

5.5.2 Detection of singlet-triplet lines

Figure 5-18 shows individual time-resolved fluorescence signals after excitation of a line of the $A^1\Pi(v'=4)-X^1\Sigma^+(v''=0)$ band and a line of the $a'^3\Sigma^+(v'=14)-X^1\Sigma^+(v''=0)$ band, both measured with the photomultiplier tube and observed on a 500-MHz oscilloscope. The indicated fluorescence lifetime of the $A^1\Pi$ state is observed to be of the order of 20 ns, but this is exaggerated due to the pulse duration of the laser which is 20 ns. The $A^1\Pi$ state has a lifetime of about 10 ns, as has been determined in numerous studies, see for example Strobl and

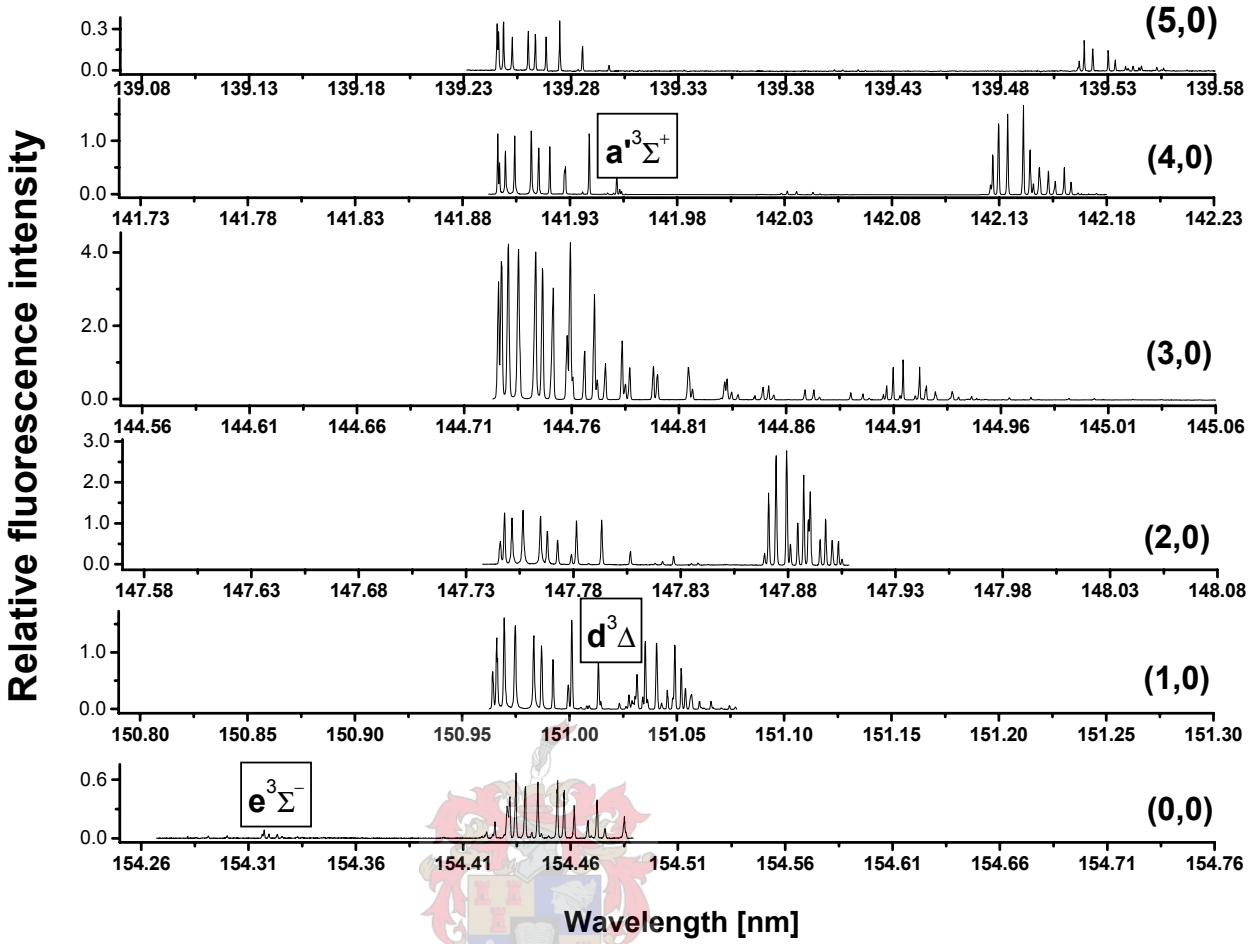

Figure 5-17: Overview of experimental band spectra, indicating the positions of the three observed singlet-triplet bands.

Vidal (1987) [28]. The indicated fluorescence lifetime of the investigated $a'^3\Sigma^+$ state is longer, indicating its triplet character. The singlet-triplet transitions of $a'^3\Sigma^+(v' = 14)-X^1\Sigma^+(v'' = 0)$ have lifetimes of around 4.5 μs [28]. The observed lifetime is only about 0.2 μs, which is probably due to a significant mixing of the triplet and singlet states.

By setting the boxcar integrator gate to integrate over the temporal region from approximately $150 - 250$ ns (refer to Figure 5-18), the singlet-triplet lines may be recorded without recording singlet-singlet lines. This is because the singlet-singlet fluorescence signal would have dropped to zero by this time. This was done in the $d^3\Delta(v' = 5)-X^1\Sigma^+(v'' = 0)$ band, and

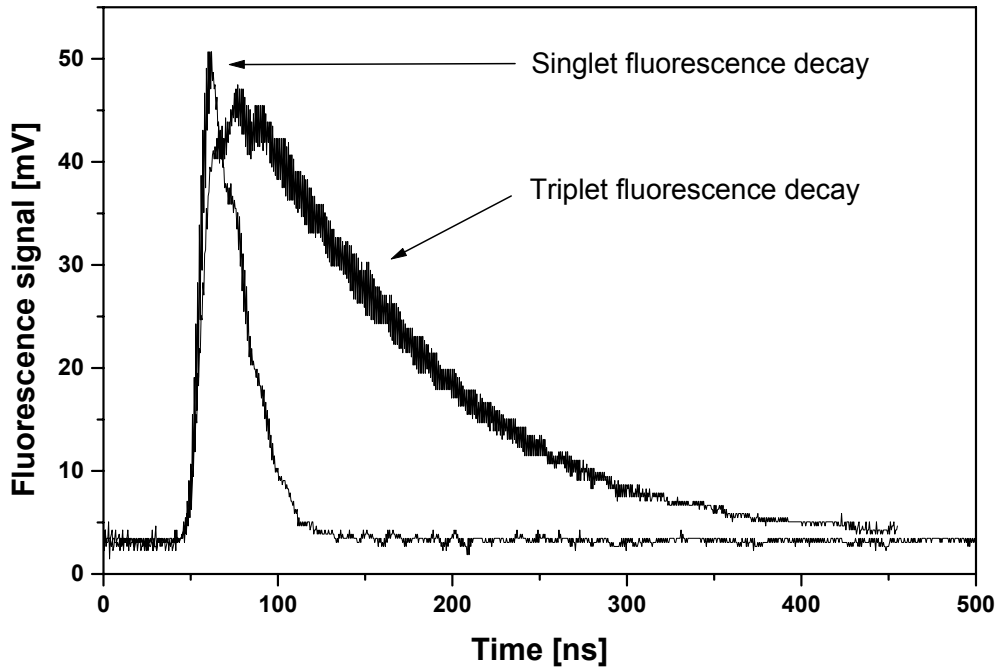

Figure 5-18: Experimental measurement of of the fluorescence decay after rovibronic laser excitation in the $A^1\Pi(v' = 4)-X^1\Sigma^+(v'' = 0)$ band (singlet-singlet line) and the $a'^3\Sigma^+(v' = 14)-X^1\Sigma^+(v'' = 0)$ band (singlet-triplet line).

compared to a spectrum recorded using the usual boxcar gate setting: a narrower gate over the central peak of a typical singlet-singlet fluorescence signal. This comparison is shown in Figure 5-19. The identified singlet-triplet lines are indicated with *dotted* lines. With the narrow gate setting (Figure 5-19(b)) the singlet-triplet lines have low intensity relative to the singlet-singlet lines and much overlap with these singlet-singlet lines occurs. The delayed gate setting enhances the intensity of the singlet-triplet lines whereas the singlet-singlet lines are virtually unobservable. The single *dashed* line indicates the position of a strong singlet-singlet fluorescence signal which is also detected at low intensity in the measurement with the delayed gate setting.

5.5.3 Summary of singlet-triplet line results

The observed lines of the three bands of singlet-triplet lines of $^{12}C^{16}O$ that were detected in this study in the vicinity of the CO Fourth Positive System transitions were correctly identified. The labelling scheme is adopted from Morton and Noreau (1994) [9]. Results are summarised

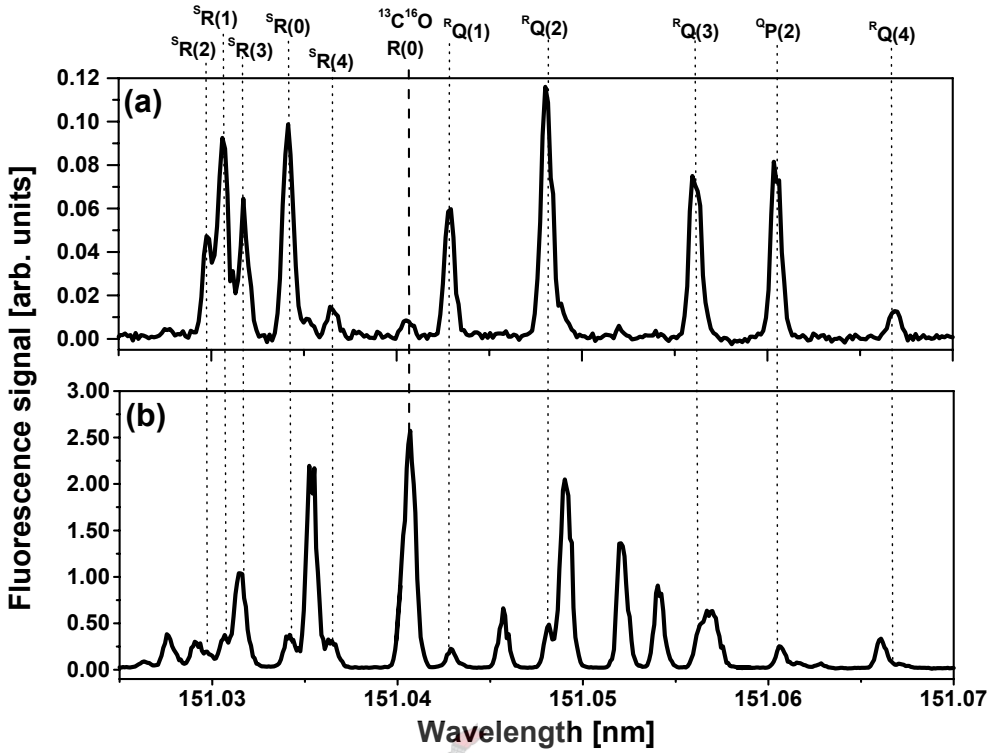

Figure 5-19: Spectra of the same wavelength region recorded (a) using a wider and delayed gate setting for selectively recording the singlet-triplet lines of the $d^3\Delta(v' = 5)$–$X^1\Sigma^+(v'' = 0)$ band, which have a longer fluorescence lifetime, and (b) the usual narrow gate setting for detection of the $A^1\Pi(v' = 1)$–$X^1\Sigma^+(v'' = 0)$ singlet-singlet lines.

in Tables 5.9–5.11. Of the 32 lines detected and included in these tables, 10 are new to the scientific literature and are marked with asterisks. The two lines marked with a # symbol have recently been added to the online database [31]. These tables are included in Appendix 8.3 with an additional insignificant figure, if required in calculations.

Table 5.9:
Experimentally measured wavelengths for the $e^3\Sigma^-(v'=1)-X^1\Sigma^+(v''=0)$ band of $^{12}C^{16}O$.

Line label	**Wavelength [nm]**
${}^{Q}R(0)$	154.3164
${}^{Q}R(1)$	154.3196
${}^{Q}R(2)$	154.3257
${}^{Q}R(3)$	154.3350
${}^{S}R(0)$	154.3000
${}^{S}R(1)$	154.2913
${}^{S}R(2)$	154.2856
${}^{Q}Q(1)$	154.3173
${}^{Q}Q(2)$	154.3234
${}^{Q}Q(3)$	154.3328

Table 5.10:
Experimentally measured wavelengths for the $d^3\Delta(v'=5)-X^1\Sigma^+(v''=0)$ band of $^{12}C^{16}O$.

Line label	**Wavelength [nm]**
${}^{S}R(0)$	151.0341*
${}^{S}R(1)$	151.0306*
${}^{S}R(2)$	151.0298*
${}^{S}R(3)$	151.0318*
${}^{S}R(4)$	151.0365
${}^{R}Q(1)$	151.0429*
${}^{R}Q(2)$	151.0480*
${}^{R}Q(3)$	151.0561*
${}^{R}Q(4)$	151.0669
${}^{Q}P(2)$	151.0604*
${}^{Q}P(3)$	151.0745*
${}^{Q}P(4)$	151.0911

Table 5.11:
Experimentally measured wavelengths for the $a'^3\Sigma^+(v'=14)$–$X^1\Sigma^+(v''=0)$ band of $^{12}C^{16}O$.

Line label	**Wavelength [nm]**
${}^RQ(1)$	141.9474
${}^RQ(2)$	141.9502
${}^RQ(3)$	141.9560
${}^RR(1)$	141.9518
${}^RR(0)$	141.9531
${}^RR(2)$	141.9539
${}^RR(3)$	141.9595
${}^PQ(1)$	141.9637 #
${}^PQ(2)$	141.9741 #
${}^PP(2)$	141.9763 *

Chapter 6

Discussions

6.1 Characterisation of the VUV source

As mentioned in Section 5.1, the phase-matching curve for the TH component was found to be independent of the wavelength and intensity of the non-resonant dye laser, although it is influenced by the intensity of the resonant dye laser and conditions in the heatpipe. This result indicates that there is no measurable competition between the SFM and THG processes and that the nonlinear processes function in the small-signal limit. This result is useful and allows the measurement of absorption spectra without wavelength separation of the SF and TH components. However, the relative noise level increases if wavelength separation is not done.

The variation of the SF signal with wavelength shown in Figure 5-2 illustrates the wide tunability possible in the VUV. The dips in this VUV signal are due to absorption in the magnesium-krypton medium. These dips are not detrimental to the experiment, as they are slowly changing in a continuous fashion over the shorter wavelength ranges scanned in this work. More information of the exact VUV wavelength regions scanned in the experiments are included in Appendix 8.1.

6.2 Introduction to experimental measurements

6.2.1 LIF and absorption spectra

The $A^1\Pi(v' = 3)$–$X^1\Sigma^+(v'' = 0)$ band was investigated in detail in the previous study in our laboratory [1], and measurement of this band was used initially for characterisation purposes and for validation of results obtained. Figure 5-3 shows a section of the $A^1\Pi(v' = 3)$–$X^1\Sigma^+(v'' = 0)$ spectrum, indicating the R(0), R(1), R(2) and R(3) lines. The positions of the higher-J rotational lines R(4), R(5), R(6) and R(7) are also indicated, but these lines are weaker and cannot be resolved because they overlap with the lower-J lines. These relative line intensities correspond qualitatively to the Boltzmann population distributions, however the nonequilibrium conditions in the supersonic expansion show up as a trend that higher-J lines have higher intensities than expected [1].

Typical signal-to-noise ratios in the spectra are up to 500 : 1 for the LIF spectra and 50 : 1 for the absorption spectra for the lowest-J $^{12}C^{16}O$ lines. However, many higher-J lines of $^{12}C^{16}O$ may occur in the absorption spectra but not in the LIF spectra. Another difference is that very few lines of the other isotopomers are visible in the absorption spectrum.

The differences between the LIF and absorption spectral characteristics may be explained by the fact that absorption takes place along the entire beam path through the vacuum chamber and supersonic expansion, whereas the fluorescence is only detected from a small central section, due to the geometry of the detection system. The larger volume in which absorption occurs allows a larger total absorption yield, due to the larger total number of molecules in this path. It also changes the characteristic temperature of the recorded spectrum, as absorption takes place not only in the cold central part of the jet, but also in the outer hotter regions of the jet and in the room temperature background gas in the chamber. For each absorbed photon (molecular excitation), fluorescence occurs in all directions, but only a fraction of this is detected in fluorescence in the small solid angle of the detector used for LIF measurement. In contrast, all absorbed photons contribute to the absorption signal. This explains the strong absorption signals obtained in the experiment.

6.2.2 Calibration of spectra

In the previous work of C.M. Steinmann [1,10], calibration was done using a linear fit of the $^{12}C^{16}O$ and $^{13}C^{16}O$ lines as wavelength references. Reference data were taken from Morton and Noreau (1994) [9] for lines with $J' \leq 6$, and from Tilford *et al.* (1972) [14] for lines with $J' > 6$. The data taken from Tilford *et al.* (1972) [14] were adjusted to correct for an observed systematic shift between the two above-mentioned data sets for $J' \leq 6$.

In the present study more $^{12}C^{16}O$ and $^{13}C^{16}O$ lines with higher-J values were observed than in the previous study. When a larger number of higher-J lines were included in the calibration method used in the previous study, larger errors in the calibration fit resulted. The cause of the larger errors when calibrations were done using large numbers of identified lines was found when comparing calibrated reference lines to their literature values. This is shown in Figure 6-1 for one $A^1\Pi(v' = 3)-X^1\Sigma^+(v'' = 0)$ band calibration. In this calibration the curve fit was linear, with similar results for polynomial fitting procedures. Of importance in this figure is the relative positions of the high-J $^{12}C^{16}O$ and low-J $^{13}C^{16}O$ data points respectively at approximately 144.93 nm, which are systematically shifted relative to one another. This indicates a possible discrepancy of the order of about 0.3 pm between the reference data sets in the region of the low-J $^{13}C^{16}O$ lines.

By using only data from Morton and Noreau (1994) [9] for calibration ($J' \leq 6$), there are three possible calibration methods: (i) using only $^{12}C^{16}O$ lines, (ii) using only $^{13}C^{16}O$ lines, and (iii) using a combination of the two. When the resulting calibrated spectral lines of $^{12}C^{16}O$ and $^{13}C^{16}O$ are compared to data from literature, the differences are up to 0.8 pm offset from the literature values for the calibrations (i) and (ii), as shown in Figure 6-2. Using a combination of the two, as is used in calibrations in this work, was found to give the best fit in both regions, as indicated in the figure, with a combined error margin of less than 0.2 pm. Therefore, in the present study all spectra were calibrated using only Morton and Noreau (1994) [9] and therefore lines with $J' > 6$ were not used as wavelength references.

Previous spectra of the $A^1\Pi(v' = 3)-X^1\Sigma^+(v'' = 0)$ band, four in total, were recalibrated in this way and improved results are included in this dissertation. The calibration error margin can be estimated from the difference between the calibrated reference wavelengths and their corresponding literature wavelengths. These results are described in Section 6.4.2.

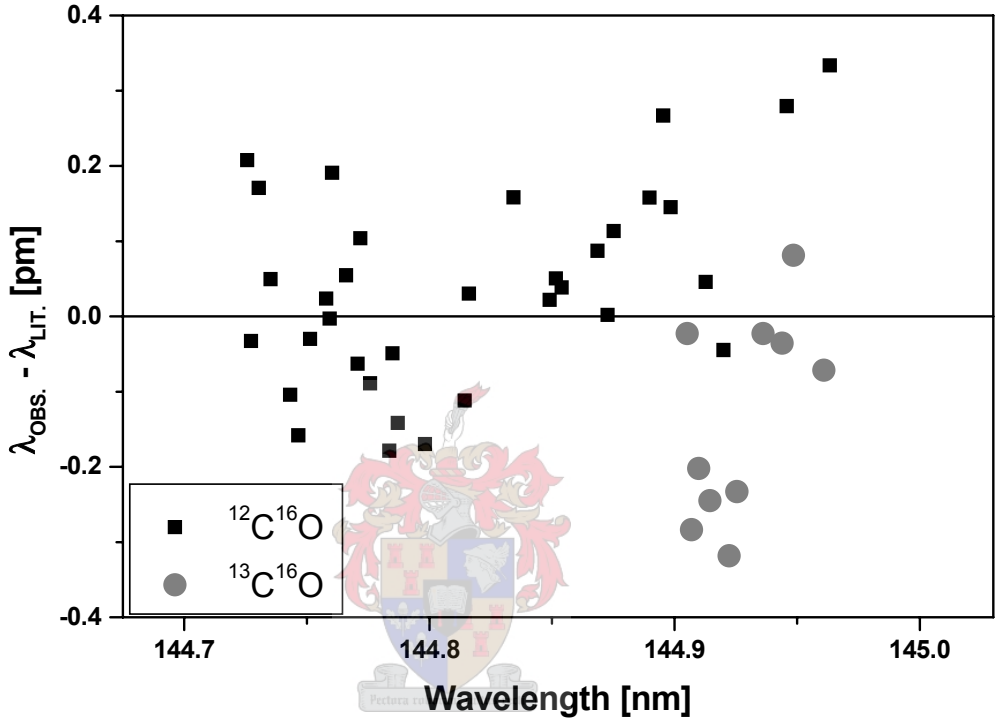

Figure 6-1: Difference between observed wavelengths after calibration (λ_{OBS}) and literature wavelengths (λ_{LIT}) using a large number of higher-J lines of $^{12}C^{16}O$, as well as $^{13}C^{16}O$ lines, in the calibration of the $A^1\Pi(v'=3)-X^1\Sigma^+(v''=0)$ band.

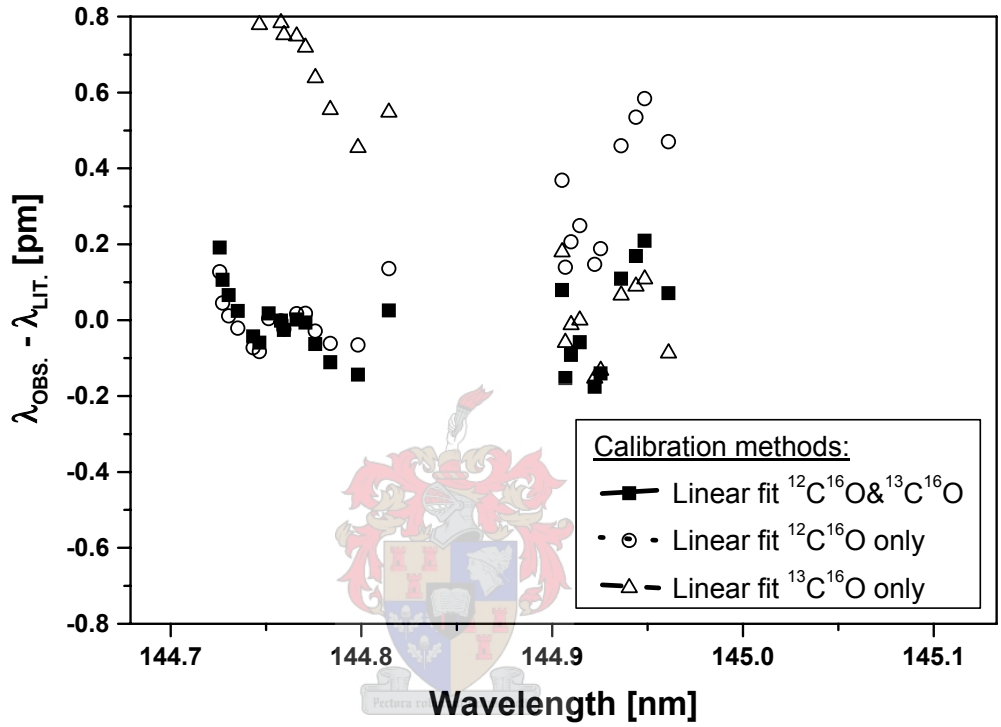

Figure 6-2: Difference between observed wavelengths after calibration (λ_{OBS}) and literature wavelengths (λ_{LIT}) for three different calibration methods, using only lines with $J \leq 6$ (i) of $^{12}C^{16}O$ only ($\circ$), of $^{13}C^{16}O$ only ($\triangle$) and of $^{12}C^{16}O$ and $^{13}C^{16}O$ ($\blacksquare$).

6.2.3 Delay scans

The laser pulse (20 ns pulse duration) can be considered instantaneous compared to the gas pulse (1 ms pulse duration). The rise and fall of the signals in a delay scan are therefore due to the laser and gas pulse interaction during the initial development of the gas pulse (the first molecules through the pulsed nozzle orifice) and after the gas pulse has passed (the last molecules before the pulsed nozzle closes), respectively. The dip or plateau region in between has previously been investigated in detail [1].

The absorption signal is sensitive to the total density of sample gas in the central core of the expansion as well as the density in the outer part of the expansion and the background gas in the chamber. The absorption delay scan therefore has a higher background gas signal compared to that of the LIF delay scan, after the gas pulse has passed.

6.2.4 Spectral line caused by perturbation

The observed spectral line caused by a perturbation (Figure 5-6) shows characteristics of a higher-J line of $^{12}C^{16}O$ for the following reasons. It was observed to have the highest intensity in the measurements of *hot characteristics*, as explained in Section 5.3.4, thereby indicating that it is a higher-J line. It was also observed in the absorption spectrum, as shown in Figure 5-6 (a). Since mostly $^{12}C^{16}O$ lines are found in absorption, this is an indication that it is a transition of $^{12}C^{16}O$ rather than another CO isotopomer. Furthermore, the delay scan profile of this line conforms to the delay scan profiles of typical $^{12}C^{16}O$ lines, with the characteristic dip clearly identifiable in Figure 5-7.

These results have led to the identification of the line as an additional Q(8) line of $^{12}C^{16}O$, which is due to perturbations in this wavelength region. This line, and the perturbation, have been pointed out as being due to the $I^1\Sigma^-(v = 3)$ state [9, 22], affecting the f-parity levels of the $A^1\Pi(v' = 2)$–$X^1\Sigma^+(v'' = 0)$ band with $J' = 7, 8$. For transitions from the $X^1\Sigma^+$ ground state, this affects only the Q(7) and Q(8) lines.

The accurate identification of this line from experimental results demonstrates the sensitivity and versatility of the experimental method.

6.3 Optimisation of experimental conditions

6.3.1 Sample density

By increasing the amount of CO in the sample gas mixture and hence the sample density, increased signal-to-noise ratios of spectral lines in the LIF spectra were observed. An increase in the total CO density in the sample gas mixture was found to increase the signal strength of all spectral lines, including those of the rarer isotopomers. The relative signal increase with increased CO density was generally found to be larger for lines having an initial[1] low intensity compared to the lines having an initial high intensity.

An increase in LIF signal with CO density is expected in the presence of sufficient photons compared to the total number of CO molecules in the beam path. An increase in the number of CO molecules would then cause an increase in the LIF signal of all lines. Since the increase is significantly different for different lines, as illustrated in Figures 5-9 and 5-11, this cannot be the only factor influencing the resulting spectral sensitivity. This additional factor may be one of the following: (i) a saturation effect, (ii) absorption of the emitted fluorescence before it reaches the detector (called self-absorption), or (iii) the effect of higher temperature caused by density increase.

Saturation of the LIF signals can occur in the photomultiplier tube detector, which saturates at a level of $\sim 400 - 500$ mV peak intensity. All LIF signals were observed during experiments to be less than this known saturation level of the photomultiplier tube. However, the response of this detector is not necessarily linear below this level, which may be a contributing factor to the lower relative signal increases with CO density increase for lines having high initial intensity compared to those having low intensity.

In the process of self-absorption, the re-absorbed photon again results in an excited CO molecule, which also fluoresces. However, this secondary fluorescence can occur in any direction. The total number of fluorescence photons reaching the detector would therefore be significantly less than that expected without such an absorption process. The process of self-absorption is expected to increase as the CO density increases since more molecules are available to contribute to this absorption process. Strong lines in the LIF spectra are expected to be affected more

[1] *Initial* refers to the condition before an increase in sample density, i.e. at low sample density.

by self-absorption as the sample density is increased, since the process is dependant on the transition probability.

The sample gas temperature is also expected to increase with increasing CO density, due to less efficient cooling in the supersonic expansion. The Boltzmann distributions in Figure 3-5 illustrate this principle, such that the lines of higher-J value have increased signals with increased temperature, while the lower-J lines have decreased signals. The resulting relative intensities in the observed spectra may be explained by this effect in combination with an overall increase in signal-to-noise ratios in the spectra.

The results in Figure 5-9 and the more detailed results in Figure 5-11 do not entirely contradict the temperature theory, but an unambiguous correlation of intensity increase with J-value and therefore with temperature is not found. Temperature may therefore be a contributing factor but is not the strongest contributor to the resulting spectra.

All three of the above-mentioned theories may explain the observed relative line intensities, or even a combination of these. The effect may be exploited to increase the signal-to-noise ratios of experimental measurements of the weaker CO rovibronic lines, and makes it possible to identify lines previously below the noise level. The only disadvantage of this increase in signal-to-noise ratio in the observed spectra is that there are more overlapping lines, since more lines are present in a given spectrum.

6.3.2 Delay setting

The peak fluorescence signal was found at a different delay time for the rarer isotopomers than for $^{12}C^{16}O$, as illustrated by the experimental results in Figure 5-12. The delay scan shows a different profile for the rarer isotopomers than for $^{12}C^{16}O$, having a triangular shape rather than the plateau profile.

Delay scans of different isotopomer lines which have the same relative intensity in spectra were expected to be similar in intensity and in delay scan profile. The plateau or dip feature of the delay scans of the $^{12}C^{16}O$ lines is observed in all lines of this species, irrespective of signal strength. An example of this is shown in Figure 5-7 (this figure is meant to illustrate the characteristics of an additional Q(8) line caused by perturbation, refer to Section 5.2.4), which shows the delay scans of three lines of $^{12}C^{16}O$ having the dip profiles at different intensities.

The possibility of a purely saturation effect causing the plateau or dip profile may therefore be eliminated on this basis, since its intensity is different for different lines.

One proposed explanation, as also proposed in the previous section concerning CO density increase, is self-absorption. This should be more prominent in the delay scans of the $^{12}C^{16}O$ molecule due to its significantly higher density in the gas jet, according to the natural abundances. Since the density of the rarer isotopomers in the sample gas is lower, self-absorption should be far less significant than with $^{12}C^{16}O$. If a hypothetical triangular shape (similar to those of the rarer isotopomers but having a steeper gradient) is also assumed for the delay scan structure of the $^{12}C^{16}O$ molecule in the absence of any additional absorption and the additional intensity is then absorbed as explained above, this would result in the plateau or dip region of the $^{12}C^{16}O$ delay scan observed. The process of self-absorption therefore satisfactorily explains the observed delay scan profiles.

The different profiles of the delay scans of different isotopomers may be exploited to selectively increase the signals of the rarer isotopomer lines in the spectra. The delay setting used in previous work was 0.41 ms, to correspond to the initial peak of the $^{12}C^{16}O$ signal. The proposed new setting is closer to 0.6 ms, to correspond to the peak of the signals of the other isotopomers. The resulting signals increase by factors of 8 for $^{13}C^{16}O$, 11 for $^{12}C^{18}O$ and 22 for $^{12}C^{17}O$, while the signal of $^{12}C^{16}O$ is decreased by a factor of 1.3. These values are for the R(0) lines of the different isotopomers in the $A^1\Pi(v' = 2)-X^1\Sigma^+(v'' = 0)$ band.

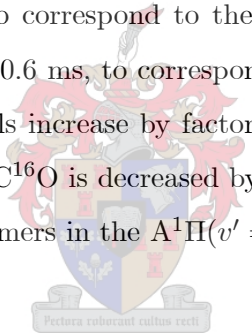

6.3.3 Gas pulse duration

The choice of gas pulse duration has previously been determined by the requirement for short pulses for sufficient flow-cooling of the sample and for maintaining low background gas density. In the light of this, shorter pulses are generally preferable.

Figure 5-13 (a) shows the delay scans of a typical $^{12}C^{16}O$ line for different pulse duration settings. The delay scans clearly show that the absolute signal strength is roughly independent of pulse duration, and that shorter pulses can therefore be used without negatively affecting the signal strengths obtained for $^{12}C^{16}O$.

However, the same does not hold for the delay scan of a typical $^{12}C^{17}O$ line, as shown in Figure 5-13 (b). By changing the pulse duration setting from 0.25 to 0.65 ms, a significant increase

in the signal strength of this delay scan peak is observed. This useful experimental result was applied to selectively enhance the rare isotopomer signals, by increasing the gas pulse duration. The longest pulse duration in this experiment is only limited by the ability of the vacuum pump to maintain a low background pressure at the chosen repetition rate of experiments, as higher background pressures may damage the pressure gauges or the photomultiplier tubes. Higher background gas density may also contribute to the absorption of the VUV excitation radiation and fluorescence by the CO in the background gas. Furthermore, a higher background gas density may cause less efficient flow-cooling in the supersonic expansion.

The delay scans of the typical $^{12}C^{17}O$ line, using pulse duration settings of 0.65 and 0.85 ms, show the triangular profile discussed in Section 6.3.2 as well as an additional tail section. Although the delay scan profile resembles that of the plateau or dip profiles of $^{12}C^{16}O$ in the case of the tail section, it must be noted that the peak is found at a different delay time, and the initial slope is therefore different. This tail section was not further investigated, and illustrates the complexity of the situation. These results were used in the present study to optimise the settings and conditions for detecting rare CO isotopomers, and illustrate interesting future research possibilities. Many of the spectra were therefore recorded using pulse durations of 0.65 ms, which optimises the rare isotopomer signal strengths, with minimal background gas.

6.3.4 Laser energy and alignment

The comparison of the experimental conditions of the two situations giving the *hot* and *cold* spectral characteristics indicate two possible explanations for the differences between the two sets of experimental measurements: (1) the total laser energy and (2) the alignment. As mentioned in Section 5.3.4, there are indications that the total useful SF energy in the *hot* situation was more (by a factor of about 3) than the *cold* situation, but this could not be quantified due to the difficulty in measuring absolute VUV intensities in the present setup. This would explain the increased number of lines observed in terms of an increased amount of total excitation, by increasing the total number of excitation photons. This theory is valid in the situation of a large number of molecules compared to the number of photons. This does not correspond to the explanation of the signal-to-noise ratio increase with sample gas density, as discussed in Section 6.3.1, which suggests a large number of photons compared to the total

number of molecules. It may be possible that the relative number of photons to the number of molecules does not necessarily fall at one of these extremes, but may be in a region in between were both affect the fluorescence intensity.

Another possibility is that the *hot* situation was recorded with an off-centre alignment of the laser through the gas jet. In the supersonic expansion process, the molecules in the centre of the jet will have the lowest temperature, while the molecules in the outer regions of the jet will have a higher temperature. This explanation assumes that an off-centre alignment of the laser through the gas jet causes the increased number of higher-J lines due to the temperature distribution explained in Section 3.3.

Both of these conditions, or a combination of them, may explain the observed differences in the spectra. Both sets of data have been used and details of these are provided in the appendices.

6.4 Spectra of rare isotopomers

6.4.1 Overview of measured spectra

In total, 35 lines of the Fourth Positive System of $^{12}C^{17}O$ and 48 lines of $^{12}C^{18}O$ were identified in recorded spectra and wavelengths determined to an accuracy of ± 0.2 pm. For 29 of the $^{12}C^{17}O$ wavelengths, experimental spectral data have not been published before. A brief discussion of the different band spectra is given below, with more details in Appendix 8.1. Particular attention is given in this discussion to the lowest-J lines ($0 \leq J \leq 6$), which are most important in astrophysics.

In the $A^1\Pi(v' = 5)-X^1\Sigma^+(v'' = 0)$ band, four lines of $^{12}C^{17}O$ and eight lines of $^{12}C^{18}O$ were identified. The wide spacing of lines and the low temperature of the spectrum allowed easy identification with minimal overlapping, however the limiting factor was the signal strengths of the lines. In the $A^1\Pi(v' = 4)-X^1\Sigma^+(v'' = 0)$ band, seven lines of $^{12}C^{17}O$ and seven of $^{12}C^{18}O$ were identified. Similarly, the wide spacing of lines simplified the identification procedure. The $A^1\Pi(v' = 3)-X^1\Sigma^+(v'' = 0)$ band, which was measured in the previous study, was reinvestigated. Under the different experimental conditions used in the present study, additional lines were identified: two of $^{12}C^{17}O$ and three of $^{12}C^{18}O$. Previous spectra were recalibrated

yielding improved values for the previously identified lines in this band. The previously published six lines of $^{12}C^{17}O$ and four of $^{12}C^{18}O$ have been improved using the new calibration technique, with one additional line identified in previously recorded spectra for $^{12}C^{17}O$ and $^{12}C^{18}O$ respectively. In total, nine lines of $^{12}C^{17}O$ and eight of $^{12}C^{18}O$ were identified. In the $A^1\Pi(v'=2)-X^1\Sigma^+(v''=0)$ band, eight lines of $^{12}C^{17}O$ and 11 of $^{12}C^{18}O$ were identified. The R(1) and Q(2) lines of $^{12}C^{17}O$ could not be identified due to overlap with the P(5) and P(6) lines of $^{12}C^{16}O$. In the $A^1\Pi(v'=1)-X^1\Sigma^+(v''=0)$ band, six lines of $^{12}C^{17}O$ and nine of $^{12}C^{18}O$ were identified. Significant overlap of lines occurs, but many of the lines were successfully resolved by analysing spectra taken under different conditions. In the $A^1\Pi(v'=0)-X^1\Sigma^+(v''=0)$ band, only one line of $^{12}C^{17}O$ could be identified and five lines of $^{12}C^{18}O$. This low number of identified lines is due to significant overlap of lines of all isotopomers in this region, due to the small vibrational shifts in this band. The band heads of $^{13}C^{16}O$ and $^{12}C^{18}O$ fall to the short wavelength side of the $^{12}C^{16}O$ band head, in contrast to the structure of the other bands, further complicating the spectra of this band.

6.4.2 Calibration accuracy determination

The observed standard deviations of the calibrations are between 0.11 and 0.21 pm in each vibronic band, separately, and the combined standard deviation of all bands is 0.16 pm. This standard deviation is used as an indication of the accuracy of the calibration. These values compare favourably to the linewidths of the recorded spectral lines, which are determined by the SF component's bandwidth, typically $0.4-0.8$ pm (FWHM). It should also be noted that the step sizes in these experiments range from $0.1-0.2$ pm. The above comparisons indicate the high degree of accuracy of this method of calibration, and specifically indicate that the spectra which are used to identify new lines may safely be assumed to be correctly calibrated to within an accuracy of ± 0.21 pm.

An additional calibration test was the comparison of identified $^{12}C^{18}O$ lines from our calibrated spectra (taken from the tables in Section 5.4.3), and comparison of these wavelengths to the corresponding wavelengths published for this isotopomer [24]. A graphical representation of the differences is shown in Figure 6-3. These differences are scattered around zero, without systematic errors, which is a good indication of the accuracy of the results. The standard devi-

ation in each band is between 0.09 and 0.23 pm, similar to the calibration accuracy. The total standard deviation of the lines of all these bands combined is 0.19 pm. This is an independent validation of the accuracy of the calibrations.

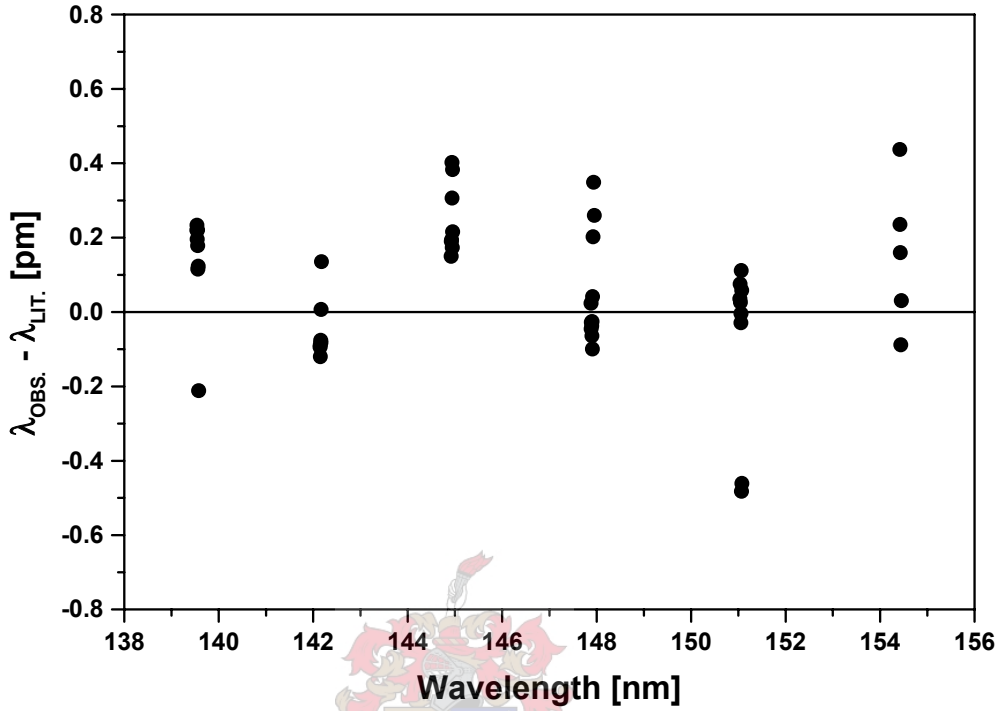

Figure 6-3: Difference between observed wavelengths of $^{12}C^{18}O$ from calibrated spectra (λ_{OBS}) and corresponding literature wavelengths (λ_{LIT}), in all six bands.

6.4.3 Application of results to astrophysical calculations

The experimental results obtained for $^{12}C^{17}O$ and $^{12}C^{18}O$ were applied to a recent problem in astrophysics involving heliocentric velocity calculations [18], using the same method as that employed in the previous study [10]. Sheffer *et al.* [18] reported on high-resolution spectra of the Fourth Positive System of $^{12}C^{17}O$ and $^{12}C^{18}O$ toward the star X Persei, obtained from the spectrograph aboard the Hubble space telescope. Their calculation of the heliocentric velocity of this observed gas cloud in the line of sight toward X Persei resulted in inconsistent velocities when calculated using data of the two isotopomers respectively.

In all four vibronic bands which have been observed by the Hubble space telescope, heliocentric velocities have been calculated with the spectroscopic data obtained in the present study. These calculated heliocentric velocities exhibit much smaller differences between the heliocentric velocities calculated from the $^{12}C^{17}O$ and $^{12}C^{18}O$ data respectively, than found by Sheffer *et al.* [18], who used theoretical estimates for the $^{12}C^{17}O$ wavelengths. The results are shown in Table 6.1. The average difference between the heliocentric velocities calculated from $^{12}C^{17}O$ and $^{12}C^{18}O$ data is 0.15 km.s^{-1} when the spectroscopic data obtained in the present study are used, compared to a difference of 1.48 km.s^{-1} in the analysis of Sheffer *et al.* [18]. A wavelength difference of 0.2 pm (which is the estimated experimental calibration accuracy in the present study) corresponds to 0.4 km.s^{-1} in the heliocentric velocity calculations. Therefore the resulting heliocentric velocity difference of 0.15 km.s^{-1} between the two species is within the experimental error margin. The heliocentric velocity calculated from the $^{12}C^{17}O$ $A^1\Pi(v' = 3)$–$X^1\Sigma^+(v'' = 0)$ data of the present study is smaller by 0.2 km.s^{-1} than results of the previous study [1]. This is due to the recalibration of spectra in the present study. From present results, the average heliocentric velocity of the interstellar gas cloud towards X Persei is $14.5(1) \pm 0.4$ km.s^{-1}.

Table 6.1:
Heliocentric velocities calculated from the experimental wavelength data obtained in the present study compared to those published by Sheffer *et al.* [18] (all in km.s^{-1})

Band Label	**Sheffer *et al.* [18]**			**Present study**		
	$^{12}C^{18}O$	**$^{12}C^{17}O$**	**Difference**	**$^{12}C^{18}O$**	**$^{12}C^{17}O$**	**Difference**
$(2, 0)$	14.8	13.8	1.0	14.8	14.3	0.5
$(3, 0)$	15.0	13.5	1.5	14.5	14.3	0.2
$(4, 0)$	14.4	13.4	1.0	14.6	14.9	-0.3
$(5, 0)$	15.9	13.5	2.4	14.4	14.2	0.2
AVERAGE:	15.03	13.55	1.48	14.58	14.43	0.15

6.5 Spectra of singlet-triplet transitions

In this study, 32 lines corresponding to excitation from the singlet electronic ground state $X^1\Sigma^+$ to electronic triplet excited states were detected. According to a comprehensive review

by Eidelsberg and Rostas [30] and the online database [31] maintained by Eidelsberg, accurate experimental wavelengths for 10 of these lines have not been experimentally determined before. The spectra with identified lines and corresponding labels may be found in Appendix 8.1, together with a description of the experimental conditions. The singlet-singlet lines in the vicinity of each singlet-triplet band were used for calibration. The wavelengths of the measured singlet-triplet lines were compared to their values from literature, if such values were available, as is shown in the graphs in Appendix 8.1. The differences between measured and literature wavelengths are slightly larger than the error margins of calibrations, indicating a slightly larger error margin on these wavelengths, which is discussed for each of these bands separately in Appendix 8.1.

Since these singlet-triplet lines are spin-forbidden transitions, due to the quantum-mechanical Selection Rule 3.3, they have low transition probabilities and the excited states have long fluorescence lifetimes. The low transition probability causes the small relative signals in typical spectra, while the longer fluorescence lifetime is demonstrated by the measurement shown in Figure 5-18. The low transition probability makes the spectral linewidth extremely narrow, according to the Heisenberg uncertainty principle. The lines are, however, observed to have similar experimental spectral linewidths than the singlet-singlet lines (comparison of $0.4 - 0.8$ pm compared to the singlet-triplet linewidths of typically 0.4 pm). This may be explained by the experimental limitation induced by the laser bandwidth, which is larger than the linewidth of the singlet and triplet levels probed. Nevertheless, lines are resolved and accurate wavelengths were determined.

Chapter 7

Conclusions and outlook

7.1 Summary

The astrophysically-relevant rovibronic lines of the Fourth Positive System $A^1\Pi - X^1\Sigma^+$ of $^{12}C^{16}O$, $^{13}C^{16}O$, $^{12}C^{17}O$ and $^{12}C^{18}O$ have been recorded at high resolution using laser-induced fluorescence excitation spectroscopy and absorption spectroscopy in a natural CO sample. This technique involved the use of a tunable narrow-bandwidth vacuum ultraviolet laser source for selective rovibronic excitation of CO molecules and subsequent detection of the laser-induced fluorescence and absorption as a function of excitation wavelength.

The vacuum ultraviolet laser source was generated by sum-frequency mixing of visible dye laser pulses. In this study, the first dye laser was always operated at the two-photon resonance of 430.88 nm, while the second dye laser was operated in wavelength regions between 390 and 545 nm, using five different dyes. The resulting vacuum ultraviolet wavelengths lie in the range $139 - 155$ nm. The molecules were introduced by pulsed supersonic expansion, facilitating a large population of CO molecules in the low-J'' rotational levels of the $v'' = 0$ vibrational level of the electronic ground state. This facilitated a high sensitivity, allowing the detection of rare CO isotopomers in a natural sample. Furthermore, the flow cooling induced by the supersonic expansion simplified the spectra since the rotational temperatures reached were similar to those in the interstellar medium, and allowed the detection of the astrophysically-relevant lines.

The specific rovibronic transitions of astrophysical interest lie in the vibronic bands $A^1\Pi(v' = 2-5) - X^1\Sigma^+(v'' = 0)$. The vibronic bands investigated in this study were the bands $A^1\Pi(v' =$

$0-5)-X^1\Sigma^+(v''=0)$. This included a reinvestigation of the vibronic band measured in the previous study $A^1\Pi(v'=3)-X^1\Sigma^+(v''=0)$ and additionally two vibronic bands which have not yet been astronomically observed $A^1\Pi(v'=0,1)-X^1\Sigma^+(v''=0)$. Although these have not yet been detected astronomically, they have a relatively high transition probability [17] and were therefore additionally recorded. The vibronic bands having $v'>5$ have smaller transition probabilities and excitation of these were not possible with the current experimental setup, since their excitation wavelengths ($\lambda < 139$ nm) are shorter than what is possible in the magnesium heatpipe.

The lines detected in each band comprised those with low J value due to the flow cooling. These are also the lines observed most often in astrophysics, due to the low temperature in interstellar space (~ 4 K). Currently the lines R(0), R(1) and Q(1) of $^{12}C^{17}O$ and $^{12}C^{18}O$ are of specific interest since these have been observed astronomically. In our spectra we have detected these lines, with some exceptions when overlapping occurs with lines of the more abundant CO isotopomers $^{12}C^{16}O$ and $^{13}C^{16}O$. These exceptions are the R(1) line in the $A^1\Pi(v'=2)-X^1\Sigma^+(v''=0)$ band and the R(1) and Q(1) lines in the $A^1\Pi(v'=0)-X^1\Sigma^+(v''=0)$ band.

In total, the wavelengths of 35 rovibronic lines of $^{12}C^{17}O$ are presented in this work. Of these, 29 have not been published before and six have been determined in previous work in our laboratory [1]. The spectra of the $A^1\Pi(v'=3)-X^1\Sigma^+(v''=0)$ band recorded in the above-mentioned study [1] have been reinvestigated and recalibrated using the improved calibration technique. Improved wavelengths have therefore been assigned to the six previously identified lines and one additional line has been identified in the reinvestigation process. The difference between previously reported wavelengths and new wavelengths for these lines falls within the experimental error margin of ± 0.2 pm.

In the work of Sheffer *et al.* [18], heliocentric velocities were calculated for a gas cloud observed in the line-of-sight toward the star X Persei. Since no laboratory wavelengths were available for the $^{12}C^{17}O$ isotopomer, calculated wavelengths were used. This resulted in an apparent difference between the heliocentric velocities calculated for the $^{12}C^{17}O$ and $^{12}C^{18}O$ isotopomers in the same gas cloud, which is highly improbable. The new wavelengths of $^{12}C^{17}O$ determined in this study have been applied to recalculate the heliocentric velocity of this observed gas cloud. The difference between the heliocentric velocities calculated when using the

new data compared to the results of Sheffer *et al.* [18] has been decreased from 1.48 km.s^{-1} to 0.15 km.s^{-1}, averaged over all four vibronic bands detected astronomically. This resolves the apparent discrepancy in the calculations to within the experimental error margin of $\pm$0.4 km.s^{-1}.

The experimental conditions for detection of rare CO isotopomers have been optimised in this study. The density of the CO sample in the supersonic expansion was increased by using pure CO gas rather than CO in a carrier gas. This had the effect of increasing the total number of CO molecules in the sample and therefore increasing the signal-to-noise ratios of the LIF spectra significantly. This increased the temperature reached in the supersonic expansion and therefore changed the relative population of rotational levels in the ground state, resulting in a larger number of lines observed. A compromise must be found between an increase in signal-to-noise ratio and an overlapping of a large number of lines. Furthermore, changes in the temporal overlap of the gas and laser pulses indicated that the optimal delay time is different for different isotopomers. Optimisation of the signals of the rare isotopomers was done by adjusting the temporal delay setting. The improved experimental conditions allowed the detection of a large number of lines, many more than in previously recorded spectra.

The calibration technique was improved in this study by using reference wavelengths of the $J \leq 6$ lines of $^{12}C^{16}O$ and $^{13}C^{16}O$ from Morton and Noreau (1994) [9]. Recalibration of previously recorded spectra provide improved wavelengths for the lines in the $A^1\Pi(v' = 3)-X^1\Sigma^+(v'' = 0)$ band, although both sets of results lie within the experimental error margin.

The viability of using absorption spectra as an additional source of information in spectral analysis has been demonstrated in this study. The combination of a large density of CO molecules in the supersonic expansion, and the addition of a vacuum monochromator to select the transmitted VUV component of interest, has resulted in good signal-to-noise ratios for the absorption spectra. The characteristics of these spectra are different from the LIF spectra, one of the most important differences being the fact that mostly $^{12}C^{16}O$ lines are detected and the rarer isotopomers have negligibly small signals, which was useful in identification of spectral lines. Possible non-fluorescent transitions may be detected using this technique, although none were detected in this study in the wavelength regions investigated.

Additional results of scientific interest include the detection of so-called singlet-triplet lines.

A total of 32 rovibronic lines originating from transitions between the singlet electronic ground state and triplet electronically excited states have been detected in the wavelength regions investigated in this study. Of these, 10 have not yet been detected before in a laboratory. These lines are also of interest in astrophysics, since astronomically detected absorption lines of low transition probability are not subject to saturation in the interstellar medium and more accurate column densities can be determined from such measurements.

7.2 Conclusion

The combination of a tunable, narrow bandwidth VUV source and a supersonic expansion of CO in natural abundance was used to resolve rovibronic lines in the $A^1\Pi(v' = 0-5)-X^1\Sigma^+(v'' = 0)$ bands for the CO isotopomers $^{12}C^{16}O$, $^{13}C^{16}O$, $^{12}C^{18}O$ and $^{12}C^{17}O$ and determine accurate laboratory measured wavelengths for $^{12}C^{17}O$ and $^{12}C^{18}O$. The spectral results presented on 29 of the $^{12}C^{17}O$ lines have not been experimentally measured before. The new spectral data were used to resolve a discrepancy in the calculation of heliocentric velocities from $^{12}C^{17}O$ and $^{12}C^{18}O$ spectra measured in the interstellar medium. The vibronic bands of $^{12}C^{17}O$ that have been characterised spectroscopically in this study constitute those most relevant to astrophysics at the present time.

7.3 Outlook

Future work would include the systematic measurement of other singlet-triplet lines of relevance in astrophysics, since many of these are still required. Such further work is envisaged using an online calibration technique, using a Te absorption cell for wavelength calibration of the visible dye laser. This will become necessary when measuring lines that lie far from the region of well-known CO singlet-singlet lines.

A new heatpipe and experimental setup for generating wavelengths in the range of $120-140$ nm are envisaged in the near future, which will make the detection of the higher-lying states in the Fourth Positive System possible.

Other possible applications include further searches into CO van der Waals molecules, and other small molecules of scientific and industrial interest. Such investigations will be specifically

viable when isotopomer detection is required. A combination of the present setup with a linear time-of-flight mass spectrometer may allow the detection of possible van der Waals molecules. An initial study generating I_2 van der Waals molecules may be required to characterise the conditions required for such cluster growth and detection. The optimisations applied in this work pave the way for further work in all the above-mentioned research directions.

Chapter 8

Appendices

8.1 Appendix A: Detailed spectra

This appendix contains detailed spectral results and discussions of the six Fourth Positive System vibronic bands and the three singlet-triplet bands recorded by continuous scans[1] in this study. Experimental conditions of each recorded band are discussed and appropriate experimental spectra are presented, with discussion of the line identification procedure used.

8.1.1 $\mathbf{A}^1\Pi(v'=5)-\mathbf{X}^1\Sigma^+(v''=0)$

The LIF and absorption spectra of the $A^1\Pi(v'=5)-X^1\Sigma^+(v''=0)$ band are shown in Figure 8-1. The assigned lines of $^{12}C^{16}O$ and $^{13}C^{16}O$ having $J \leq 6$ are labelled, and the R(0) lines of $^{12}C^{17}O$ and $^{12}C^{18}O$ are also labelled. The lines of the rare $^{12}C^{17}O$ lines of interest have a much smaller relative intensity and are better visible in the detailed graph in Figure 8-2.

This band was measured by a continuous scan in the wavelength range from $139.23-139.57$ nm. The non-resonant dye laser was operated at wavelengths in the range $393.6-396.5$ nm using the grating order 7, with approximately 0.5 mJ (at 399 nm) obtained using *PBBO dye* in *propylene carbonate (PC)* as solvent. The specific experimental conditions were as follows: 4 bar pure CO was expanded in supersonic expansion, the gas pulse duration setting was 0.65 ms,

[1] Continuous scan refers to a continuous measurement in small wavelength steps towards longer wavelengths, with minimal interruptions. Larger wavelength regions recorded using the same step sizes physically take longer to record. The longest continuous wavelength scan was the (5,0) band due to the wider spacing of lines, taking approximately 8 hours in recording time.

the delay between gas and laser pulses was 0.65 ms, the wavelength step size of the non-resonant dye laser was 1.5 pm, the repetition rate was 5 Hz, data averaging of each point was done over 10 laser shots, and the absorption spectrum was recorded without wavelength separation.

The LIF spectral lines in this band are widely spaced and the only significant overlap was that of the Q(4) and P(2) lines of the same isotopomer, for both $^{12}C^{16}O$ and $^{13}C^{16}O$. In both cases the line was considered to correspond to P(2) due to the expected lower intensity of Q(4), from inspection of relative intensities in the respective branches. The $^{13}C^{16}O$ Q(5) line overlapped the $^{12}C^{18}O$ R(0) line. In this case the Q(5) line was considered negligible due to its expected lower intensity and the line was assigned R(0).

The absorption spectrum contains much noise due to the long timescale of this spectral measurement (due to the wide spacing and vibrational isotopic shifts of the lines). The baseline of the absorption spectrum shifts over long time periods and more dips in the VUV signal due to crystal growth in the heatpipe may be observed, resulting in artificial features in the absorption spectrum.

A detailed graph of the LIF spectrum of the $A^1\Pi(v' = 5)-X^1\Sigma^+(v'' = 0)$ band, showing specifically the region of $^{12}C^{17}O$ lines, is found in Figure 8-2. In this band, four lines of $^{12}C^{17}O$ were detected, as indicated: R(1), R(0), Q(1) and Q(2). The expected line positions of the $^{12}C^{16}O$ lines in this wavelength region are indicated. By observing the positions of the expected $^{12}C^{16}O$ lines P(9), Q(12) and R(16), and finding no signal above the noise level, it may be assumed that higher-J lines in each branch also have signals below this level. Therefore possible overlap of the $^{12}C^{16}O$ R(17) line with the $^{12}C^{17}O$ Q(1) line is resolved and the line may be safely identified as $^{12}C^{17}O$ Q(1).

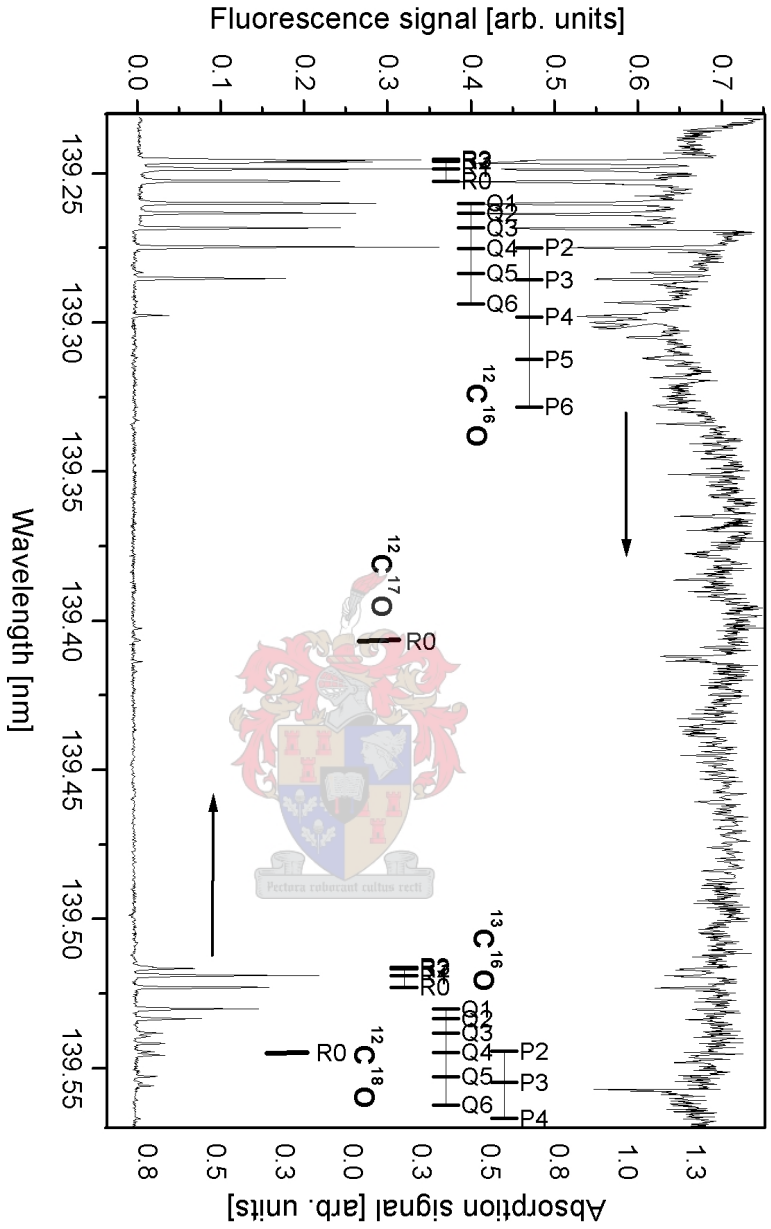

Figure 8-1: Experimental LIF (lower) and absorption (upper) spectra of the $A^1\Pi(v' = 5)-X^1\Sigma^+(v'' = 0)$ band, with the positions of the lowest-J lines of $^{12}C^{16}O$ and $^{13}C^{16}O$ indicated, as well as R(0) of $^{12}C^{17}O$ and $^{12}C^{18}O$.

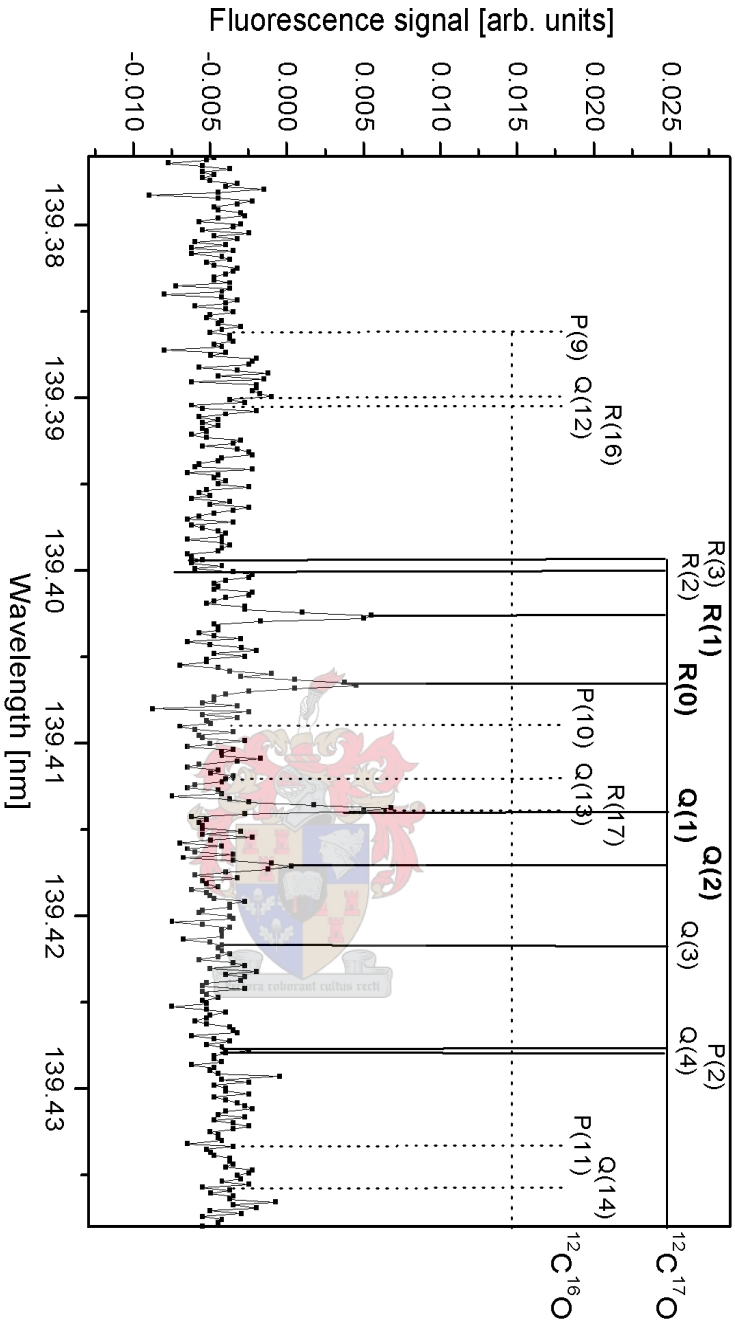

Figure 8-2: Experimental LIF spectrum of the $A^1\Pi(v' = 5)-X^1\Sigma^+(v'' = 0)$ band, showing the positions of the $^{12}C^{17}O$ lines (solid lines) and the positions of expected $^{12}C^{16}O$ lines (dotted lines).

8.1.2 $\mathbf{A}^1\Pi(v'=4)-\mathbf{X}^1\Sigma^+(v''=0)$

The LIF and absorption spectra of the $A^1\Pi(v'=4)-X^1\Sigma^+(v''=0)$ band are shown in Figure 8-3. The assigned lines of $^{12}C^{16}O$ and $^{13}C^{16}O$ having $J \leq 6$ are labelled, and the R(0) lines of $^{12}C^{17}O$ and $^{12}C^{18}O$ are also labelled. The lines of the rare $^{12}C^{17}O$ lines of interest have a smaller relative intensity and are better visible in the detailed graph in Figure 8-4.

This band was measured by continuous scans in sections in the wavelength range from $141.88 - 142.19$ nm. The gaps in the spectrum are regions omitted from the measurements, due to a lack of interesting lines expected in these regions. The dye laser was operated at wavelengths in the range $415.74 - 418.25$ nm using the grating order 7, with approximately 0.2 mJ (at 418 nm) obtained using *stilbene 3 dye* in *methanol* as solvent. The experimental conditions were as follows: 4 bar pure CO was expanded in supersonic expansion, the gas pulse duration setting was 0.65 ms, the delay between gas and laser pulses was 0.65 ms, the wavelength step size of the non-resonant dye laser was 1.5 pm, the repetition rate was 5 Hz, data averaging of each point was done over 10 laser shots, and the absorption spectrum was measured without wavelength separation.

The LIF spectral lines of $^{12}C^{16}O$ and $^{13}C^{16}O$ in this band are widely spaced, with little overlap between lines. The $^{13}C^{16}O$ lines Q(3) and Q(4) were not identified due to their low relative intensity and partial overlap with other stronger lines.

The absorption spectrum shows strong absorption lines corresponding to $^{12}C^{16}O$ lines. Many higher-J lines of $^{12}C^{16}O$ occur in absorption but not in fluorescence. The baseline "jump" in the absorption spectrum observed at 142.1660 nm was observed twice, but not investigated further. This is probably due to changes in the intensity of the VUV beam.

A detailed graph of the LIF spectrum of the $A^1\Pi(v'=4)-X^1\Sigma^+(v''=0)$ band showing specifically the region of $^{12}C^{17}O$ lines, is found in Figure 8-4. In this band, seven lines of $^{12}C^{17}O$ were detected, as indicated: R(3), R(2), R(1), R(0), Q(1), Q(2) and Q(3). The expected line positions of the $^{12}C^{16}O$ lines in this wavelength region are shown. These do not overlap the expected positions of $^{12}C^{17}O$ lines and also have low signals in this experiment. Both of these factors allow the easy identification of the $^{12}C^{17}O$ lines.

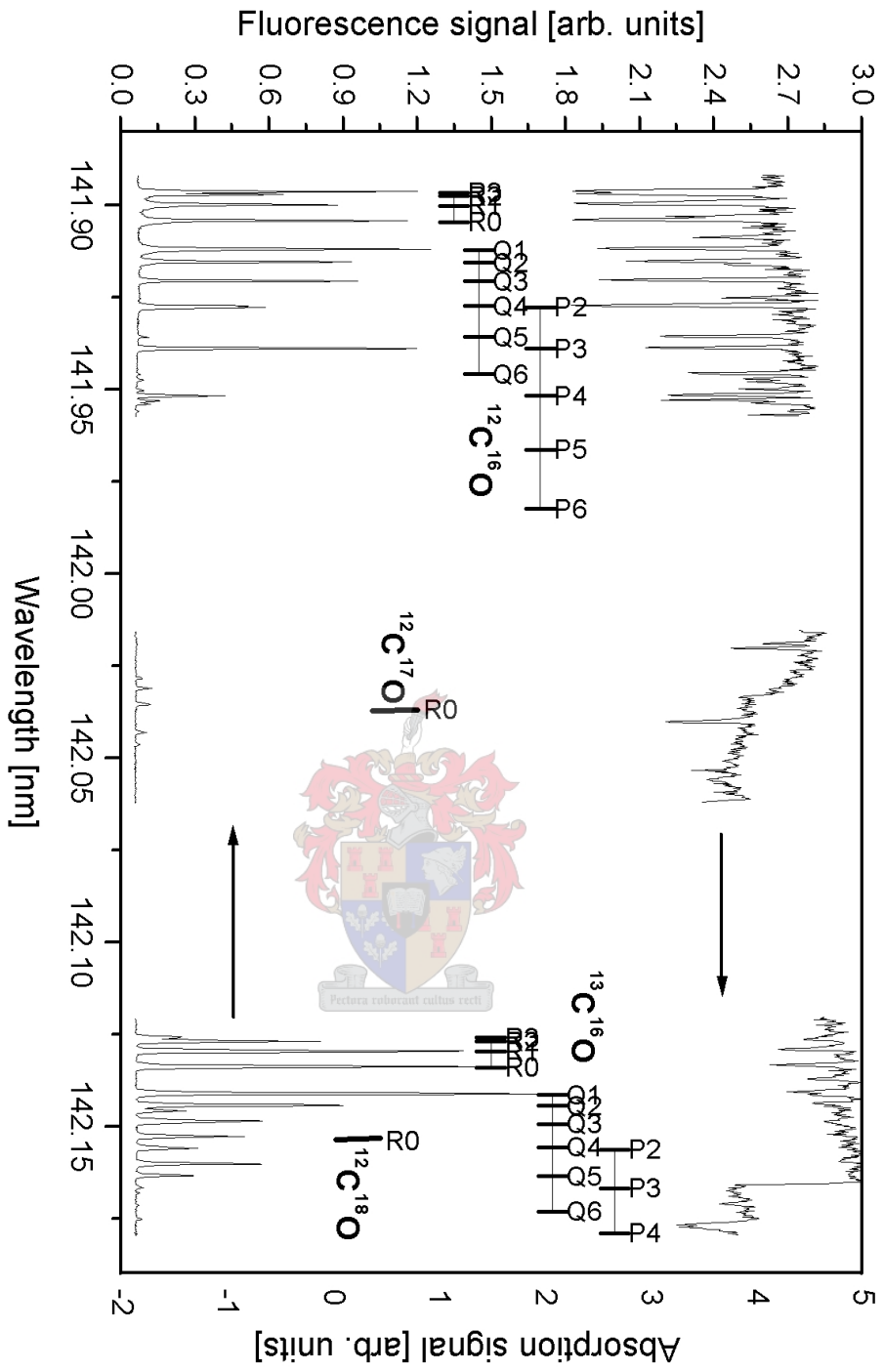

Figure 8-3: Experimental LIF (lower) and absorption (upper) spectra of the $A^1\Pi(v' = 4)-X^1\Sigma^+(v'' = 0)$ band, with the positions of the lowest-J lines of $^{12}C^{16}O$ and $^{13}C^{16}O$ indicated, as well as R(0) of $^{12}C^{17}O$ and $^{12}C^{18}O$.

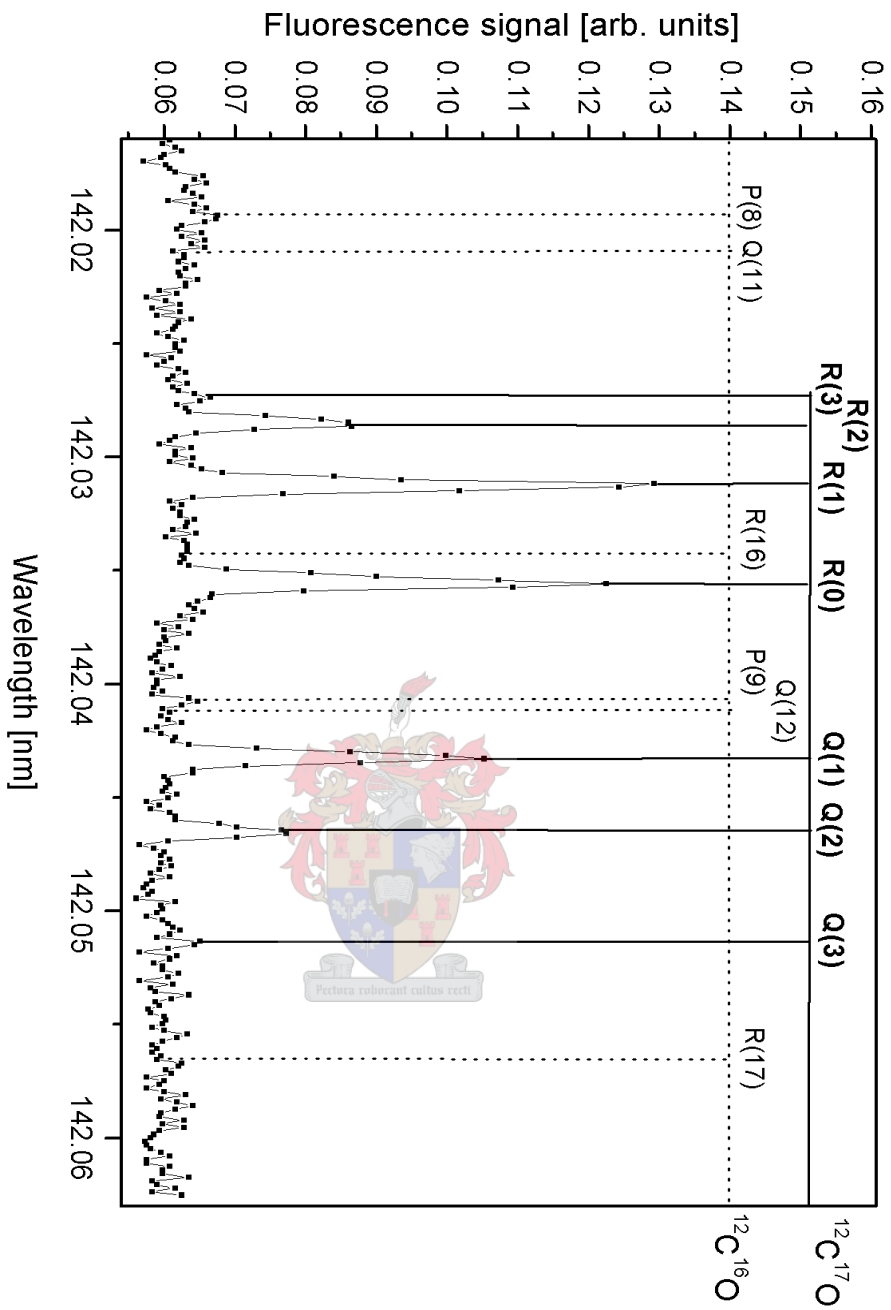

Figure 8-4: Experimental LIF spectrum of the $A^1\Pi(v' = 4)-X^1\Sigma^+(v'' = 0)$ band, indicating the region of $^{12}C^{17}O$ lines (solid lines) and the positions of expected $^{12}C^{16}O$ lines (dotted lines).

8.1.3 $\mathbf{A}^1\Pi(v'=3)-\mathbf{X}^1\Sigma^+(v''=0)$

The LIF and absorption spectra of the $A^1\Pi(v'=3)-X^1\Sigma^+(v''=0)$ band are shown in Figure 8-5. The assigned lines of $^{12}C^{16}O$ and $^{13}C^{16}O$ having $J \leq 6$ are labelled, and the R(0) lines of $^{12}C^{17}O$ and $^{12}C^{18}O$ are also labelled. The lines of the rare $^{12}C^{17}O$ lines of interest have a smaller relative intensity and are better visible in the detailed graph in Figure 8-6.

This band has been studied previously and was measured here largely as a repeatability exercise. However, during the course of the implementation of improved experimental conditions, it was found that additional lines could be identified. The continuous scan of this band was done in the wavelength range $144.72 - 144.97$ nm. The dye laser was operated at wavelengths in the range $440.8 - 444.7$ nm using the grating order 7, with approximately 1.1 mJ (at 440 nm) obtained using *coumarin 440 dye* in *methanol* as solvent. The experimental conditions were as follows: 4 bar pure CO was expanded in supersonic expansion, the gas pulse duration setting was 0.25 ms, the delay between gas and laser pulses was 0.65 ms, the wavelength step size of the non-resonant dye laser was 1.5 pm, the repetition rate was 5 Hz, data averaging of each point was done over 10 laser shots, and the absorption spectrum was measured with wavelength separation through the monochromator. Besides this continuous measurement, four spectra of the previous study were recalibrated.

The specific LIF spectrum presented in Figure 8-5 refers to the experimental conditions exhibiting *hot* spectral characteristics, as discussed in Section 5.3.4. This results in a larger number of higher-J lines and therefore more line overlap in general. Due to the higher signals of the more abundant isotopomers, these could be identified easily. The only exceptions were some lines of $^{13}C^{16}O$ which could not be resolved due to partial overlap and smaller relative signals.

The absorption spectrum shows a baseline drift, which is attributed to a decrease in VUV signal with wavelength in this wavelength range (this is due to a magnesium absorption as discussed previously [1], [57]). As in all absorption spectra, some higher-J lines of $^{12}C^{16}O$ are visible which are not visible in fluorescence.

A detailed graph of the LIF spectrum of the $A^1\Pi(v'=3)-X^1\Sigma^+(v''=0)$ band, showing specifically the region of $^{12}C^{17}O$ lines, is found in Figure 8-6. In this measurement, six lines of $^{12}C^{17}O$ were detected, as indicated: R(3), R(2), R(0), Q(1), Q(4) and P(2). The expected

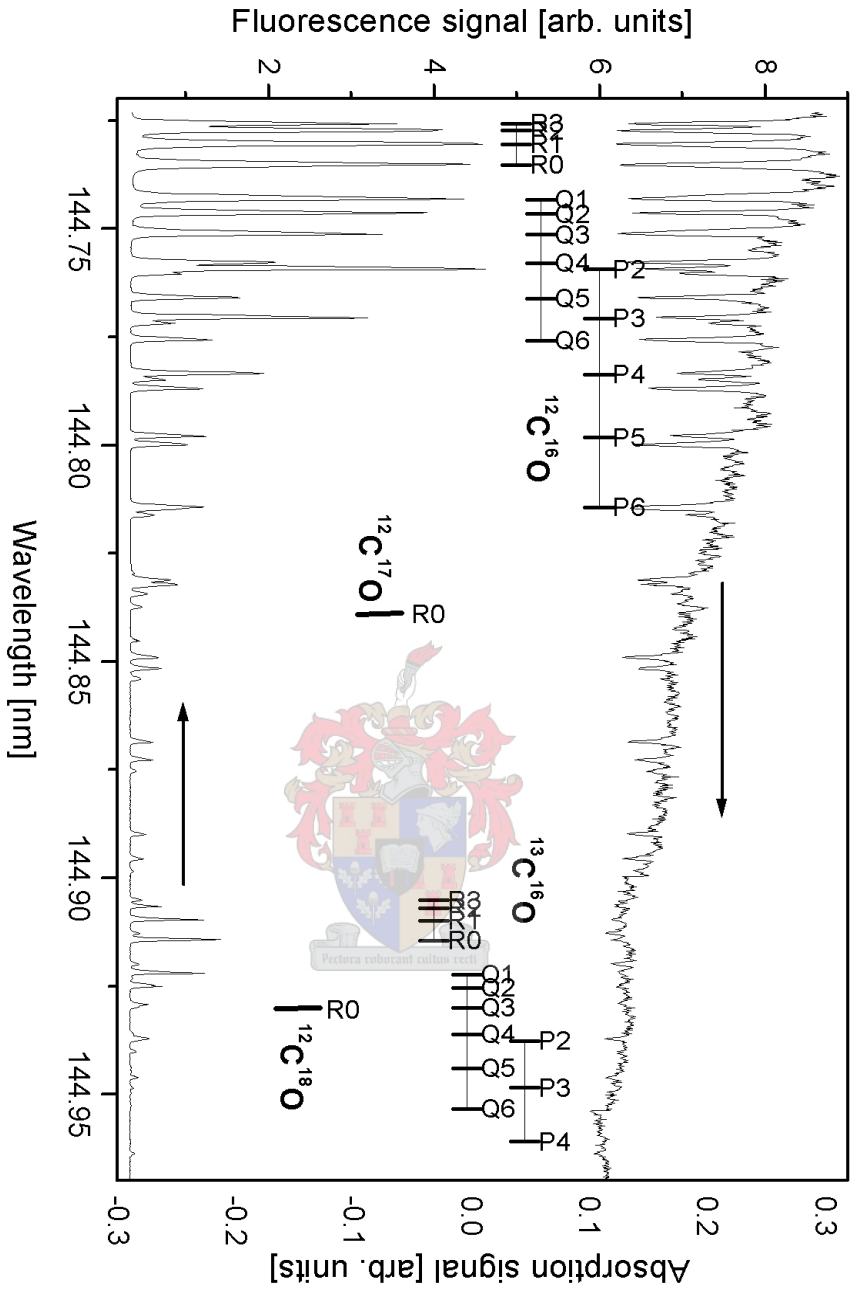

Figure 8-5: Experimental LIF (lower) and absorption (upper) spectra of the $A^1\Pi(v' = 3)-X^1\Sigma^+(v'' = 0)$ band, with the positions of the lowest-J lines of $^{12}C^{16}O$ and $^{13}C^{16}O$ indicated, as well as R(0) of $^{12}C^{17}O$ and $^{12}C^{18}O$.

line positions of the $^{12}C^{16}O$ lines in this wavelength region are indicated. These lines have high relative signals in this experiment, due to the *hot* spectral characteristics. Although this limits the identification of lines due to overlap, the improved signal-to-noise ratios allow the identification of a number of $^{12}C^{17}O$ lines not detected in previous experiments.

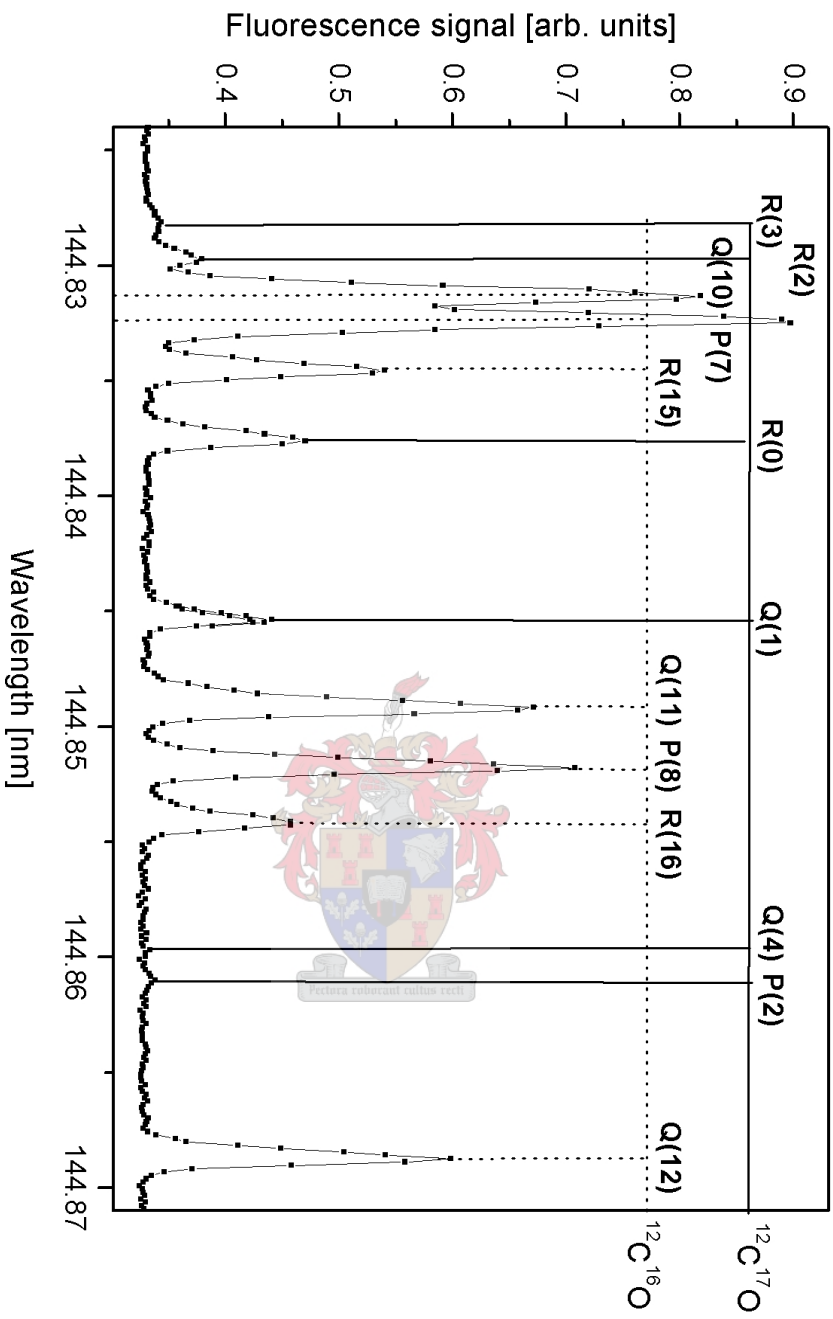

Figure 8-6: Experimental LIF spectrum of the $A^1\Pi(v' = 3)-X^1\Sigma^+(v'' = 0)$ band, indicating the region of $^{12}C^{17}O$ lines (solid lines) and the positions of expected $^{12}C^{16}O$ lines (dotted lines).

8.1.4 $\mathbf{A}^1\Pi(v'=2)-\mathbf{X}^1\Sigma^+(v''=0)$

The LIF and absorption spectra of the $A^1\Pi(v'=2)-X^1\Sigma^+(v''=0)$ band are shown in Figure 8-7. The assigned lines of $^{12}C^{16}O$ and $^{13}C^{16}O$ having $J \leq 6$ are labelled, and the R(0) lines of $^{12}C^{17}O$ and $^{12}C^{18}O$ are also labelled. The lines of the rare $^{12}C^{17}O$ lines of interest have a smaller relative intensity and are visible on this scale as very small peaks, and are also better visible in the detailed graph in Figure 8-8.

This band was measured by continuous scans on three occasions in the wavelength range from $147.74-147.91$ nm. The dye laser was operated at wavelengths in the range $470.2-473.5$ nm using the grating order 6, with approximately 1 mJ (at 480 nm) on all three occasions, obtained using *coumarin 480 dye* in *methanol* as solvent. The experimental conditions on the three occasions were as follows: 4 bar pure CO was expanded in supersonic expansion, the gas pulse duration settings on the three occasions were (i) 0.25 ms (ii) 0.65 ms (iii) 0.65 ms, the delay between gas and laser pulses was 0.65 ms throughout, the wavelength step sizes of the non-resonant dye laser were (i) 1.5 pm (ii) 1 pm (iii) 1 pm, the repetition rates were (i) 10 Hz (ii) 5Hz (iii) 5 Hz, data averaging of each point was done over 10 laser shots, and absorption spectra were measured with wavelength separation on one occasion (i), and without separation in (ii) and (iii). The experimental conditions for (i) was according to the *hot* spectral characteristics and for (ii) and (iii) according to *cold* characteristics.

The LIF spectrum presented in Figure 8-7 refers to the experimental conditions (ii) above; it therefore exhibited *cold* spectral characteristics. This results in a smaller number of lines and therefore less overlap in general. It is interesting to note in the LIF spectrum that the $^{13}C^{16}O$ lines appear stronger than the $^{12}C^{16}O$ lines. This may be explained by the improved experimental conditions applied to detect the rarer isotopomers, selectively enhancing their signals, as discussed in Section 5.3. Physically, the different isotopomers may also have different Franck-Condon factors and this may be a contributing factor to the relative signal strengths.

The absorption spectrum shows many higher-J lines of $^{12}C^{16}O$ which are not visible in fluorescence, even up to the P(9) line, as an example. Since the wavelength region scanned becomes shorter and the time of recording a spectrum becomes correspondingly shorter, the absorption spectrum background noise decreases (at least the baseline shift). This may be observed by comparison of the absorption spectra of this and other bands recorded over a

longer total time, for example the $A^1\Pi(v' = 5)-X^1\Sigma^+(v'' = 0)$ band, which shows a much larger noise level in the absorption spectrum.

A detailed graph of the LIF spectrum of the $A^1\Pi(v' = 2)-X^1\Sigma^+(v'' = 0)$ band, showing specifically the region of $^{12}C^{17}O$ lines, is found in Figure 8-8. In the spectrum shown here, six lines of $^{12}C^{17}O$ were detected, as indicated: R(3), R(2), R(0), Q(1), Q(3), P(2). The expected line positions of the $^{12}C^{16}O$ lines in this wavelength region are indicated. Overlapping of the $^{12}C^{16}O$ P(5) line with the R(1) line of $^{12}C^{17}O$ occurs, and the latter is considered negligible due to inspection of the relative intensity of the $^{12}C^{16}O$ P(4) line. Similarly, the $^{12}C^{16}O$ P(6) line overlaps the $^{12}C^{17}O$ Q(2) line, and the latter cannot be assigned. The $^{12}C^{17}O$ P(3) line indicated in the graph was not entirely resolved above the noise level, and therefore not assigned a wavelength. Of the nine lines of $^{12}C^{17}O$ indicated in the figure, six were identified in this spectrum.

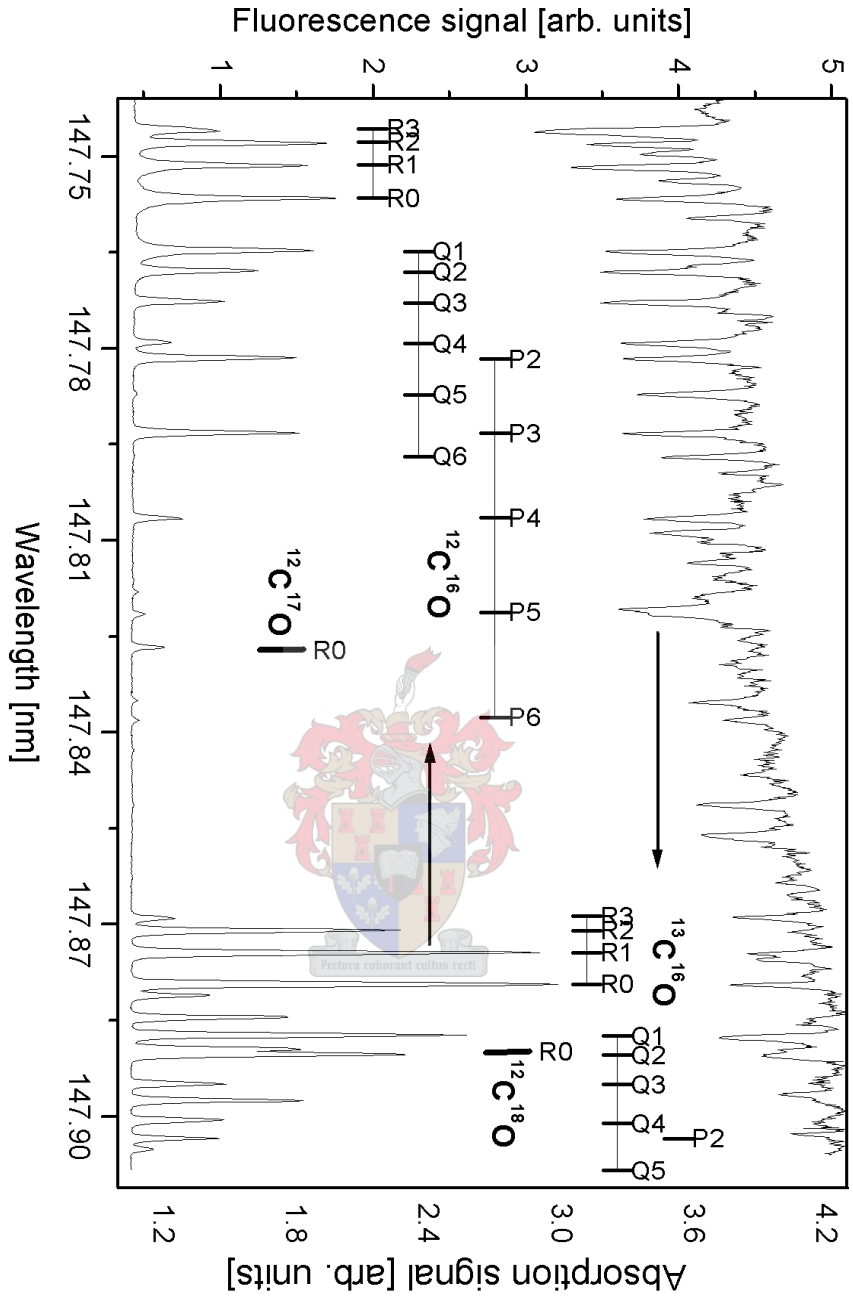

Figure 8-7: Experimental LIF (lower) and absorption (upper) spectra of the $A^1\Pi(v' = 2)-X^1\Sigma^+(v'' = 0)$ band, with the positions of the lowest-J lines of $^{12}C^{16}O$ and $^{13}C^{16}O$ indicated, as well as R(0) of $^{12}C^{17}O$ and $^{12}C^{18}O$.

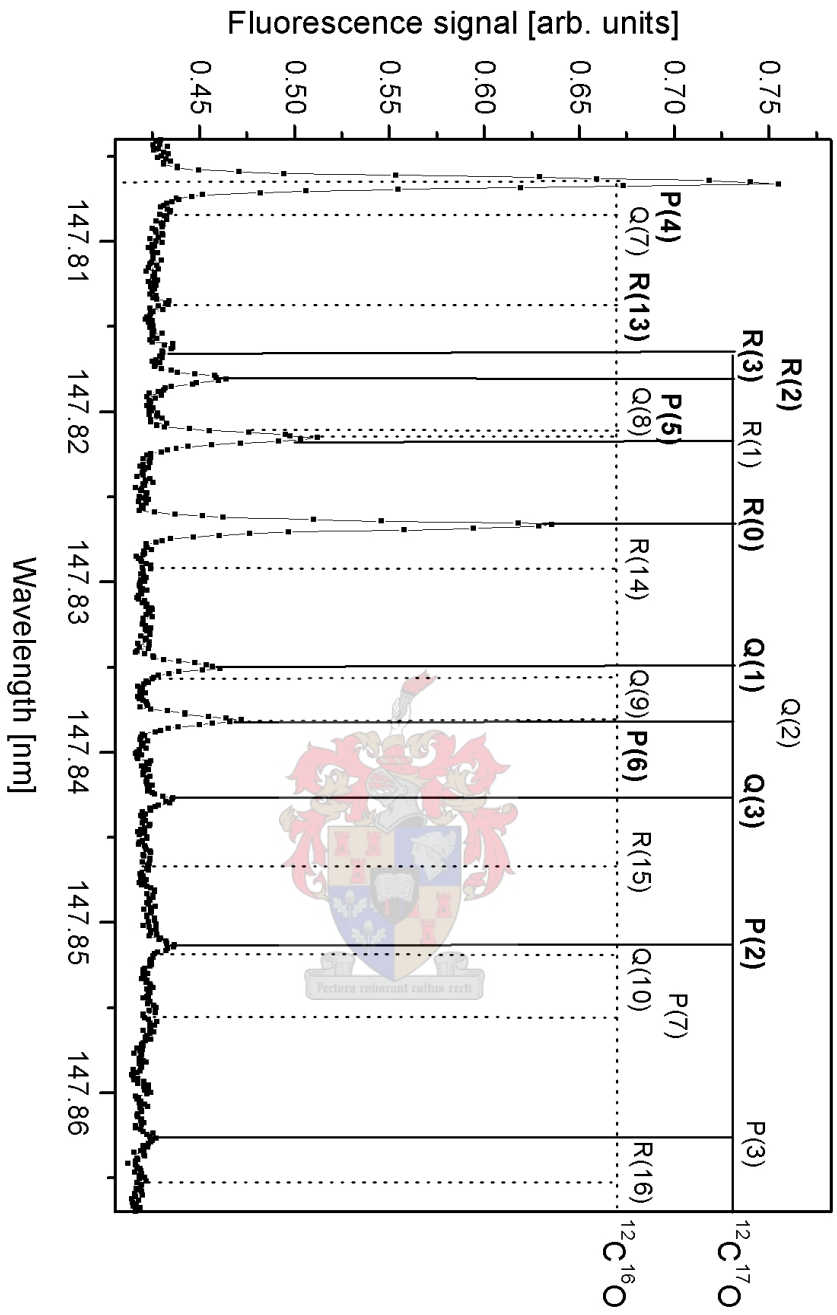

Figure 8-8: Experimental LIF spectrum of the $A^1\Pi(v' = 2)-X^1\Sigma^+(v'' = 0)$ band, indicating the region of $^{12}C^{17}O$ lines (solid lines) and the positions of expected $^{12}C^{16}O$ lines (dotted lines).

8.1.5 $\mathbf{A}^1\Pi(v'=1)-\mathbf{X}^1\Sigma^+(v''=0)$

The LIF and absorption spectra of the $A^1\Pi(v'=1)-X^1\Sigma^+(v''=0)$ band are shown in Figure 8-9. The assigned lines of $^{12}C^{16}O$ and $^{13}C^{16}O$ having $J \leq 6$ are labelled, and the R(0) lines of $^{12}C^{17}O$ and $^{12}C^{18}O$ are also labelled. The lines of the rare $^{12}C^{17}O$ lines of interest have small signals and are found between these lines due to the smaller spacing between band origins of the different isotopomers, and cannot be identified on this scale. These lines are better visible in the detailed graph in Figure 8-10. Besides the lines of this band, a number of $^{12}C^{16}O$ singlet-triplet lines overlap this band in the region of the $^{13}C^{16}O$ lines. This singlet-triplet band $d^3\Delta(v'=5)-X^1\Sigma^+(v''=0)$ is shown in detail in Section 8.1.8.

This band was measured by continuous scans on four occasions in the wavelength range from $150.95 - 151.08$ nm. The dye laser was operated at wavelengths in the range $504.0 - 506.0$ nm using the grating order 6, with approximately 1 mJ (at 480 nm) on all occasions, obtained using *coumarin 480 dye* in *methanol* as solvent. The experimental conditions on the four occasions were as follows: 4 bar pure CO was expanded in supersonic expansion, the gas pulse duration settings on the different occasions were (i) 0.25 ms and (ii), (iii) and (iv) 0.65 ms, the delay between gas and laser pulses was 0.65 ms throughout, the wavelength step sizes of the non-resonant dye laser were (i) 1.5 pm (ii) 1 pm (iii) 1 pm (iv) 1.5 pm, the repetition rate was 5 Hz, data averaging of each point was done over 10 laser shots, and the absorption spectrum was measured with wavelength separation in (i) and not on the other occasions.

The LIF spectrum presented in Figure 8-9 refers to the experimental conditions (iii) above, and exhibited *cold* spectral characteristics. This results in a smaller number of lines and therefore less overlapping in general. However, the closer spacing of the band origins and the overlapping of singlet-triplet lines makes the assignment of lines difficult. The lines of $^{12}C^{16}O$ and $^{13}C^{16}O$ have a higher intensity (of equal intensity in this experiment), which makes the analysis slightly simpler.

The absorption spectrum shows many higher-J lines of $^{12}C^{16}O$ which are not visible in fluorescence, as in other bands. One unidentified absorption line was observed at 151.0597 nm, but this is found in the overlapping region of $^{12}C^{16}O$, $^{13}C^{16}O$, $^{12}C^{17}O$, $^{12}C^{18}O$ and singlet-triplet lines.

A detailed graph of the LIF spectrum of the $A^1\Pi(v'=1)-X^1\Sigma^+(v''=0)$ band, showing

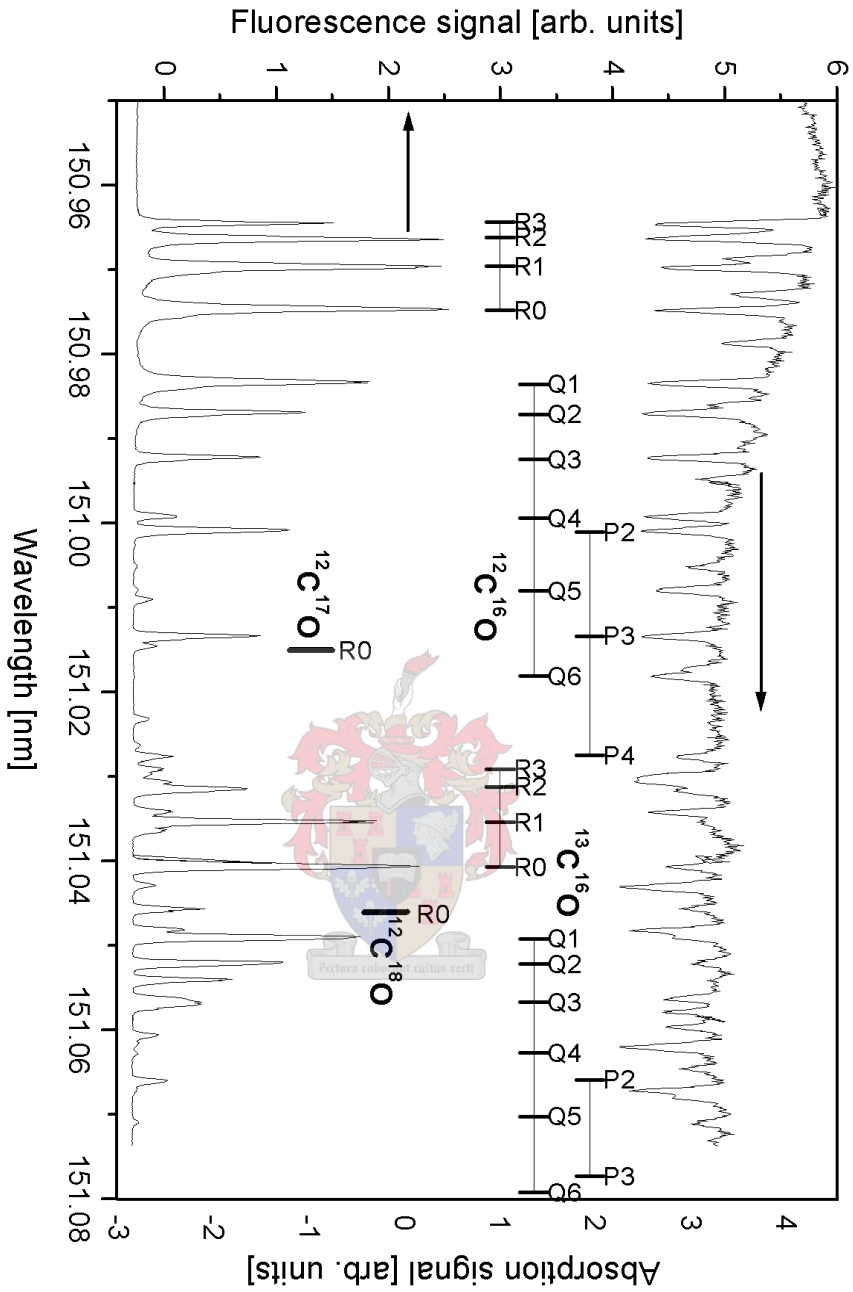

Figure 8-9: Experimental LIF (lower) and absorption (upper) spectra of the $A^1\Pi(v' = 1)-X^1\Sigma^+(v'' = 0)$ band, with the positions of the lowest-J lines of $^{12}C^{16}O$ and $^{13}C^{16}O$ indicated, as well as R(0) of $^{12}C^{17}O$ and $^{12}C^{18}O$.

specifically the region of $^{12}C^{17}O$ lines, is found in Figure 8-10. In the spectrum shown here, five lines of $^{12}C^{17}O$ were detected, as indicated: R(2), R(1), R(0), Q(1), Q(2). The expected line positions of the $^{12}C^{16}O$ and $^{13}C^{16}O$ lines in this wavelength region are indicated. Overlapping of the $^{12}C^{16}O$ and $^{12}C^{17}O$ lines do not occur for the five lines identified here. The peak on the left flank of the R(2) line of $^{13}C^{16}O$ (indicated by an asterisk) is an expected position for all of the following: $^{12}C^{16}O$ R(13), $^{12}C^{17}O$ Q(3) and the $^{S}R(1)$ line of the $d^3\Delta(v' = 5)-X^1\Sigma^+(v'' = 0)$ singlet-triplet band. This line could be due to the contributions of all of these, but an assignment is not made for this line.

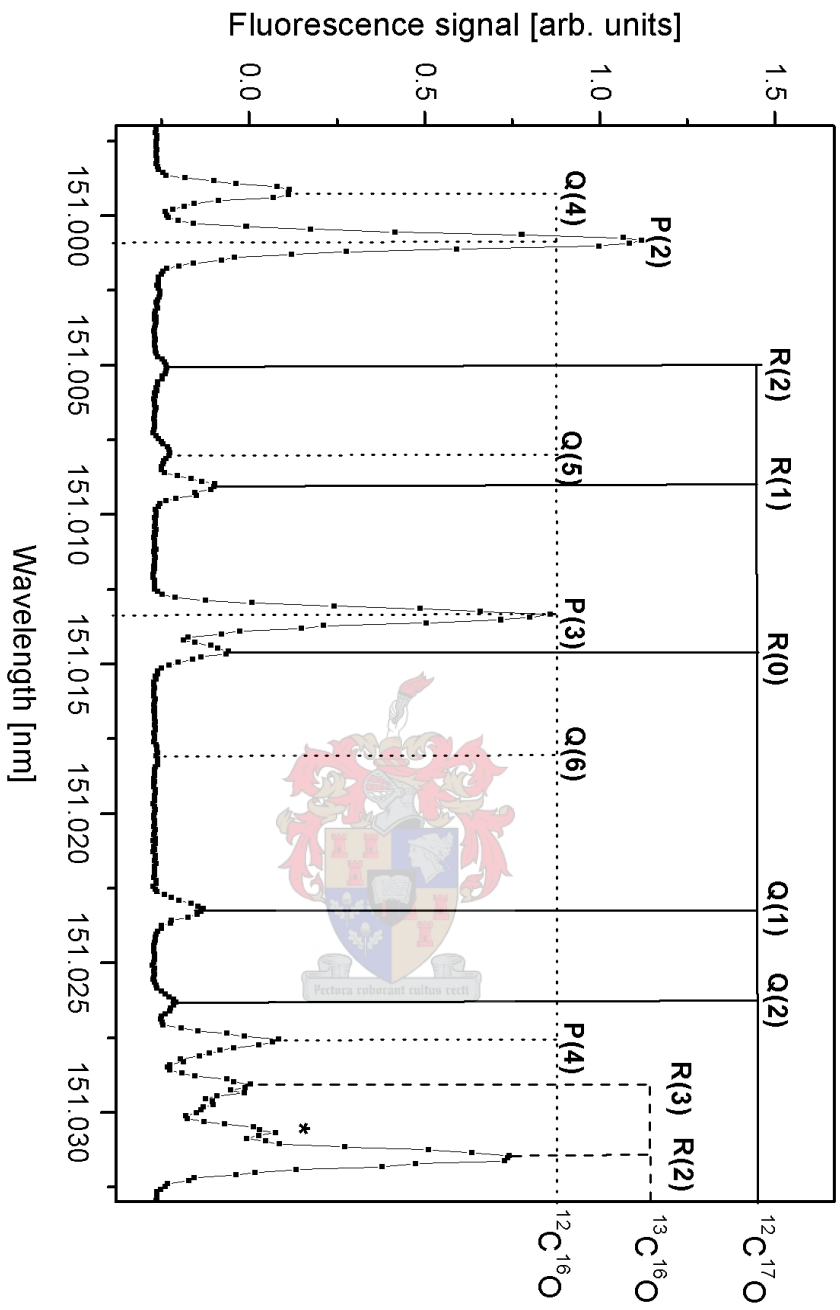

Figure 8-10: Experimental LIF spectrum of the $A^1\Pi(v' = 1)-X^1\Sigma^+(v'' = 0)$ band, indicating the region of $^{12}C^{17}O$ lines (solid lines) and the positions of expected $^{12}C^{16}O$ lines (dotted lines), and some $^{13}C^{16}O$ lines (dashed lines). The line indicated with an asterisk comprises overlapping of the lines of various species.

8.1.6 $\mathbf{A}^1\Pi(v'=0)-\mathbf{X}^1\Sigma^+(v''=0)$

The LIF and absorption spectra of the $A^1\Pi(v'=0)-X^1\Sigma^+(v''=0)$ band are shown in Figure 8-11. The assigned lines of $^{12}C^{16}O$ and $^{13}C^{16}O$ having $J \leq 6$ are labelled, and the R(0) lines of $^{12}C^{17}O$ and $^{12}C^{18}O$ are also labelled. In this band the $^{13}C^{16}O$ lines are found towards shorter wavelengths than the $^{12}C^{16}O$ lines. The lines of the rare $^{12}C^{17}O$ lines of interest, which lie between the $^{12}C^{16}O$ and $^{13}C^{16}O$ lines, have small signals and significant overlapping occurs. A detailed LIF graph of this region is shown in Figure 8-6.

This band was measured by continuous scans on two occasions in the wavelength range from $154.41 - 154.49$ nm. The dye laser was operated at wavelengths in the range $545.1 - 546.26$ nm using the grating order 5, with approximately 0.8 mJ (at 540 nm) on one occasion and approximately 1.5 mJ on the other occasion, obtained using *coumarin 540A dye* in *methanol* as solvent. The experimental conditions on the two occasions were as follows: 4 bar pure CO was expanded in supersonic expansion, the gas pulse duration settings were (i) 0.25 ms and (ii) 0.65 ms, the delays between gas and laser pulses were 0.65 ms in both cases, the wavelength step sizes of the non-resonant dye laser were (i) 1.5 pm and (ii) 1 pm, the repetition rates were (i) 10 Hz and (ii) 5 Hz, data averaging of each point was done over 10 laser shots, and the absorption spectrum was measured with wavelength separation in (i) and without separation on the other occasion.

The LIF spectrum presented in Figure 8-11 refers to the experimental conditions (i) above, and exhibited *hot* spectral characteristics. The close spacing of the band origins, combined with the *hot* characteristics of the spectrum made line assignment a challenge. The lines of $^{12}C^{16}O$ and $^{13}C^{16}O$ have a higher intensity which simplifies the analysis slightly.

The absorption spectrum shows a number of higher-J lines of $^{12}C^{16}O$ which are not visible in fluorescence, as in other bands.

A detailed graph of the LIF spectrum of the $A^1\Pi(v'=0)-X^1\Sigma^+(v''=0)$ band, showing specifically the region of $^{12}C^{17}O$ lines, is found in Figure 8-12. In the spectrum shown here, only one line of $^{12}C^{17}O$ could be detected, as indicated: R(0). This is due to significant overlapping with the $^{12}C^{16}O$, $^{13}C^{16}O$ and $^{12}C^{18}O$ lines in the vicinity, which are indicated. In order to simplify the figure, all positions of expected $^{12}C^{17}O$ lines are not included here. All other lines have higher peak intensity and were identified to belong to other isotopomers, as indicated.

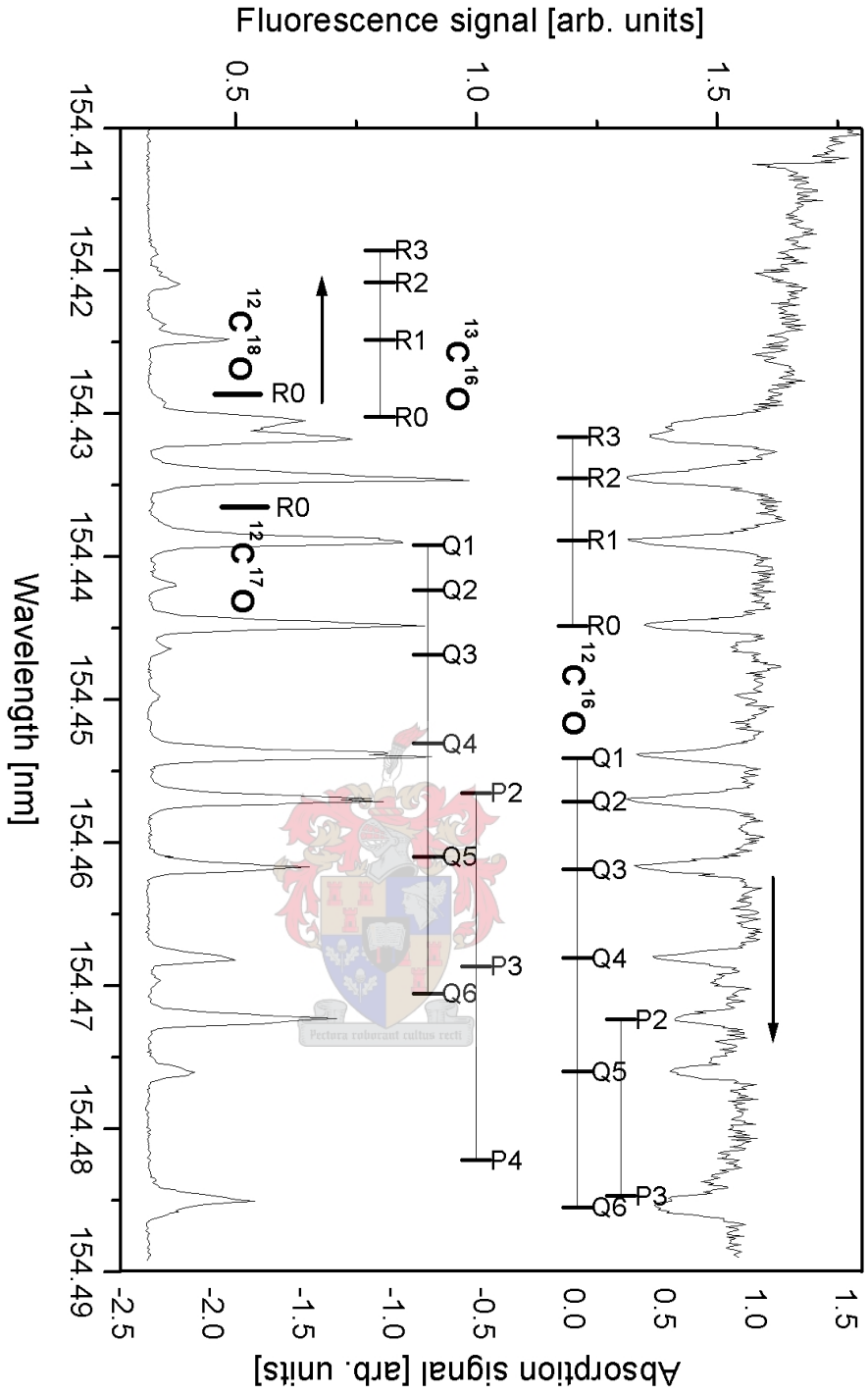

Figure 8-11: Experimental LIF (lower) and absorption (upper) spectra of the $A^1\Pi(v' = 0)-X^1\Sigma^+(v'' = 0)$ band, with the positions of the lowest-J lines of $^{12}C^{16}O$ and $^{13}C^{16}O$ indicated, as well as R(0) of $^{12}C^{17}O$ and $^{12}C^{18}O$.

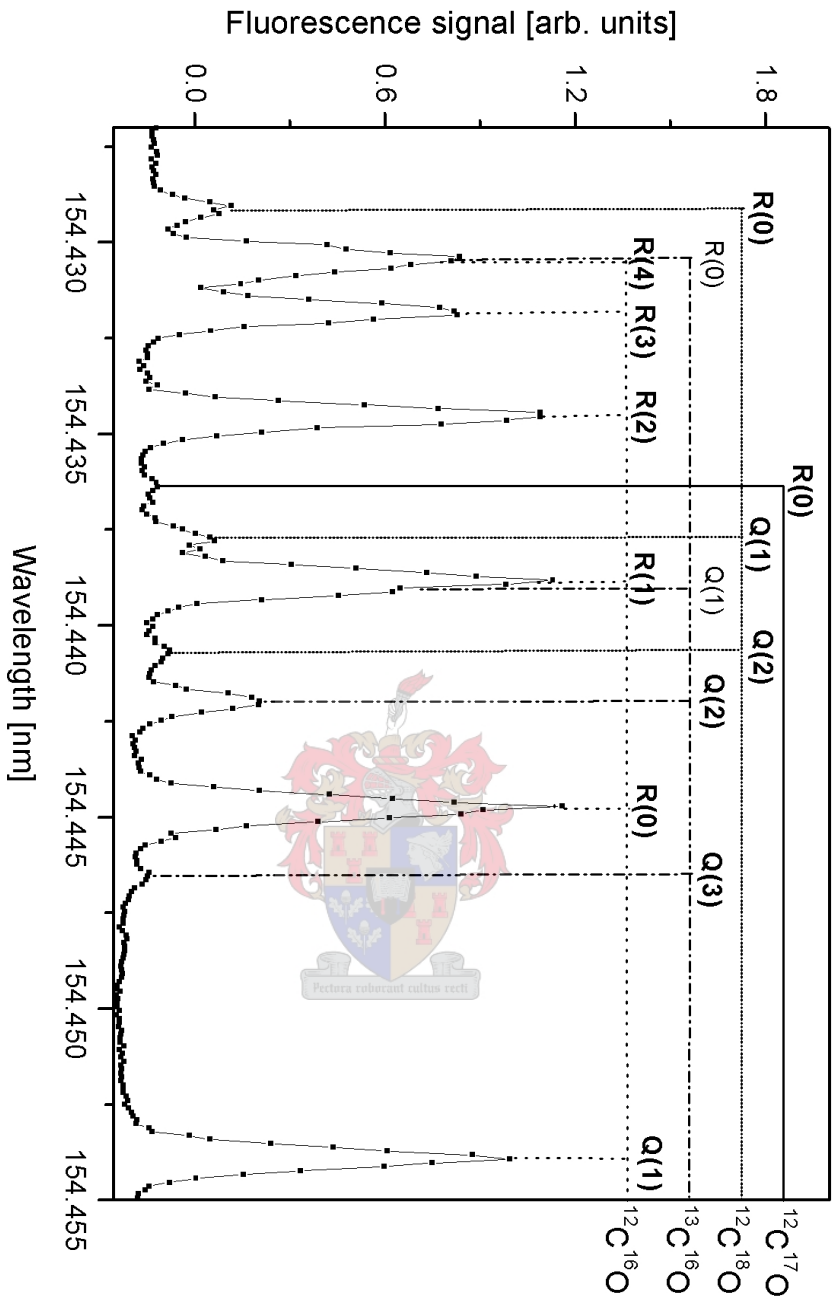

Figure 8-12: Experimental LIF spectrum of the $A^1\Pi(v' = 0)$–$X^1\Sigma^+(v'' = 0)$ band, indicating the region of $^{12}C^{17}O$ lines (solid lines) and the positions of expected $^{12}C^{16}O$ (dotted), $^{13}C^{16}O$ (dash-dotted) and $^{12}C^{18}O$ (dashed) lines.

8.1.7 $\mathbf{e}^3\Sigma^-(v'=1)-\mathbf{X}^1\Sigma^+(v''=0)$

This band was recorded to the short wavelength side of the $A^1\Pi(v'=0)-X^1\Sigma^+(v''=0)$ band and is shown in detail in Figure 8-13. This figure shows all 10 identified lines with the labelling scheme adopted from [9]. The experimental conditions are identical to those of the description (i) for the $A^1\Pi(v'=0)-X^1\Sigma^+(v''=0)$ band measurement (since this is the same measurement).

All 10 identified lines of this band could be compared to the literature wavelengths, and this is shown in Figure 8-14. The average deviation between the experimental and literature wavelengths of 0.3 pm is comparable to the estimated calibration accuracy of ±0.2 pm. The slightly larger deviation and the systematic nature of this difference, as visible in the figure, indicates a possible minor error in the calibration or the literature wavelengths.

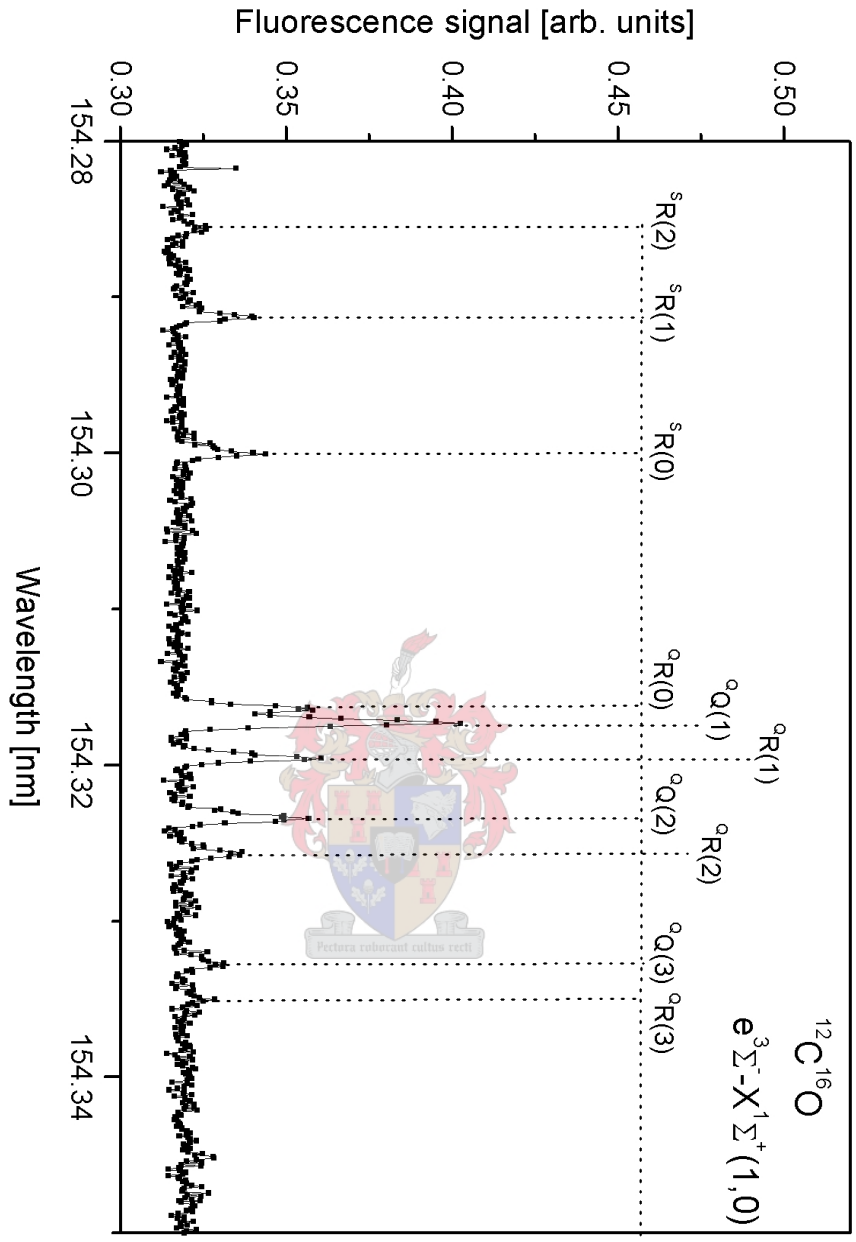

Figure 8-13: Experimental LIF spectrum of the $e^3\Sigma^-(v' = 1)$–$X^1\Sigma^+(v'' = 0)$ band, with the positions of all identified lines indicated.

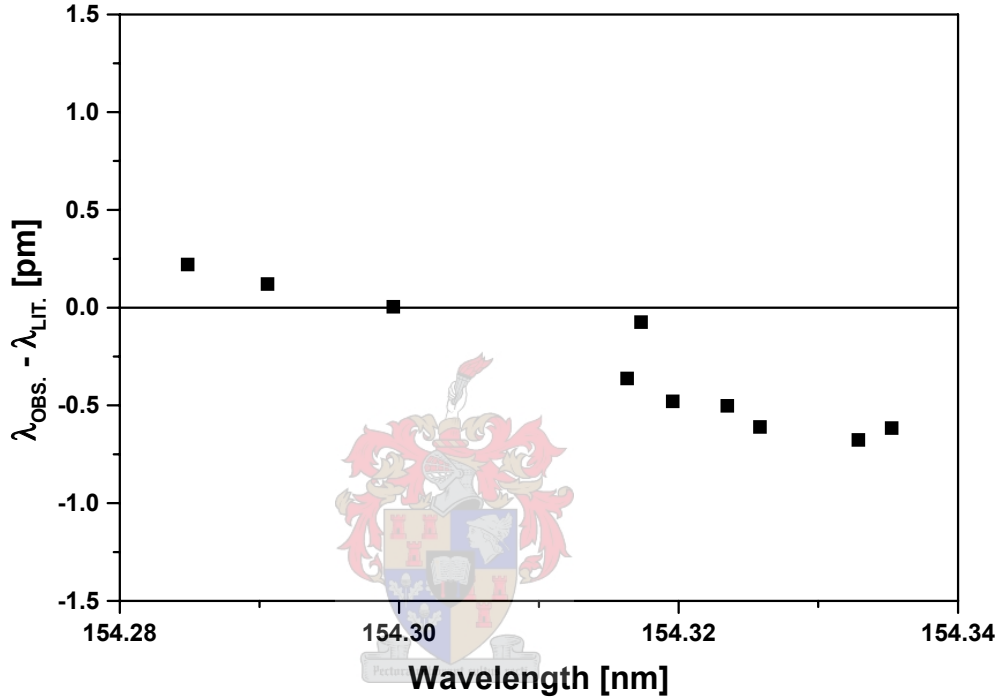

Figure 8-14: Difference between experimental (λ_{OBS}) and literature wavelengths (λ_{LIT}) of 10 identified lines of the $e^3\Sigma^-(v'=1)-X^1\Sigma^+(v''=0)$ band.

8.1.8 $\mathbf{d}^3\Delta(v'=5)-\mathbf{X}^1\Sigma^+(v''=0)$

This band was recorded between the $^{13}C^{16}O$ lines of the $A^1\Pi(v'=1)-X^1\Sigma^+(v''=0)$ band and is shown in detail in Figure 8-15. This figure shows all 12 identified lines, of which nine are new results, with the labelling scheme adopted from [9]. In this measurement the R(0) line of $^{13}C^{16}O$ is also identified. The experimental conditions are identical to those of the description (iv) for the $A^1\Pi(v'=1)-X^1\Sigma^+(v''=0)$ band measurement, which is also used for calibration purposes. This particular measurement (a separate continuous scan) was made using a modified gate setting to selectively enhance the singlet-triplet lines and discriminate against the singlet-singlet lines.

The three lines detected that are documented in the literature could be compared to these literature values. This comparison is shown in Figure 8-16. The average deviation between the experimental and literature wavelengths of 0.7 pm is larger than the calibration error margin and indicates possible error in either the literature wavelength or the observed wavelength for the $^{Q}P(4)$ line.

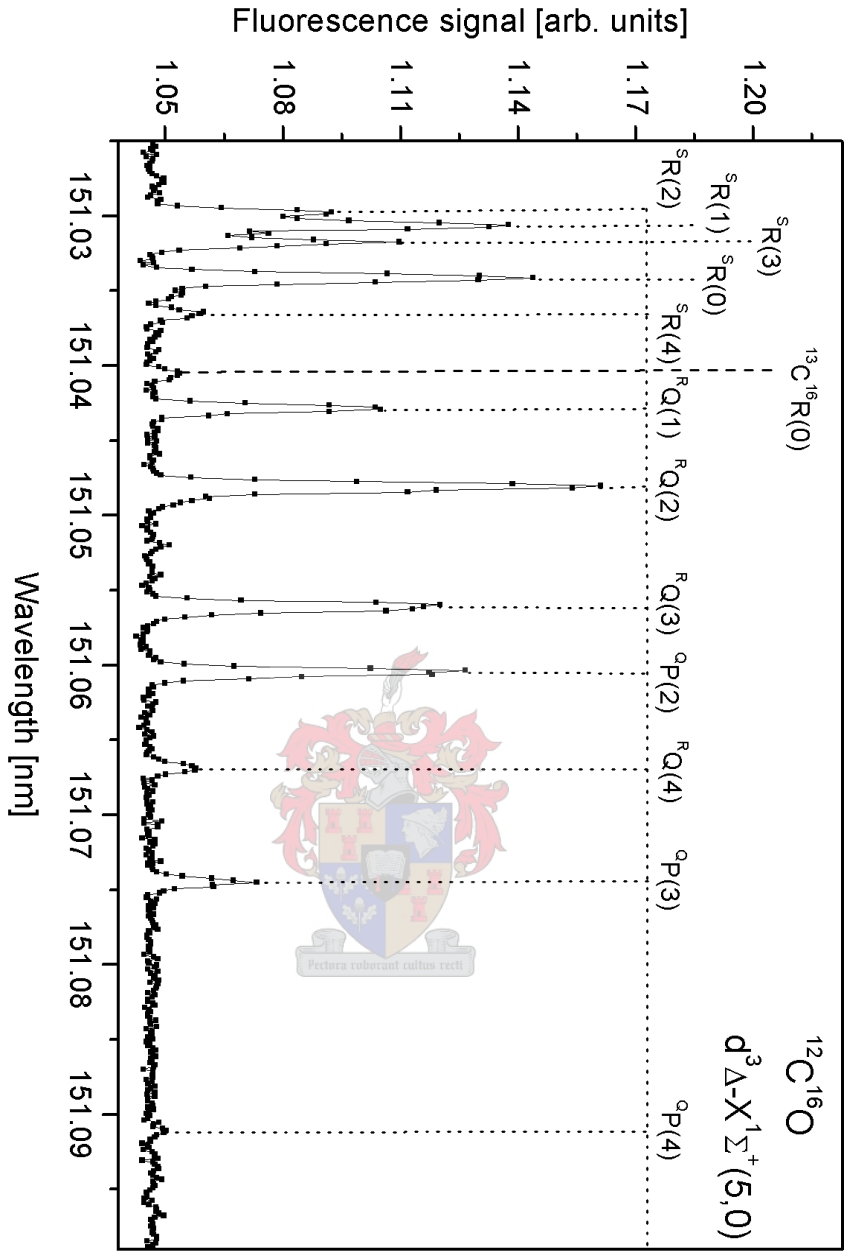

Figure 8-15: Experimental LIF spectrum of the $d^3\Delta(v' = 5)$–$X^1\Sigma^+(v'' = 0)$ band, with the positions of all identified lines indicated.

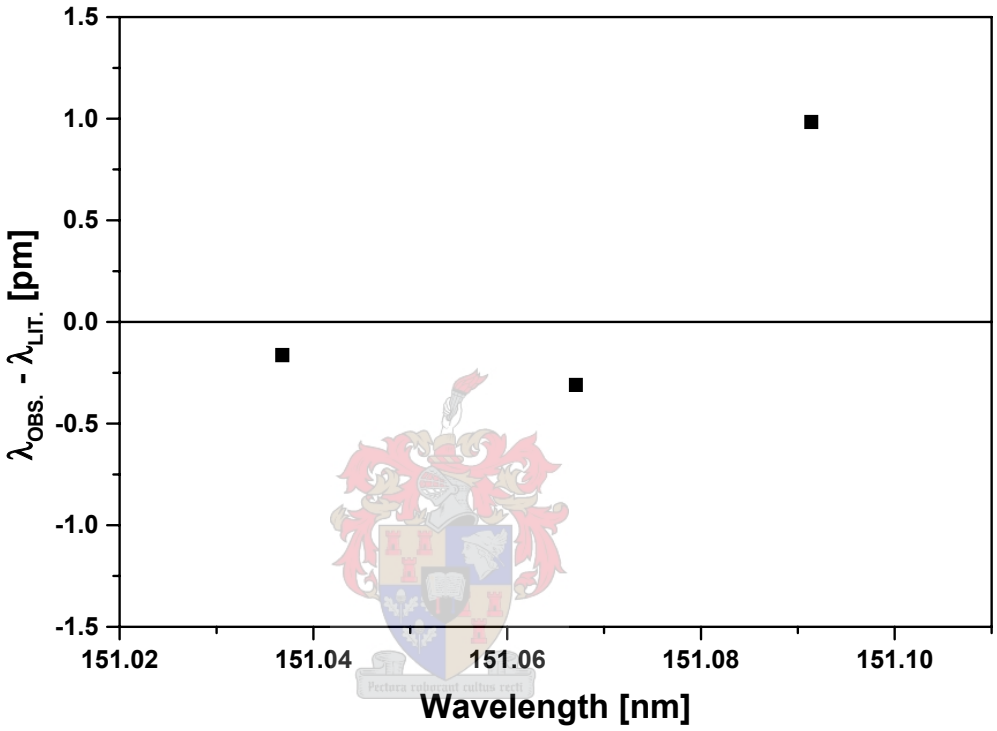

Figure 8-16: Difference between experimental (λ_{OBS}) and literature wavelengths (λ_{LIT}) of three identified lines of the $\mathrm{d}^3\Delta(v' = 5)$–$\mathrm{X}^1\Sigma^+(v'' = 0)$ band.

8.1.9 $\mathbf{a'}^3\Sigma^+(v'=14)-\mathbf{X}^1\Sigma^+(v''=0)$

This band was recorded between the $^{12}C^{16}O$ lines of the $A^1\Pi(v'=4)-X^1\Sigma^+(v''=0)$ band and is shown in detail in Figure 8-17. This figure shows all 10 identified lines, of which one has not been experimentally measured before (two have recently been added to the database [31]), with the labelling scheme adopted from [9]. The experimental conditions are identical to those of the description for the $A^1\Pi(v'=4)-X^1\Sigma^+(v''=0)$ band measurement, which is also used for calibration purposes. This particular measurement (a separate continuous scan) was done using a modified gate setting to selectively enhance the singlet-triplet lines and discriminate against the singlet-singlet lines.

The seven lines detected that are also documented in the paper [30] could be compared to these literature values. This comparison is shown in Figure 8-18. The average deviation between the experimental and literature wavelengths of 0.4 pm is comparable to the estimated calibration accuracy of ± 0.2 pm. The slightly larger deviation and the systematic nature of this difference, as visible in the figure, indicates a possible minor error in the calibration or the literature wavelengths.

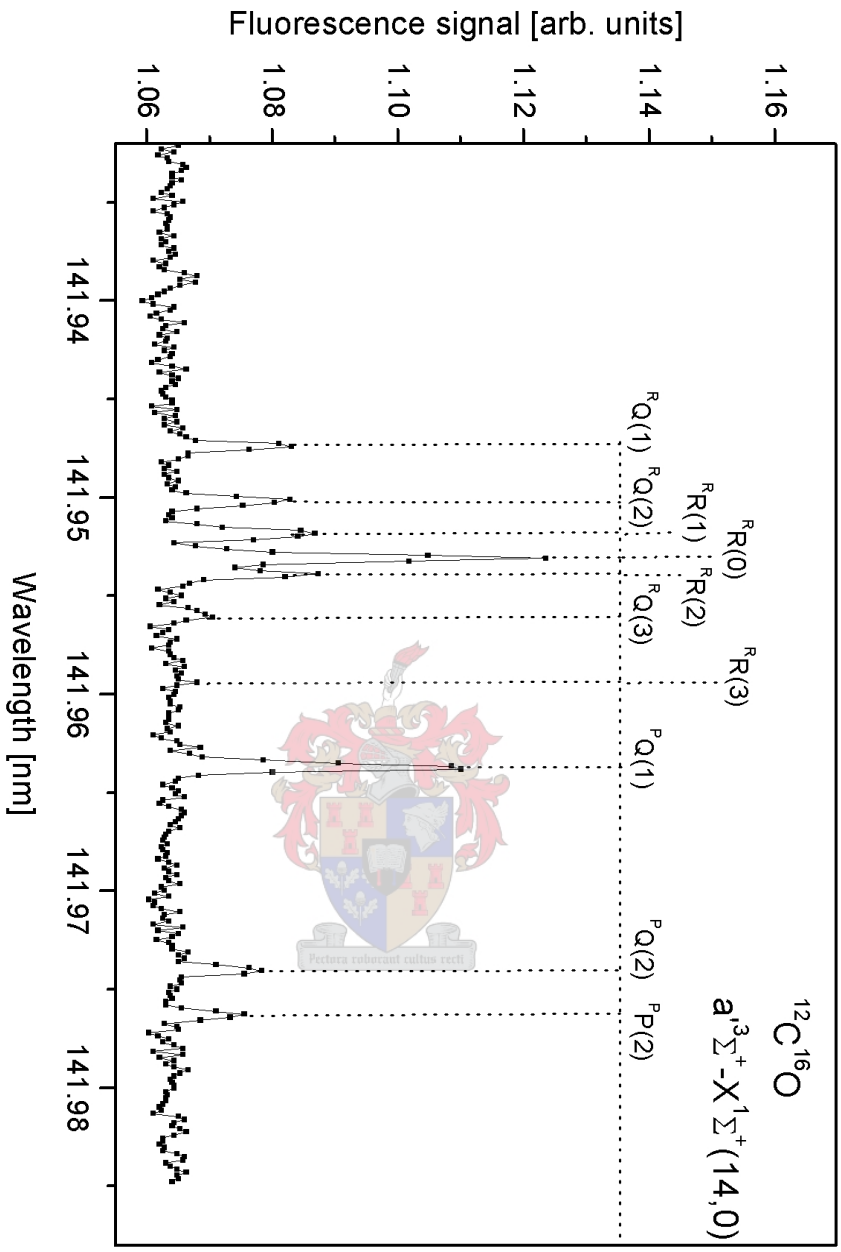

Figure 8-17: Experimental LIF spectrum of the $a'^3\Sigma^+(v' = 14) - X^1\Sigma^+(v'' = 0)$ band, with the positions of all identified lines indicated.

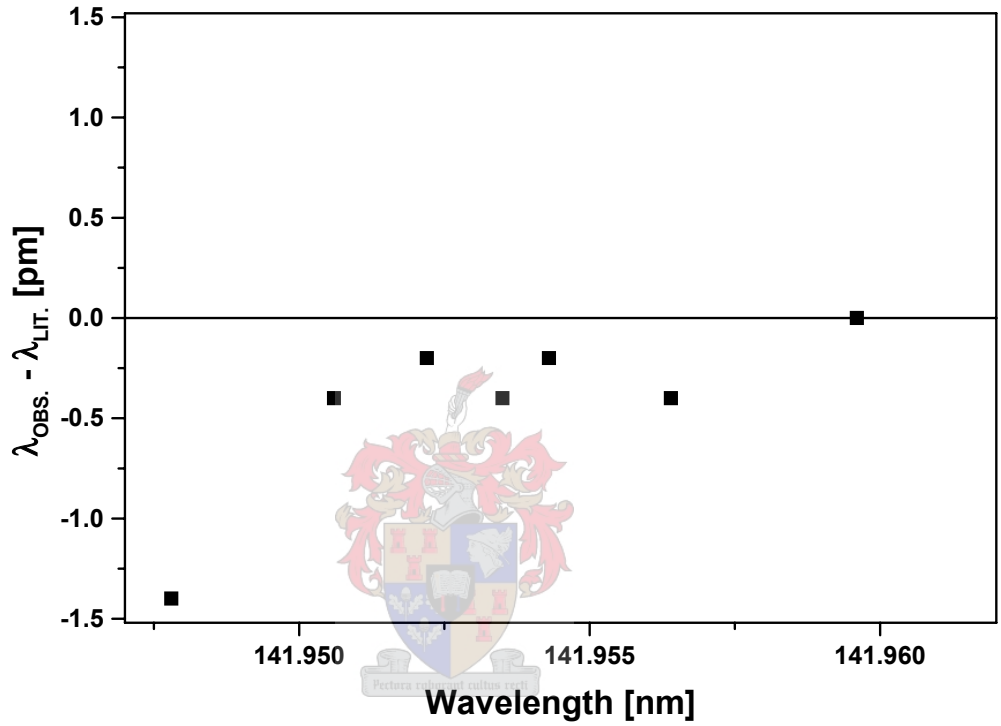

Figure 8-18: Difference between experimental (λ_{OBS}) and literature wavelengths (λ_{LIT}) of seven identified lines of the $a'^3\Sigma^+(v'=14)-X^1\Sigma^+(v''=0)$ band.

8.2 Appendix B: Band origins

Band origins (the positions of the forbidden Q(0) lines) were determined for all four isotopomers in all six vibronic bands measured (of the Fourth Positive System, i.e. excluding singlet-triplet bands). The theoretical position of the band origin relative to the neighbouring R(0) and Q(1) lines was calculated, and the resulting ratio was used to interpolate the position of the band origin from experimental data of the R(0) and Q(1) lines. The resulting band origins are presented in Table 8.1. The asterisk indicates a slight variation in the determination of the band origin, since the Q(1) lines could not be identified in either of these cases. An assumption was made as to the wavelength of this line, according to the expected position from calculations.

Table 8.1:
Band origins determined experimentally, of the four most abundant isotopomers of CO, in the lowest six vibronic bands of the Fourth Positive System. All values are given in nm.

Band label	$^{12}C^{16}O$	$^{13}C^{16}O$	$^{12}C^{18}O$	$^{12}C^{17}O$
$(5,0)$	139.2583	139.5286	139.5512	139.4122
$(4,0)$	141.9105	142.1398	142.1587	142.0416
$(3,0)$	144.7417	144.9207	144.9359	144.8438
$(2,0)$	147.7632	147.8859	147.8960	147.8334
$(1,0)$	150.9819	151.0477	151.0525	151.0217
$(0,0)$	154.4525	154.4377	*154.4365	*154.4438

Vibrational isotopic shifts of the band origins of the rarer isotopomers relative to those of $^{12}C^{16}O$ were calculated from the data above and are included in Table 8.2. This is a reproduction of Table 5.2 from Chapter 5, but is included here for easy reference.

Table 8.2:
Calculated theoretical and observed experimental vibrational isotopic shifts of the band origins relative to $^{12}C^{16}O$. All values are given in cm^{-1}.

	Vibrational isotopic shift relative to $^{12}C^{16}O$ [cm^{-1}]					
Band label	**$^{13}C^{16}O$**		**$^{12}C^{18}O$**		**$^{12}C^{17}O$**	
	Theory	Experiment	Theory	Experiment	Theory	Experiment
$(5,0)$	138.5	139.1	150.2	150.7	79.0	79.3
$(4,0)$	112.3	113.7	121.8	123.0	64.1	65.0
$(3,0)$	84.7	85.3	91.9	92.6	48.3	48.7
$(2,0)$	55.5	56.2	60.2	60.8	31.7	32.1
$(1,0)$	24.9	28.9	27.0	31.0	14.2	17.5
$(0,0)$	-7.3	-6.2	-7.9	-6.7	-4.2	-3.6

8.3 Appendix C: Detailed tables of results

Detailed tables of results are included here for reference purposes. The results in this appendix have been used to find averaged values for the rovibronic transitions of interest, as presented in Chapter 5. These tables include results from each experimental spectrum analysed. The detailed descriptions of these experimental conditions are found in Appendix 8.1. The number of spectra used for finding an averaged value for a given line is included, as some lines were not identified in all measured spectra due to overlapping and/or low signal-to-noise ratios. The data are presented, with an additional insignificant digit for eliminating possible rounding errors when using the data in future calculations. These tables are not numbered as they are not referenced directly in this dissertation. Error margins of all six vibronic bands are estimated from the calibration accuracy as ± 0.2 pm, as shown in Section 5.2.2. The error margin is slightly larger for the singlet-triplet bands as indicated in Figures 8-14 (0.3 pm), 8-16 (0.7 pm), and 8-18 (0.4 pm).

8.3.1 $\mathbf{A}^1\Pi(v'=5)-\mathbf{X}^1\Sigma^+(v''=0)$

$^{12}C^{17}O$

	Experimental wavelengths [nm]			
Line label	Hot lines	Cold lines	Average	# of lines
R(1)	-	139.4026(8)	139.4027	1
R(0)	-	139.4066(1)	139.4066	1
Q(1)	-	139.4137(8)	139.4138	1
Q(2)	-	139.4171(3)	139.4171	1

$^{12}C^{18}O$

	Experimental wavelengths [nm]			
Line label	Hot lines	Cold lines	Average	# of lines
R(2)	-	139.5394(7)	139.5395	1
R(1)	-	139.5417(9)	139.5418	1
R(0)	-	139.5456(9)	139.5457	1
Q(1)	-	139.5528(4)	139.5528	1
Q(2)	-	139.5560(0)	139.5560	1
Q(3)	-	139.5607(6)	139.5608	1
P(2)	-	139.5670(1)	139.5670	1
P(3)	-	139.5770(1)	139.5770	1

8.3.2 $\mathbf{A}^1\Pi(v'=4)-\mathbf{X}^1\Sigma^+(v''=0)$

$^{12}C^{17}O$

	Experimental wavelengths [nm]			
Line label	Hot lines	Cold lines	Average	# of lines
R(3)	-	142.0273(9)	142.0274	1
R(2)	-	142.0285(4)	142.0285	1
R(1)	-	142.0312(4)	142.0312	1
R(0)	-	142.0356(0)	142.0356	1
Q(1)	-	142.0432(6)	142.0433	1
Q(2)	-	142.0465(2)	142.0465	1
Q(3)	-	142.0514(1)	142.0514	1

$^{12}C^{18}O$

	Experimental wavelengths [nm]			
Line label	Hot lines	Cold lines	Average	# of lines
R(2)	-	142.1459(6)	142.1460	1
R(1)	-	142.1486(5)	142.1486	1
R(0)	-	142.1528(6)	142.1529	1
Q(1)	-	142.1603(0)	142.1603	1
Q(2)	-	142.1634(6)	142.1635	1
Q(3)	-	142.1682(7)	142.1683	1
P(2)	-	142.1753(2)	142.1753	1

8.3.3 $\mathbf{A}^1\Pi(v'=3)-\mathbf{X}^1\Sigma^+(v''=0)$

$^{12}C^{17}O$

	Experimental wavelengths [nm]			
Line label	Hot lines	Cold lines	Average	# of lines
R(3)	144.8280(7)	1. - 3. - 2. 144.8283(3) 4. -	144.8282	2
R(2)	144.8297(0)	1. - 3. - 2. 144.8299(2) 4. -	144.8298	2
R(1)	-	1. - 3. 144.8327(7)[2] 2. - 4. -	144.8328	1
R(0)	144.8375(9)	1. 144.8374(3) 3. 144.8376(4) 2. 144.8377(1) 4. 144.8375(7)	144.8376	5
Q(1)	144.8454(0)	1. 144.8453(0) 3. 144.8454(6) 2. 144.8456(1) 4. 144.8454(6)	144.8454	5
Q(2)	-	1. - 3. 144.8485(7) 2. - 4. -	144.8486	1
Q(3)	-	1. 144.8532[3] 3. - 2. - 4. -	144.8532	1
Q(4)	144.8596(9)	-	144.8597	1
P(2)	144.8610(1)	-	144.8610	1

[2]This line was newly identified in the reinvestigation process, from previously recorded spectra.

[3]This data taken from Steinmann et al [10]. It could not be identified in the reinvestigation process, due mainly to a very low signal-to-noise ratio.

$^{12}C^{18}O$

	Experimental wavelengths [nm]			
Line label	Hot lines	Cold lines	Average	# of lines
R(3)	-	1. - 3. - 2. 144.9204(0)[4] 4. -	144.9204	1
R(1)	144.9248(8)	1. 144.9248(6) 3. 144.9250(1) 2. 144.9251(0) 4. 144.9251(0)	144.9250	5
R(0)	144.9294(6)	1. 144.9295(6) 3. 144.9295(9) 2. 144.9297(8) 4. 144.9297(5)	144.9296	5
Q(1)	-	1. 144.9374(1) 3. 144.9374(5) 2. 144.9375(9) 4. 144.9375(6)	144.9375	4
Q(2)	144.9402(9)	1. 144.9406(2) 3. 144.9404(8) 2. 144.9405(7) 4. 144.9406(1)	144.9405	5
Q(3)	144.9450(4)	-	144.9450	1
Q(4)	144.9513(5)	-	144.9514	1
P(2)	144.9527(4)	-	144.9527	1

[4]This line was newly identified in the reinvestigation process, from previously recorded spectra.

8.3.4 $\mathbf{A}^1\Pi(v'=2)-\mathbf{X}^1\Sigma^+(v''=0)$

^{12}C^{17}O

	Experimental wavelengths [nm]			
Line label	Hot lines	Cold lines	Average	# of lines
R(3)	147.8161(1)	1. 147.8163(2) 2. 147.8162(2)	147.8162	3
R(2)	147.8182(0)	1. 147.8181(2) 2. 147.8181(3)	147.8181	3
R(0)	147.8267(9)	1. 147.8266(9) 2. 147.8267(8)	147.8268	3
Q(1)	-	1. 147.8350(8) 2. 147.8349(8)	147.8350	2
Q(3)	147.8429(9)	1. 147.8428(9) 2. -	147.8429	2
Q(4)	147.8489(5)	-	147.8490	1
P(2)	-	1. 147.8513(5) 2. -	147.8514	1
P(3)	147.8628(2)	-	147.8628	1

$^{12}C^{18}O$

	Experimental wavelengths [nm]			
Line label	Hot lines	Cold lines	Average	# of lines
R(2)	147.8810(8)	1. 147.8811(9) 2. 147.8811(1)	147.8811	3
R(1)	147.8845(6)	1. 147.8845(6) 2. 147.8844(6)	147.8845	3
R(0)	147.8895(6)	1. 147.8895(0) 2. 147.8894(8)	147.8895	3
Q(1)	147.8973(8)	1. 147.8975(6) 2. 147.8974(2)	147.8975	3
Q(2)	147.9005(0)	1. 147.9005(8) 2. 147.9004(9)	147.9005	3
Q(3)	147.9050(5)	1. 147.9052(0) 2. -	147.9051	2
Q(4)	147.9111(4)	-	147.9111	1
P(2)	147.9136(4)	1. - 2. 147.9136(0)	147.9136	2
P(3)	147.9247(9)	-	147.9248	1
P(4)	147.9374(7)	-	147.9375	1
P(5)	147.9514(9)	-	147.9515	1

8.3.5 $\mathbf{A}^1\Pi(v'=1)-\mathbf{X}^1\Sigma^+(v''=0)$

^{12}C^{17}O

	Experimental wavelengths [nm]			
Line label	Hot lines	Cold lines	Average	# of lines
R(3)	151.0031(3)	1. - 2. - 3. 151.0028(3)	151.0030	2
R(2)	-	1. - 2. 151.0050(7) 3. 151.0053(3)	151.0052	2
R(1)	151.0093(3)	1. 151.0090(4) 2. 151.0090(7) 3. 151.0092(1)	151.0092	4
R(0)	151.0147(1)	1. 151.0145(9) 2. 151.0145(6) 3. 151.0146(4)	151.0146	4
Q(1)	151.0232(3)	1. 151.0232(3) 2. 151.0232(4) 3. 151.0232(2)	151.0232	4
Q(2)	-	1. 151.0262(5) 2. 151.0263(1) 3. 151.0263(5)	151.0263	3

$^{12}C^{18}O$

	Experimental wavelengths [nm]			
Line label	Hot lines	Cold lines	Average	# of lines
R(3)[5]	151.0342(4)	1. 151.0340(7) 2. 151.0341(1) 3. 151.0341(1)	151.0341	4
R(2)	151.0365(1)	1. 151.0364(9) 2. 151.0364(2) 3. 151.0364(2)	151.0365	4
R(0)	151.0456(3)	1. 151.0457(6) 2. 151.0457(4) 3. 151.0455(9)	151.0457	4
Q(1)	151.0540(8)	1. 151.0540(7) 2. 151.0540(5) 3. 151.0539(9)	151.0540	4
Q(2)	-	1. - 2. 151.0569(9) 3. -	151.0570	1
Q(3)	-	1. - 2. 151.0616(3) 3. 151.0615(1)	151.0616	2
Q(4)	151.0669(4)	1. - 2. 151.0671(0) 3. -	151.0670	2
Q(5)	151.0745(5)	-	151.0745	1
P(2)	147.9247(9)	1. 151.0708(4) 2. 151.0709(9) 3. 151.0706(7)	151.0708	4

[5] This line was observed to have strong triplet character, which indicates possible overlap and a subsequent larger error margin.

8.3.6 $\mathbf{A}^1\Pi(v'=0)-\mathbf{X}^1\Sigma^+(v''=0)$

$^{12}C^{17}O$

	Experimental wavelengths [nm]			
Line label	Hot lines	Cold lines	Average	# of lines
R(0)	154.4362(8)	154.4363(6)	154.4363	2

$^{12}C^{18}O$

	Experimental wavelengths [nm]			
Line label	Hot lines	Cold lines	Average	# of lines
R(2)	154.4201(1)	154.4197(9)	154.4200	2
R(1)	154.4237(5)	154.4237(4)	154.4237	2
R(0)	154.4292(3)	154.4291(1)	154.4292	2
Q(2)	-	154.4406(7)	154.4407	1
Q(4)	154.4516(8)	-	154.4517	1

8.3.7 $\mathbf{e}^3\Sigma^-(v'=1)-\mathbf{X}^1\Sigma^+(v''=0)$

Line label	Experimental wavelength [nm]
$^QR(0)$	154.3163(9)
$^QR(1)$	154.3196(0)
$^QR(2)$	154.3256(9)
$^QR(3)$	154.3350(4)
$^SR(0)$	154.3000(1)
$^SR(1)$	154.2912(5)
$^SR(2)$	154.2855(9)
$^QQ(1)$	154.3173(1)
$^QQ(2)$	154.3234(4)
$^QQ(3)$	154.3327(9)

8.3.8 $\mathbf{d}^3\Delta(v'=5)-\mathbf{X}^1\Sigma^+(v''=0)$

Line label	Experimental wavelength [nm]
${}^{S}R(0)$	151.0341(3)
${}^{S}R(1)$	151.0306(3)
${}^{S}R(2)$	151.0297(8)
${}^{S}R(3)$	151.0317(5)
${}^{S}R(4)$	151.0364(8)
${}^{R}Q(1)$	151.0428(8)
${}^{R}Q(2)$	151.0480(4)
${}^{R}Q(3)$	151.0560(8)
${}^{R}Q(4)$	151.0669(0)
${}^{Q}P(2)$	151.0604(5)
${}^{Q}P(3)$	151.0745(2)
${}^{Q}P(4)$	151.0911(4)

8.3.9 $\mathbf{a}'^3\Sigma^+(v'=14)-\mathbf{X}^1\Sigma^+(v''=0)$

Line label	Experimental wavelength [nm]
${}^{R}Q(1)$	141.9473(8)
${}^{R}Q(2)$	141.9501(5)
${}^{R}Q(3)$	141.9560(2)
${}^{R}R(1)$	141.9518(1)
${}^{R}R(0)$	141.9531(0)
${}^{R}R(2)$	141.9538(9)
${}^{R}R(3)$	141.9594(6)
${}^{P}Q(1)$	141.9637(5)
${}^{P}Q(2)$	141.9740(6)
${}^{P}P(2)$	141.9763(1)

Bibliography

[1] C.M. Steinmann (2003). *Vacuum ultraviolet laser spectroscopy of carbon monoxide in a supersonic jet*, PhD Dissertation, University of Stellenbosch, Stellenbosch, South Africa.

[2] E.F. Van Dishoeck, J.H. Black (1988). "The photodissociation and chemistry of interstellar CO", *The Astrophysical Journal* **334**, 771-802.

[3] A.M. Smith, T.P. Stecher (1971). "Carbon monoxide in the Interstellar Spectrum of Zeta Ophiuchi", *The Astrophysical Journal* **164**, L43-L47.

[4] http://www.seds.org/~spider/oaos/oaos.html (5 October 2005). "Orbital Telescopes", Webpage containing list of past, current and future satellite observatories.

[5] D.S. Balser, J.P. McMullin, T.L. Wilson (2002). "CO isotopes in planetary nebulae", *The Astrophysical Journal* **572**, 326-334.

[6] W. Demtroder (2003). *Laser Spectroscopy: Basic concepts and Instrumentation*, Third Edition, Springer, Heidelberg.

[7] C.M. Steinmann (1999). *Development and characterisation of a tunable laser source in the vacuum ultraviolet*, MSc Thesis, University of Stellenbosch, Stellenbosch.

[8] G. Scoles (1988). *Atomic and molecular beam methods Volume 1*, Oxford University Press, New York.

[9] D.C. Morton, L. Noreau (1994). "A Compilation of Electronic Transitions in the CO Molecule and the Interpretation of some Puzzling Interstellar Absorption Features", *The Astrophysical Journal Supplement Series* **95**, 301-343.

[10] C.M. Steinmann, E.G. Rohwer, H. Stafast (2003). "Accurate laboratory wavelengths of the vacuum ultraviolet A(v'=3)-X(v"=0) band of $^{12}C^{17}O$ and $^{12}C^{18}O$", *The Astrophysical Journal* **590**, L123-L126.

[11] C.M. Steenkamp, A. du Plessis, E.G. Rohwer (2005). "An improved experimental setup for high-resolution vacuum ultraviolet laser spectroscopy", *South African Journal of Science* **101**, 272-275.

[12] P.H. Krupenie (1966). "The Band Spectrum of carbon monoxide", *National Standard Reference Data Series - National Bureau of Standards* **5**, Washington D.C.

[13] J.D. Simmons, A.M. Bass, S.G. Tilford (1969). "The Fourth Positive System of carbon monoxide Observed in Absorption at High Resolution in the Vacuum Ultraviolet Region", *The Astrophysical Journal* **155**, 345-358.

[14] S.G. Tilford, J.D. Simmons (1972). "Atlas of the Observed Absorption Spectrum of carbon monoxide Between 1060 and 1900 Å", *Journal of Physical Chemistry Reference Data* **Vol. 1 No. 1**, 147-187.

[15] F.J. Lovas, P.H. Krupenie (1974). "Microwave Spectra of Molecules of Astrophysical Interest VII. Carbon monoxide, Carbon Monosulfide, and Silicon monoxide", *Journal of Physical Chemistry Reference Data* **Vol. 3 No. 1**, 245-257.

[16] R.L. Kurucz (1976). "The Fourth Positive System of Carbon monoxide", *Smithsonian Astrophysical Observatory (SAO) Special Report* **#374**.

[17] I. Borges Jr., P.J.S.B. Caridade, A.J.C. Varandas (2001). "Potential energy curves for $X^1\Sigma^+$ and $A^1\Pi$ states of CO: The $A^1\Pi(v' = 0 - 23) \longleftarrow X^1\Sigma^+(v'' = 0, 1)$ Transitions", *Journal of Molecular Spectroscopy* **209**, 24-29.

[18] Y. Sheffer, D.L. Lambert, S.R. Federman (2002). "Ultraviolet detection of interstellar $^{12}C^{17}O$ and the CO isotopomeric ratios toward X Persei", *The Astrophysical Journal* **574**, L171-L174.

[19] R. Farrenq, G. Guelachvili, A.J. Sauval, N. Grevesse, C.B. Farmer (1991). "Improved Dunham Coefficients for CO from Infrared Solar Lines of High Rotational Excitation", *Journal of Molecular Spectroscopy* **149**, 375-390.

[20] T. George, W. Urban, A. Le Floch (1994). "Improved Mass-Independant Dunham Parameters for the Ground State of CO and Calibration Frequencies for the Fundamental Band", *Journal of Molecular Spectroscopy* **165**, 500-505.

[21] A. Le Floch (1992). "Accurate Energy Levels for the $C^1\Sigma^+$(v=0) and $E^1\Pi$(v=0) States of $^{12}C^{16}O$", *Journal of Molecular Spectroscopy* **155**, 177-183.

[22] K.H. Strobl (1986). *Lebensdauer gestörter Energieniveaus am Beispiel des CO-Moleküls*, PhD Dissertation, Leopold-Franzens-Universität Innsbruck, München.

[23] C. Haridass, K.P. Huber (1994). "A high-resolution ^{13}C isotope study in the vacuum ultraviolet of spectra of CO(A$\longrightarrow$X), C I, and C II", *The Astrophysical Journal* **420**, 433-438.

[24] L.M. Beaty, V.D. Braun, K.P. Huber, A.C. Le Floch (1997). "A high-resolution ^{18}O isotope study in the vacuum ultraviolet of the $A^1\Pi \longrightarrow X^1\Sigma^+$ 4^{th} positive system of CO", *The Astrophysical Journal Supplement Series* **109**, 269-277.

[25] C.M. Steinmann, A. du Plessis, E.G. Rohwer (2005). "High-resolution vacuum ultraviolet laser spectroscopy of molecules in a free supersonic jet: in search of rare CO isotopomers and CO-Ar van der Waals molecules", *South African Journal of Science* **101**, 87-88.

[26] R.W. Field, B.G. Wicke (1972). "Analysis of Perturbations in the $a^3\Pi$ and $A^1\Pi$ States of CO", *Journal of Molecular Spectroscopy* **44**, 383-399.

[27] P. Klopotek, C.R. Vidal (1984). "Frequency selective excitation spectroscopy of the CO intercombination bands", *Canadian Journal of Physics* **Vol. 62**, 1426-1436.

[28] K.H. Strobl, C.R. Vidal (1987). "Radiative lifetimes of selected rovibronic triplet levels of the CO molecule", *Journal of Chemical Physics* **Vol. 86, No. 1**, 62-70.

[29] F. Rostas, M. Eidelsberg, A. Jolly, J.L. Lemaire, A. Le Floch, J. Rostas (2000). "Band oscillator strengths of the intersystem transitions of CO", *Journal of Chemical Physics* **Vol. 112, No. 10**, 4591-4603.

[30] M. Eidelsberg, F. Rostas (2003). "An Atlas of Intersystem Transitions of CO", *The Astrophysical Journal Supplement Series* **145**, 89-109.

[31] http://amrel.obspm.fr/molat/ (13 November 2005), "MOLAT Atomic and Molecular Data", Website containing the Intersystem Transitions of CO analagous to reference [30], maintained by M. Eidelsberg.

[32] C.R. Vidal (1988). "Vacuum ultraviolet laser spectroscopy of small molecules", *Advances in Atomic and Molecular Physics* **Vol. 23**, 1-35.

[33] K. Yamanouchi, S. Tsuchiya (1995). "Tunable vacuum ultraviolet laser spectroscopy: excited state dynamics of jet-cooled molecules and van der Waals complexes", *Journal of Physics B: Atomic, Molecular and Optical Physics* **28**, 133-165.

[34] A.C. Provorov, B.P. Stoicheff, S Wallace (1977). "Fluorescence studies in CO with tunable VUV laser radiation", *The Journal of Chemical Physics*, **Vol. 67, No. 11**, 5393-5394.

[35] G. Hancock, H. Zacharias (1981). "Laser-induced fluorescence from CO($A^1\Pi$)", *Chemical Physics Letters* **Vol. 82, No. 3**, 402-404.

[36] H. Zacharias, H. Rottke, K.H. Welge (1980). "Photoionization of CO and NO by tunable VUV laser radiation", *Optics Communications* **Vol. 35, No. 1**, 185-188.

[37] A. Mellinger, C.R. Vidal (1994). "Laser-reduced fluorescence spectroscopy of predissociated CO triplet states", *Journal of Chemical Physics* **Vol. 101, No. 1**, 104-110.

[38] P. Klopotek, C.R. Vidal (1985). "Two-step vacuum-ultraviolet visible excitation spectroscopy on the CO molecule", *Journal of the Optical Society of America B*, **Vol. 2, No. 6**, 869-876.

[39] T. Ebata, N. Hosoi, M. Ito (1992). "Rotational analysis of v=1 level of n=8 $\sim$ 10 Rydberg states of CO by triple resonant multiphoton spectroscopy", *Journal of Chemical Physics* **Vol. 97, No. 6**, 3920-3930.

[40] M. Drabbels, J. Heinze, J.J. ter Meulen, W.L. Meerts (1993). "High-resolution double-resonance spectroscopy on Rydberg states of CO", *Journal of Chemical Physics* **Vol. 99, No. 8**, 5701-5711.

[41] M. Komatsu, T. Ebata, N. Mikami (1993). "Rotational analysis of n=4-7 Rydberg states of CO observed by ion-dip spectroscopy", *Journal of Chemical Physics* **Vol. 99, No. 12**, 9350-9365.

[42] A. Mellinger, E.G. Rohwer, C.R. Vidal (2001). "Carbon monoxide Triplet Rydberg Series in the f Complex Region", *Journal of Molecular Spectroscopy* **206**, 126-134.

[43] P.F. Levelt, W. Ubachs, W. Hogervorst (1992). "Extreme ultraviolet laser spectroscopy on CO in the 91-100 nm range", *Journal of Chemical Physics* **Vol. 97, No. 10**, 7160-7166.

[44] K.S.E. Eikema, W. Hogervorst, W. Ubachs (1994). "Predissociation rates in carbon monoxide: dependence on rotational state, parity and isotope", *Chemical Physics* **181**, 217-245.

[45] W. Ubachs, I. Velchev, P. Cacciani (2000). "Predissociation in the $E^1\Pi$ $v = 1$ state of the six natural isotopomers of CO", *Journal of Chemical Physics* **Vol. 113, No. 2**, 547-560.

[46] W. Ubachs, P.C. Hinnen, P. Hansen, S. Stolte, W. Hogervorst, P. Cacciani (1995). "Laser Spectroscopic studies of the $C^1\Sigma^+$, $v = 0$ and $v = 1$ States of CO", *Journal of Molecular Spectroscopy* **174**, 388-395.

[47] C. Chen (2004). "Recent advances in deep and vacuum-UV harmonic generation with KBBF crystal", *Optical Materials* **26**, 425-429.

[48] J.G. Eden (2000). "From N2 (337 nm) to High-Order Harmonic Generation: 40 Years of Coherent Source Development in the UV and VUV", *IEEE Journal on selected topics in quantum electronics* **Vol. 6 no. 6**, 1051-1060.

[49] C.R. Vidal (1987). "Four-wave frequency mixing in gases". In L.F. Molenauer and J.C. White (Eds.), *Topics in Applied Physics* **59** - *Tunable lasers*, 57-113, Springer-Verlag, Heidelberg.

[50] A. Mellinger (1995). *Untersuchung hochangeregter Triplettzustände des CO-Moleküls*, PhD Dissertation, Technische Universität München, München.

[51] G. Herzberg (1950). *Molecular spectra and molecular structure I: Spectra of diatomic molecules*, Van Nostrand Company, New York.

[52] J. M. Brown, J.T Hougen, K.P. Huber, *et al.* (1975) "The labelling of parity doublet levels in linear molecules", *Journal of Molecular Spectroscopy* **55**, 500-503.

[53] K.P. Huber, G. Herzberg (1979). *Molecular spectra and molecular structure IV: Constants of diatomic molecules*, Van Nostrand Company, New York.

[54] T. Imasaka, D.S. Moore, T. Vo-Dinh (2003). "Critical assessment: Use of supersonic jet spectrometry for complex mixture analysis", *Pure and Applied Chemistry*, **Vol. 75**, 975-998.

[55] A. du Plessis, C.M. Steinmann, E.G. Rohwer (2005). "Experimental conditions for vacuum ultraviolet laser spectroscopy", *South African Journal of Science* **101**, 93-95.

[56] *Dye Laser FL3001/2 Instruction Manual* (1988). Lambda Physik GmbH, Gottingen, Germany.

[57] P. Huang (2004). *Diagnostics in vacuum ultraviolet laser spectroscopy*, MSc thesis, University of Stellenbosch, Stellenbosch.